UNIVERSITÀ DEGLI STUDI DI VERONA

Department of Biotechnology

Graduate School of Science Engineering and Medicine

Doctoral program in

Nanotechnology and Nanomaterials for Bio-Medical Applications

Cycle XXVI - Year 2011

Fast 5d-4f luminescence of Pr^{3+} in new wide band-gap host lattices for applications in medical diagnostics

S.S.D. CHIM03

Coordinator: Prof. Adolfo Speghini

Tutor: Prof. Marco Bettinelli

Doctoral Student: Dott. Mattia Trevisani

Ai miei genitori e

a mio fratello

Contents

IV

Abstract

The work presented in this thesis is focused on the development and improvement of new wide band-gap luminescent materials used as fast scintillators in modern medical diagnostic techniques. The goal of this research consists in obtaining inorganic scintillators activated with trivalent preaseodymium (Pr^{3+}) ion where a very fast interconfigurational *d-f* emission could be observed.

The performance of scintillator materials is determined by the dissipation of high energy photons in a sequence of processes ultimately leading to the emission of visible or UV radiation. The understanding of the processes responsible for relaxation and migration of electronic excitations, and the transfer of energy to defects and impurity centers is crucial for successful development of new optical materials with enhanced performance, especially in terms of quantum efficiency, temporal response, radiation resistance, thermal and chemical stability.

In the present work polycrystalline powders of Ca_9LuPO_4:Ce^{3+}/Pr^{3+}, $K_3Lu(PO_4)_2$:Pr^{3+}, $KLuP_2O_7$:Pr^{3+}, X_2SiO_5:Pr^{3+} (X= Y, Lu) and single crystals of $BaMgF_4$:Nd^{3+} were synthesized and characterized. A systematic study of time-resolved luminescence spectra and luminescence decay profiles of these materials was performed at the HASYLAB, DESY synchrotron facility in Hamburg (Germany) in order to understand the electronic structure of luminescent centers, the influence of defects, and the main mechanisms responsible for host-to-impurity energy transfer and relaxation of the host electronic excitation. The research proposed in this project will allow developing an adequate model of creation and relaxation of electronic excitations establishing the main principles for the synthesis of new materials with controllable optical and luminescence properties.

Riassunto

Il lavoro presentato in questa tesi si pone l'obiettivo di studiare le proprietà ottiche e spettroscopiche di nuovi materiali luminescenti destinati ad applicazioni quali scintillatori veloci per moderne tecniche di diagnostica medica. Specificatamente la nostra attenzione è stata rivolta alla sintesi di materiali inorganici ad ampio *band-gap* attivati con lo ione trivalente praseodimio (Pr^{3+}) il quale, in seguito ad opportuna eccitazione, può dare luogo ad emissioni radiative veloci (15-25 ns) potenzialmente utili nella realizzazione di scintillatori.

Le prestazioni dei scintillatori sono determinate prevalentemente dalla dissipazione dell'energia assorbita in seguito all' irradiazione del materiale attraverso una sequenza di processi che portano infine all'emissione di radiazione visibile o ultravioletta. Lo studio e la comprensione dei meccanismi di rilassamento, migrazione e trasferimento dell'energia assorbita dal materiale ai difetti e/o impurezze è fondamentale per la progettazione di nuovi materiali ottici dalle prestazioni avanzate, soprattutto in termini di efficienza quantica, velocità di risposta, stabilità termica e chimica.

Nel presente lavoro di tesi sono stati preparati e caratterizzati campioni di $Ca_9LuPO_4:Ce^{3+}/Pr^{3+}$, $K_3Lu(PO_4)_2:Pr^{3+}$, $KLuP_2O_7:Pr^{3+}$, $X_2SiO_5:Pr^{3+}$ (X= Y, Lu) come polveri policristalline e $BaMgF_4:Nd^{3+}$ come cristallo singolo. Per ciascun materiale è stato quindi condotto uno studio ottico sistematico mediante spettroscopia di luminescenza risolta nel tempo e dinamica di stato eccitato al fine di comprendere la struttura elettronica dei centri luminescenti, l'influenza dei difetti reticolari e i principali meccanismi responsabili dei trasferimenti energetici tra matrice e ione luminescente.

L'attività di ricerca proposta in questo progetto di tesi porrà le basi per lo sviluppo di adeguati modelli sulle modalità di trasferimento energetico in nuovi materiali scintillatori attivati con ioni lantanidi, portando infine alla possibilità di progettare materiali dalle proprietà ottiche opportunamente selezionate e all'ottimizzazione delle prestazioni di materiali già in uso.

Chapter 1

Introduction

The development of new luminescent materials or phosphors for the conversion of various types of ionizing radiation into visible light has always been based on the deep understanding of processes responsible for absorption and dissipation of high energy photons, creation of intrinsic electronic excitations (free electrons and holes, *e-h* pairs, excitons), energy transfer to defects and impurities [1, 2]. These processes represent key problems in radiation physics of the solid state and are very important for improved performance of materials applied as X-ray phosphors and, especially, scintillators.

The field of scintillators is currently quite extensive and diverse. This is due to the unprecedented demand on detectors of ionizing radiation (X- and γ-rays) following requirements imposed by the modern nuclear medical imaging techniques such as computed tomography (CT), single photon emission tomography (SPECT) and positron emission tomography (PET), high-energy physics, security inspection, space applications etc. The modern technologies require increasingly superior characteristics of scintillators which are often well beyond those delivered by traditional ones, particularly in terms of quantum efficiency, temporal response, mechanical and chemical stability and radiation resistance.

In the last two decades a strong research activity has given rise to the formulation of new scintillator materials based on complex oxide hosts doped with Ce^{3+} ions. These materials exhibit efficient and relatively fast (20-70 ns) $5d$-$4f$ electric-dipole emission in a broad spectral range (350-600 nm) [3-6]. The introduction of new and faster scintillators such as Gd_2SiO_5:Ce^{3+} (GSO) and Lu_2SiO_5:Ce^{3+} (LSO) allowed the development of CT and PET scanners with significantly improved performance. Recently, much attention has been turned to the $5d$-$4f$ emission of Pr^{3+} ions in several wide band-gap hosts because of its shorter lifetime (typically 15-25 ns) allowing for the development of new scintillators which are two or three times faster than the commonly used ones activated with Ce^{3+} ions and which can show better performances for some applications. A number of Pr^{3+} doped oxidic materials, such as silicates (A_2SiO_5, $Lu_2Si_2O_7$, $Ca_3A_2Si_3O_{12}$, A=Y, Lu, Sc) [7-

10], garnets ($Lu_3Al_5O_{12}$, $Y_3Al_5O_{12}$) [11-14], aluminates ($LuAlO_3$) [12, 15], double phosphate ($M_3La(PO_4)_3$ and $M_9Lu(PO_4)_7$, M = Ca, Sr, Ba) [16, 17], etc. have been recently studied to test their potentials for fast scintillator applications.

This research project was conceived with the aim to provide insight into the nature and the time scale of the relaxation processes occurring after absorption of a high energy photon in Pr^{3+}-doped inorganic wide band-gap materials. This includes research on dynamics and spectroscopy of processes responsible for a fast feeding and radiative relaxation of $5d$ states of lanthanide ions (Pr^{3+} in particular), crystal structure defects and intrinsic electronic excitations (electrons, holes, e-h pairs, excitons) in wide band-gap crystal materials characterized by different dimensions, electronic structure and electron-phonon coupling. Our research also focuses on the understanding of photoionization phenomena and processes related to creation and relaxation of impurity trapped excitons.

In order to achieve these objectives, the work of this research has been organized as follows:

- ✓ synthesis of polycrystalline wide band-gap inorganic materials activated with Pr^{3+} ions by conventional solid-state inorganic routes, both in nanocrystalline and bulk forms;
- ✓ structural characterization of the obtained materials by X-ray powder diffraction;
- ✓ study of the luminescence properties and excited state dynamics of the materials employing time-resolved VUV spectroscopy upon excitation with synchrotron radiation, by focusing on the following topics: i) the $5d$-$4f$ luminescence of the Pr^{3+} ion and the energetic position of the $4f^15d^1$ configuration that is critical for photon cascade emission [18]; ii) the dopant/defect interactions as well as other processes responsible for the quenching of potentially useful luminescence; iii) host or defect excitation-induces emission of Pr^{3+} ion doped into complex oxide hosts.

All these studies address fundamental issues that are central in the field of the optical and spectroscopic properties of wide-band gap inorganic materials, and are therefore scientifically relevant in the area of Physics of Condensed Matter. Additionally, it is hoped to obtain advances in the development of new materials yielding efficient and fast luminescence in the UV and visible regions, as they find numerous applications in many important technological fields.

The host lattices selected for these studies are new complex oxides and fluorides with a wide band gap (7-9 eV), including the family of the oxyorthosilicates having general formula A_2SiO_5 (A = X1-Y, X2-Y and X2-Lu) as nano-powders, the double phosphates $Ca_9Lu(PO_4)_7$, $K_3Lu(PO_4)_7$ and $KLuP_2O_7$ as bulk powders and the fluoride $BaMgF_4$ as single crystal. For some of these materials it has been explored the spectroscopy of other luminescent centers, i.e. Ce^{3+} and Nd^{3+}, which,

together with Pr^{3+}, represent excellent candidates for the realisation of new advanced fast scintillator materials.

References

1. Pédrini, C., *Electronic processes in rare earth activated wide gap materials.* physica status solidi (a), 2005. **202**(2): p. 185-194.

2. Yen, W.M., *General factors governing the efficiency of luminescence devices.* Optical Materials, 2005. **27**(11): p. 1647-1652.

3. Ogiegło, J.M., et al., *Luminescence and Energy Transfer in $Lu_3Al_5O_{12}$ Scintillators Co-Doped with Ce^{3+} and Tb^{3+}.* The Journal of Physical Chemistry A, 2012. **116**(33): p. 8464-8474.

4. Melcher, C.L., et al., *Cerium oxidation state in LSO:Ce scintillators.* Nuclear Science, IEEE Transactions on, 2005. **52**(5): p. 1809-1812.

5. Korzhik, M. and P. Lecoq, *Search of new scintillation materials for nuclear medicine applications.* Nuclear Science, IEEE Transactions on, 2001. **48**(3): p. 628-631.

6. Eijk, C.W.E.v., *Inorganic scintillators in medical imaging.* Physics in Medicine and Biology, 2002. **47**(8): p. R85.

7. Nikl, M., et al., *Fast 5d→4f luminescence of Pr^{3+} in Lu_2SiO_5 single crystal host.* Chemical Physics Letters, 2005. **410**(4–6): p. 218-221.

8. Nikl, M., et al., *Luminescence and scintillation kinetics of the Pr^{3+} doped $Lu_2Si_2O_7$ single crystal.* Chemical Physics Letters, 2010. **493**(1–3): p. 72-75.

9. Ivanovskikh, K.V., et al., *Optical spectroscopy of $Ca_3Sc_2Si_3O_{12}$, $Ca_3Y_2Si_3O_{12}$ and $Ca_3Lu_2Si_3O_{12}$ doped with Pr^{3+}.* Journal of Luminescence, 2010. **130**(5): p. 893-901.

10. Ivanovskikh, K.V., et al., *VUV Spectroscopy of $Ca_3Sc_2Si_3O_{12}$:Pr^{3+}: Scintillator Optimization by Co-Doping with Mg^{2+}.* ECS Journal of Solid State Science and Technology, 2012. **1**(5): p. R127-R130.

11. Ogino, H., et al., *Growth and Luminescence Properties of Pr-doped $Lu_3(Ga,Al)_5O_{12}$ Single Crystals.* Japanese Journal of Applied Physics, 2007. **46**(6R): p. 3514.

12. Wojtowicz, A.J., et al., *Scintillation properties of selected oxide monocrystals activated with Ce and Pr.* Optical Materials, 2006. **28**(1–2): p. 85-93.

13. Ivanovskikh, K.V., et al., *Luminescence Temperature Quenching for Ce^{3+} and Pr^{3+} d-f Emission in YAG and LuAG.* ECS Journal of Solid State Science and Technology, 2013. **2**(2): p. R3148-R3152.

14. Yoshikawa, A., et al., *Energy Transfer to Pr^{3+} Ions in $Pr:Lu_3Al_5O_{12}$ (LuAG) Single Crystals.* Nuclear Science, IEEE Transactions on, 2008. **55**(3): p. 1372-1375.

15.   Korzhik, M.V. and P. Lecoq, *Physics of scintillation in REAlO$_3$:Ce$_{3+}$ (RE=Y, Lu)*. Nuclear Instruments and Methods in Physics Research Section A: Accelerators, Spectrometers, Detectors and Associated Equipment, 2005. **537**(1–2): p. 40-44.

16.   Ivanovskikh, K., et al., *Fast UV luminescence in Pr^{3+}-doped eulytite double phosphates*. Optical Materials, 2011. **34**(2): p. 419-423.

17.   Trevisani, M., et al., *Interconfigurational 5d → 4f luminescence of Ce^{3+} and Pr^{3+} in Ca$_9$Lu(PO$_4$)$_7$*. Journal of Physics: Condensed Matter, 2012. **24**(38): p. 385502.

18.   Srivastava, A.M., et al., *The influence of the Pr^{3+} 4f^{1}5d^1 configuration on the $^1S_0$ emission efficiency and lifetime in LaPO$_4$*. Optical Materials, 2011. **33**(3): p. 292-298.

Chapter 2

Theory

2.1 Scintillation and inorganic scintillators

Inorganic scintillator materials are commonly used in today's radiation detectors for medical imaging, high-energy physics, geophysical exploration, interplanetary exploration, and security applications. In each application the scintillator is the primary radiation sensor that emits light or "scintillates" when struck by high-energy photon. The words *scintillator* and *scintillation* are derived from the word *scintilla* which is Latin for spark. An inorganic scintillator is essentially a luminescent material that absorbs high energetic radiation, such as α-, β-, γ-, X-rays, neutrons or high energetic particles, and convert this absorbed radiation into radiation with a wavelength in or around the visible spectral region. The emitted radiation is thus converted into an electric signal by a photomultiplier tube (PMT) or a charge coupled device (CCD) detector.

The investigation described in this thesis are especially focused on the search for new scintillators material as radiation detectors for the X- and γ-ray imaging techniques, such as computed tomography (CT), single photon emission computed tomography (SPECT) and positron emission tomography (PET). The rapid evolution in medical imaging equipment has led to the requirement of increasingly fast and efficient scintillator materials in order to improve their radiation detection performance [1]. Some scintillators that are applied nowadays in the above-mentioned medical diagnostics have serious drawbacks concerning afterglow, decay time, and the matching between emission wavelength and light detector sensitivity. If the scintillator characteristics are improved, the irradiation dose to be administer can be lowered and scanning times can be shortened, which is particularly beneficial for the patient.

2.1.1 A brief history of scintillators

The history of scintillators begins in 1895 with Röntgen's discovery of the barium platinocyanide fluorescence excited by X-rays. In the following year Becquerel discovered that

certain luminescent crystals containing uranium emit light spontaneously [2] and Pupin made first use of $CaWO_4$ in X-ray intensifying screens [3]. It was only shortly thereafter that the works of Maria Sklodowska and Pierre Curie established the existence of radioactivity as a general phenomenon, stimulating an avalanche of discoveries that changed the face of modern physics. Crookes, in 1990, used ZnS to detect and count radioactivity, a method that was used some years later, in 1909, by Rutherford in his famous experiments on scattering of α particles [4]. While in the early days scintillations were evaluated visually, the combination of the photomultiplier tube (PMT) and new scintillator materials discovered after World War II established the scintillator counter as we know it today. It was Hofstadter's discovery of the thallium-activated alkali halides [5] that triggered a series of advanced research programs using modern solid state physics and spectroscopy, beginning, at long last, to develop a comprehensive understanding of the physical mechanisms behind the scintillation effect. Thallium doped sodium iodide, NaI:Tl, which was presented for the first time in 1948, was the most popular scintillator used in the detectors for the following tens of years due to its high light yield.

The next great step in scintillator development took place in the early 1970's, with the discoveries of CaF_2:Eu [6], BaF_2 [7], and $Bi_4Ge_3O_{12}$ (BGO) [8]. In particular BGO has had an extraordinary history, originally proposed in the late 1969 for nuclear medicine applications [9] and culminating in 1990 when 12000 crystals of this material (24 cm in length each) were used for the fabrication of the largest electromagnetic-radiation calorimeter in the world (CERN, Geneva). Today BGO serves as a standard material for comparison for newly developed scintillators.

During the last decade the need for improved radiation detectors began to grow rapidly. High energy physics urgently sought new extremely radiation-resistant scintillator materials capable of recording very small cross-section events produced by high repetition rate collisions in a new generation of highly luminous accelerators (LHC at CERN, SSC, SLAC, FNAL and Cornell in the USA) [10]. Medicine, where the evolution of diagnostic radiology from simple X-ray photography into computed tomography, single photon emission computed tomography and positron emission tomography stimulated the early development of new scintillators and phosphors, now began to demand even denser, brighter and faster materials. Since the discovery of Lu_2SiO_5:Ce^{3+} by Melcher and Schweitzer in 1992 [11] a large number of Ce^{3+} doped Lu-compounds have been studied resulting in the discovery of other high-light yield scintillators like $LuAlO_3$:Ce^{3+} [12] and $LuPO_4$:Ce^{3+} [13].

The newest scintillators $LaCl_3$:Ce^{3+} and $LaBr_3$:Ce^{3+} [14] were discovered at Delft University and provide record high energy resolution and ultrafast detection of gamma rays.

In Fig. 2.1 the history of inorganic scintillators discovery is schematically reported.
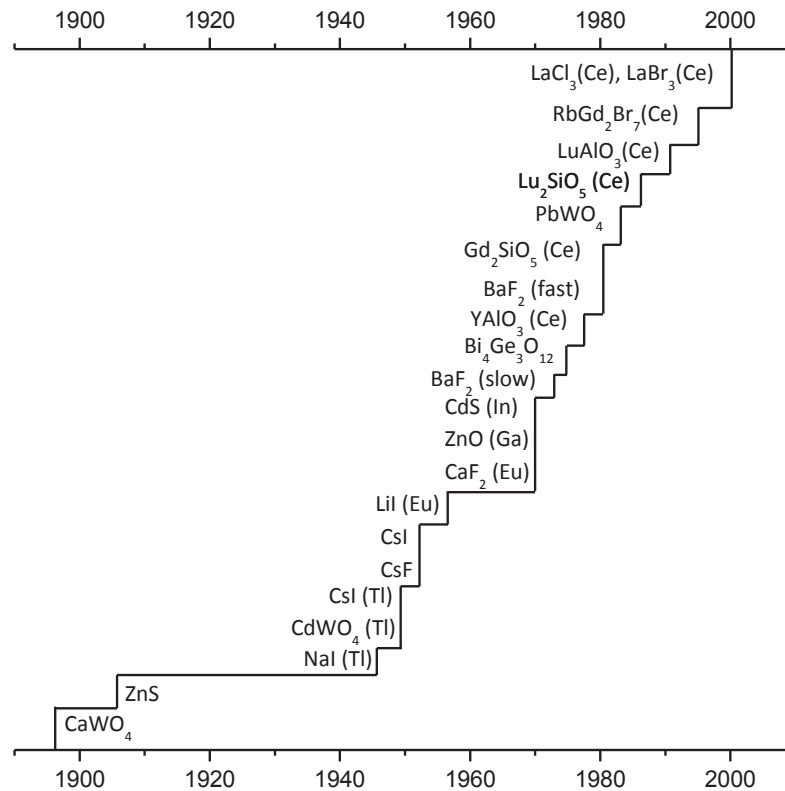
Fig. 2.1. The history of inorganic scintillators discovery (adapted from [15]).

2.1.2 The development of the medical imaging technologies

The first medical image is the X-ray image that Röntgen took of his wife's hand in 1895 using a photographic film to convert the X-ray into a form observable by the human eye [16] (Fig. 2.2).

Fig. 2.2 On the left, a picture of Wilhelm Conrad Röntgen; on the right, one of the first X-ray photographs of the hand of the wife of Röntgen, Anna Berta Ludwig

One year later, powdered phosphors materials such as $CaWO_4$ [17] replaced the photographic films previously used as the X-ray conversion material and have been an integral part of medical devices ever since. As matter of the fact, virtually all medical imaging modalities that require the detection of energetic photons (X- and γ-rays) utilize scintillator materials for their detection. These modalities include planar X-ray imaging, computed tomography (CT), single photon emission computed tomography (SPECT) and positron emission tomography (PET). With the increasing requirements for medical imaging equipment, the demand for the scintillators as the detection material in imaging has been became enormous. It has been documented [18] that about 175 metric tons of scintillators are required annually for medical diagnostic applications (Table I).

Table I. Annual volume of scintillator required for medical imaging technologies [18]

Modality	Annual production (screen)	Annual scint. (volume/m^3)
Planar X-ray	1000000	50
CT	2000	0.15
SPECT	2000	6
PET	50	0.5

In the field of medical imaging diagnostics, the energy of the photons detected is generally between 15 and 600 KeV. The detection system has to be very efficient because there is an intrinsic limit of radiation dose that can be administered to a patient due to safety concerns. Thus the only way to improve the signal-to-noise ratio and then the image quality can be achieved by increasing the sensitivity of detector. The development of scintillators used in planar X-ray imaging, e.g. Gd_2O_2S:Tb and LaOBr:Tb, and used in CT, e.g. $(Y,Gd)_2O_3$:Eu, Pr and Gd_2O_2S:Pr,Ce,F seems relatively mature [19]. Nowadays, the attention is mainly focused on the improvement of the performance of the scintillators used in SPECT and PET imaging systems.

SPECT is based on detecting individual photons emitted randomly by a radioactive element (such as ^{99m}Tc with the emission of 140 KeV photons) which is introduced into the body of the patient either by injection or inhalation. The emitted γ-rays are detected by two-dimensional position sensitive detectors based on a scintillator material (Fig. 2.3). The collimator and detector combination form what is known as a gamma-camera. The direction of the gamma rays is determined by a collimator placed between the detector array and the patient, while the photons that are not travelling in the desired direction are absorbed by the collimator. When the gamma-camera is rotated around the patient and/or two opposed gamma-cameras are used, it is possible to construct a three-dimensional image.
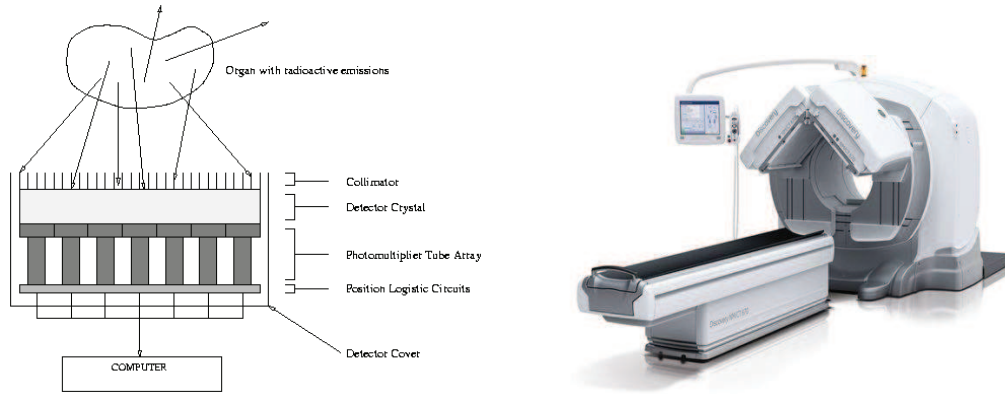
Fig.2.3 On the left, a schematic gamma-camera. On the right, a typical SPECT scanner.

Similar to SPECT, the patient for PET imaging is injected with a biological substance which is labelled with a positron emitter; most commonly used are ^{11}C, ^{13}N, ^{15}O and ^{18}F. Imaging of regional tracer concentration is accomplished by the unique properties of positron decay and annihilation. After the emission from the parent nucleus, the energetic positron traverses a few millimeters through the tissue until it becomes thermalized by electrostatic interaction between the electrons and the atomic nuclei of the media and combines with a free electron to form a positronium. The positronium decays by annihilation, generating a pair of gamma rays which travel in nearly opposite directions with an energy of 511 KeV each. The opposed photons from positron decay can be detected by using pairs of collinearly aligned detectors in coincidence (Fig. 2.4).
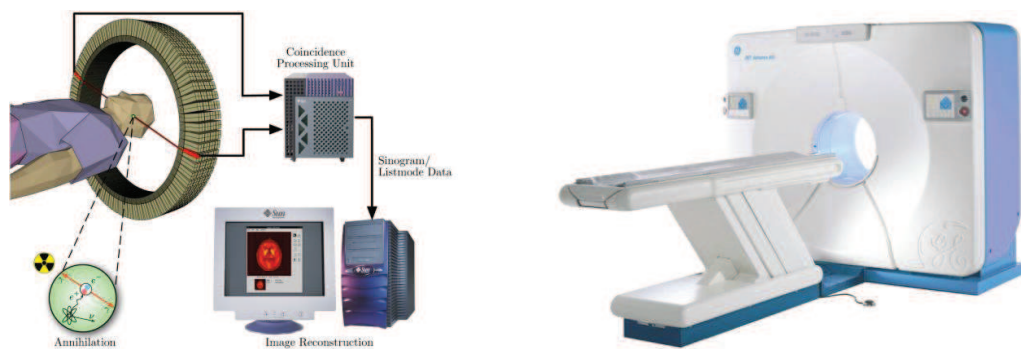
Fig. 2.4 On the left, a schematic acquisition PET scheme. On the right, a typical PET scanner.

This electronic collimation is the reason why PET is much more sensitive (factor >100) than the conventional nuclear medical technique such as SPECT. The detector pairs of a PET system are installed in a ring-like pattern, which allows measurements of

radioactivity along lines through the organ of interest (the so called Line of Response, LOR) at a large number of angles and radial distances. Subsequently, this angular information is used in the reconstruction of tomographic images of regional radioactivity distribution. Recently, special efforts have been made in the development of fast ($\tau \leq 50$ ns) or even ultrafast ($\tau \leq 5$ ns) γ-ray PET detectors [20] based on scintillator materials in order to reduce the random coincidence rate (Fig. 2.5) and thus to improve the quality of the tomographic images. In the section 2.1.4. several aspects of scintillator performance, including the response time, will be addressed in more detail.

TRUE COINCIDENCES   SCATTERED COINCIDENCES
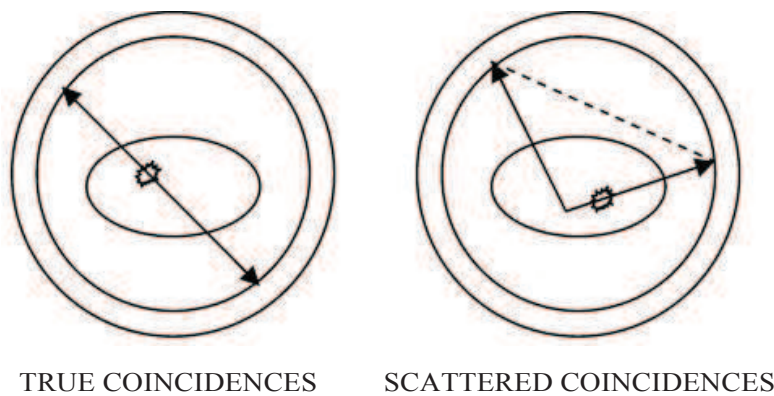
Fig. 2.5 Transaxial view of ring of detectors and organ of interest demonstrating the true coincident and random coincidence events.

2.1.3 Basic scintillation mechanism

Scintillation conversion is a complex process [21], which is usually simplified into three consecutive subprocesses (Fig. 2.6):

i.   *Absorption/multiplication*: absorption of a high-energy particle creates an inner shell hole and a primary electron; the multiplication of electrons and holes occurs by radiative decay, non-radiative decay (Auger processes), and inelastic electron/electron scattering. When the electron energies become less than the ionization threshold, electrons and holes thermalize into the bottom of the conduction band and the top of the valence band, respectively. The electrons and holes can remain free or combine to form free or self-trapped excitons.

ii. *Energy carrier migration*: usually, the site of the absorption of incoming radiation and that of the final emission do not coincide; in that case, the energy has first to migrate before

transferring to a luminescent center. The speed and efficiency of the scintillation processes are influenced by the properties of the energy carriers.

iii. *Relaxation/emission*: an excited emitting center releases its energy by emitting a photon or via non-radiative processes.
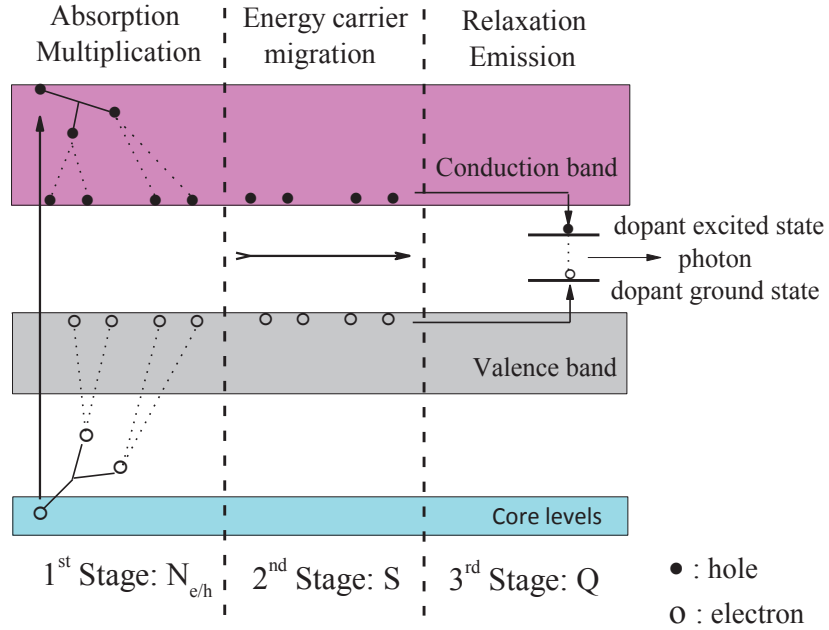
Fig. 2.6 Sketch of scintillating mechanism (reproduced from [15]).

These three stages of the scintillation process determine the overall scintillation efficiency of a scintillator, Y_{ph}, which is given by the number of photons produced per energy of incoming particle, $E_{incident}$ (usually photon/MeV):

$$Y_{ph} = N_{e/h}SQ = \frac{10^6}{E_{e/h}}SQ = \frac{10^6}{\beta E_g}\,SQ \tag{2.1}$$

where $N_{e/h}$, S, Q and $E_{e/h}$ are number of electron/hole pairs created during the multiplication stage, the efficiency with which an energy carrier is going to excite a luminescent center, the quantum efficiency of the luminescent center and the energy required to create one electron/hole pair, respectively. It is important to realize that the energy $E_{e/h}$ which is necessary to create the average electron-hole pair is much larger than that of the pair, i.e., $E_{e/h} = \beta E_g$ $(\beta > 1)$, where E_g is the band-gap energy (in eV) and β represents a proportional constant. Shockley estimated that $3E_g$ is needed per pair [22]; later, Robbins showed that this value can vary between $2.3E_g$ and $7E_g$, depending on

the host lattice [23]. In addition the emitted radiation, E_{em}, generally will be situated at energies below E_g. Therefore $N_{e/h} = (E_{em}E_g^{-1})(E_g E_{e/h}^{-1})$, where E_{em} is the energy of the emission maximum. For a given host lattice it is possible to estimate the value of β, so that the value of $N_{e/h}$ can also be estimated, since the values of E_g and E_{em} can be easily obtained spectroscopically.

2.1.3.1 Transfer process S

Whereas Q is understood, S is a least well-known quantity governing the light yield of the conversion process. S is affected by non-radiative processes that are generally dependent on many parameters: energy carrier types, temperature and impurities. In particular S can be significantly degraded by the presence of defects, which can trap migrating electrons and holes thereby quenching or delaying the scintillating process. By better understanding the structure of traps, materials can be designed to minimize non-radiative transitions by lowering the concentration of traps/defects. The transfer efficiency S is equal to 1 only if the electron-hole pair is exclusively captured by the luminescent center. Obviously, as soon as the pair ends its life in a different way, the value of S becomes smaller than 1.

We wish here to present the physics of transfer in a greatly abbreviated form. This enormously complex problem will be dealt with by considering three generic types of transfer and giving some indications of their relative importance.

1. **Radiative transfer** occur whenever there is an overlap between the absorption of the luminescent center that emits the scintillation light and another emission originating elsewhere in the lattice. The most common example of this is self-absorption, where both absorbing and emitting centers are chemically identical. The phenomenon consists of the emission of a real photon and its reabsorption before leaving the medium, for which reason it is also known as radiation imprisonment or trapping. The effect is most noticeable in materials characterized by resonance radiation and has been extensively studied in gases (primarily Hg vapor [24]).

2. **Excitonic transfer**: S is also influenced by the energy transfer such as transfers from self-trapped hole (STH) or exciton (STE) to dopant ion [25]. These mechanisms (see Fig. 2.7) have been experimentally [26] and theoretically [27] demonstrated in several systems, mostly halides. As a function of the STH or STE properties the transfers can or cannot occur. STH transfer is governed by the energy barriers of the hole trapping and the STH diffusion, respectively. STE energy transfer is governed by the dipole/dipole energy transfer probability from the STE to the dopant ion according to the eq. 2.2

$$W_{STE \rightarrow dopant}(r) = \tau_{STE}^{-1}(\frac{R_{d-d}}{r})^6 \qquad (2.2)$$

where τ_{STE} is the lifetime of the STE and R_{d-d} depends on the overlap of the absorption of the dopant and the emission of the STE. If both mechanism are complex, it has been shown that they can be optimized by changing the dopant concentration and anion type [26]. Schematically, the dopant concentration decreases the distance between a STH (STE) and the dopant site, maximizing the energy barriers of STH trapping and migration or STE lifetime. STH energy barriers decrease in the row $Cl \rightarrow Br \rightarrow I$ while STE lifetime increase. These trends provide useful information to maximize the probability for an efficient transfer from the lattice to the emitting center.
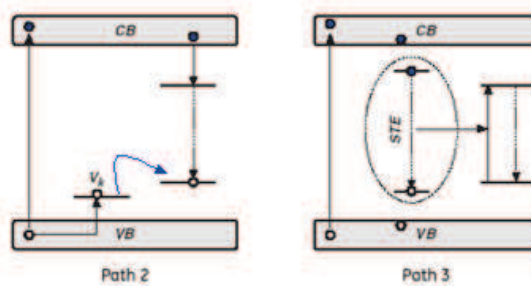
Fig 2.7 On the left, formation of self-trapped hole (STH) and followed by recombination on luminescent ion; on the right, formation of self-trapped exciton (STE) followed by recombination on luminescent ion.

3. ***Sequential trapping*** of free charge carriers at activator ions, without the formation of excitons, is yet another mechanism of transfer. In this case migrating electron and holes can be trapped by the presence of the defects quenching or delaying the scintillating process. By better understanding the structure of traps, the materials can be designed to minimize non-radiative transitions by lowering the concentration of traps/defects. This mechanism is common in many luminescent materials and a comprehensive discussion of its role in rare earth doped scintillators has been given by Wojotowicz in a contribution at the International Conference on Inorganic Scintillators and their Application, *SCINT95* [28].

2.1.3.2 Luminescence Yield Q

The luminescence process is described by the quantum yield Q, which is generally a well known quantity, particularly for the weak electron-lattice coupling characteristic of the RE ions. By

painstaking effort the quantum efficiency can be measured directly, but it is equally valid and far easier to obtain as the ratio of the overall decay time to the radiative lifetime τ_r: $Q = \tau_d/\tau_r$. The theoretical understanding of Q, or, equivalently, the nonradiative rates, is well grounded, especially for narrow band emitters such as the RE ions. For broad band emitters such as BGO, the theory is not in quite a good shape [29], but empirical data are abundant.

2.1.3.3 Kinetics of the response

The kinetics of the light response of a scintillator is clearly governed by the rate constants of the *energy carrier migration* (R_{tfr}) and *emission* (R_r) processes (see Fig. 2.6), as they are by far slower with respect to the initial *absorption and multiplication* stage. The decay rate of the luminescent centre itself is defined by its transition dipole moment from the excited-to-ground state and can be further enhanced by additional non-radiative quenching, or energy transfer process away from the excited state. Such quenching or energy transfer, however, results in the decrease of parameter Q in equation (1) and the overall conversion efficiency gets smaller. In the simplest case of exponential decay, the emission intensity $I(t)$ is:

$$I(t) = A exp[-t/\tau] \tag{2.3}$$

where A is a proportional constant and τ is called decay time.

There is no fundamental limitation on the transfer rate. It can be instantaneous when the luminescence center is excited directly, with no intermediate steps like excitons or e-h pairs. Unlike the case of the transfer rate, there is a fundamental physical law that limits the radiative rate R_r (inverse of the Einstein coefficient A). For electric dipole emission the radiative lifetime $\tau_r = 1/R_r$ in ns is given by [30] :

$$\tau_r = 1.5 \cdot 10^{-5} \cdot \frac{9\lambda^2}{f \cdot n \cdot (n^2+2)^2} \tag{2.4}$$

where f is the oscillator strength of the transition (summed over the final states and averaged over the initial states), λ is the wavelength of the transition in nanometers and n is the refractive index. For the fastest possible scintillators, therefore, two important conditions must be met: the optical transitions must be fully allowed by all relevant selection rules, with a high oscillator strength and consequently short radiative decay time τ_r; simultaneously the transfer time has to be significant shorter than τ_r to allow the radiative decay to govern the rate.

2.1.4 Requirements

There is a variety of radiation detector applications that desire scintillators with high light output, good attenuation power, a low level of afterglow, and a fast scintillating decay time, but generally the specific properties of the scintillators are carefully chosen depending on the destination of the material. Scintillators are used in a wide range of applications, including medical imaging, high energy physics, space exploration and homeland security. The following aspects are important in the evaluation of the performance of a generic scintillator material:

- ▪ *Stopping power (attenuation coefficient).* For efficient absorption of high energetic radiation (from 100 KeV to 10 MeV) a scintillator should contain high atomic number (Z) elements (e.g. Ba, La, I, Lu, Cs, Pb, Bi) and posses a high density (ρ). As matter of the fact, elements with a high atomic number are characterized by higher electron densities and thus a higher absorption cross-section for X-rays and γ-rays. In order to evaluate the detection efficiency the *linear attenuation coefficient* μ is usually used, which is defined as the probability per unit length that a incident X- or γ-ray will be removed from the beam. This is just a sum of the probabilities for the three important ray-matter interaction modes (eq. 2.5).

$$\mu = \kappa_{photoelectric} + \sigma_{compton} + \tau_{pair} \qquad (2.5)$$

As thoroughly argued by van Eijk in [31], considering the photoelectric effect, for an efficient and small scintillator detector, both a large density ρ and effective atomic number Z_{eff} [32] is needed. For detection by Compton scattering one might be tempted to conclude that only the density should be large. For detection by means of pair production both a high ρ and a high Z_{eff} is required. In Table II the dependence of the linear attenuation coefficients for the main interaction processes of X- and γ-rays with matter on the density ρ and the atomic number Z is summarized.

Table II. Linear attenuation coefficients (cm^{-1}).

Photoelectric effect	$\kappa \propto \rho Z_{eff}^{3-4}$
Compton scattering	$\sigma \propto \rho Z_{eff}^{0}$
Pair production	$\tau \propto \rho Z_{eff}^{1}$

Concluding, it may be stated that in general both a high density ρ and a high effective atomic number Z_{eff} are important. Of course it should be realized that the importance of the different interaction mechanisms for the primary interaction processes varies strongly with

energy. Photoelectric effect dominates at lower energies ($\leq$100 KeV; $\mu = \sigma$ at 500 KeV for $Z = 80$ material), Compton scattering is most important as intermediate energies, and pair production can only occur above 1022 KeV.

- *Chemical stability and mechanical strength.* The chemical composition of a scintillator should not change over time due to exposure to the environment or high energy radiation. Changes due to absorption of water (for hygroscopic scintillators) or the change in valence states of activator ions in an oxidizing environment are examples of undesired chemical changes. Ruggedness and mechanical shock resistance are additional highly desirable characteristics.

- *Light Output.* The light output is generally given as the number of photons emitted per MeV of energy of incoming radiation (ph/MeV). According to equation (1) it is commendatory to study preferentially materials having a small E_g. For materials being build of ions having a noble gas configuration, E_g decreases roughly along the series fluorides (9-12 eV), oxides (5-9 eV), chlorides (6-8 eV), bromides (5-7 eV), iodides (4-6 eV), sulphides (2-5 eV) and selenides (2-4 eV). In the search for new scintillator materials, mainly oxides and fluorides gained attention. Whereas high light yield may not be too critical for detecting very energetic particles, for applications where the particle energy is smaller or fixed, e.g. in positron emission tomography, increased light yield is important for improving accuracy, spatial- and energy-resolution.

- *Decay time.* Fast signal rise and decay times are important for good timing resolution and high counting rates or for time-of-flight modes of operation. Very short response time (< 100 ns) is absolutely required in PET scanners where the coincident detection of γ-rays have to be realized.

- *Afterglow.* Persistent emission or afterglow is emission that continues for second, minutes or even hours after the excitation pulse and it should be avoided as much as possible. It is caused by the slow thermally activated release of trapped charge carriers that have been created under high energy excitation; this results in a lowering of the direct light output and leads to ghost images. The afterglow properties are strongly influenced by the synthesis procedure of the material, as it usually involves defects.

- *Radiation damage.* Stability and reproducibility of light output of a scintillator are critical to many applications. Radiation damage refers to the change of scintillation efficiency due to defect creation by the radiation dose. These defects are commonly color centers whose electronic structure imparts optical absorption bands at the scintillator wavelengths. As in the case of afterglow, the binding energy of the color center determines the longevity of the damage. In general, this energy is sufficiently large that damage can last from second to

days at room temperature. Although radiation damage typically decreases the scintillation efficiency, there are exceptional cases where the efficiency increases; this latter behaviour is likely due to the modification or neutralization of defect centers that otherwise reduce the scintillator's quantum efficiency.

- ▪ *Emission wavelength.* The emission of a scintillator has to be detected with the highest possible sensitivity. This depends on the wavelength of the emission and the type of the detector used. If the emission is detected by a PMT, the best signal to noise ratio is obtained in the UV-blue part of the spectra; on the other hand, if the detector is a CCD camera or a Si-photodiode, the emission should be in the green-red spectral region to obtain the best sensitivity. In the recent years an enormous development of semiconductor photodetectors has occurred and the latest generation of the back illuminated CCD from Hamamatsu announced for 2005 shows an enhanced sensitivity down to 200 nm.

2.2 Materials

Generally, one can group scintillator materials into two classes:

- *Intrinsic scintillators*, in which the luminescence center is created by the structural unit or an intrinsic defect of the host. Examples are CsI, $Bi_4Ge_3O_{12}$, CeF_3, $PbWO_4$ and BaF_2.
- *Extrinsic scintillators,* in which the luminescence center is a well defined impurity ion, introduced into a host lattice. A prime example of this kind of material is $NaI:Tl$; others include the more modern wide band-gap materials utilizing some RE^{3+} ions, such as Ce^{3+}, Pr^{3+} and Nd^{3+}.

Obviously the border between intrinsic and extrinsic scintillators is not very rigid and may even be crossed deliberately. An example is provided by such materials as $Ce_xLa_{1-x}F_3$, which can be prepared with active ion (Ce) concentration anywhere between 0 and 100%.

2.2.1 The host lattice

The choice of the type and morphology of the host lattice is crucial to determine the performance of the scintillation process. Nowadays oxide-based lattices are the major focus of attention for the realization of new and improved scintillator materials. There are essentially two reasons for such attention. One is that most oxides are particularly inert to ambient conditions of

handling and use. Typically they are quite hard, chemically inert, insoluble in water and particularly amenable to optical processing. In contrast, most halides tend to be relatively soft, water soluble, and vulnerable to attack by atmospheric moisture. While fluoride are less susceptible to these deficiencies, they are far more difficult to synthesize in pure form than oxides, and are particularly sensitive to the presence of even minute amounts of oxidic contamination, which severely degrades their emission properties.

In this thesis most of the synthesized matrixes contain Lu^{3+} ion. As is obvious from the previous discussion (section 2.1.5), the Lu^{3+} ion is particularly favored as a major constituent of the host lattice because of its high atomic number, imparting a high density and concomitant stopping power to the lattice. In addition Lu ion, by virtue of its full $4f$ shell, has a much higher-lying core level (6.9 eV in free atom) than to the other spectroscopically inert rare earths (Y, 25.6 eV; La, 14.4 eV) [33]. While Robbin's theory of conversion [23] does not consider the core levels, such an easily ionizable electronic state could conceivably have a significant influence on the conversion and transport processes. Any attempt to answer this question is hindered by the fact that, with the one exception of $YAlO_3$ (YAP), yttrium based compounds have received far less development effort than their Lu counterparts.

Regarding the morphology of the scintillator, currently are known six types of materials used in radiation detection: single crystals, polycrystalline ceramics, glasses, powders, plastics, and inert gases. Despite of the best figure-of-merit of the single crystal scintillators, by far not all intrinsically efficient compounds can be grown in the form of bulk single crystals with sufficiently big dimension and manufacturing price affordable for practical applications [34, 35]. Too high melting temperatures, presence of phase transitions between the melting point and room temperature or stoichiometry problems coming from different volatility of binary constituents from the high temperature melt of complex compounds are just few examples of troubles which can make single crystal preparation impossible. Optical ceramics have been under development as an alternative to single crystal materials to provide bulk optical elements in the case where single crystals cannot form or when ceramic materials show superior properties, for example in the achievable concentration and homogeneity of the dopant. A wet chemical coprecipitation process is used to make the powders, and a special sintering process in instituted for transforming powder compacts into transparent luminescent ceramic. In the case of cubic materials the technological progress allowed to obtain bulk samples virtually indistinguishable from single crystals and in some parameters (doping profile) even clearly superior. Development of optical ceramics for the scintillator applications was triggered by the needs of Computed Tomography medical imaging. The review of the results achieved mainly at the manufacturing and characterization of

$(Y,Gd)_2O_3$:Eu, Gd_2O_2S:Pr, Ce, F and $Gd_3Ga_5O_{12}$:Cr, Ce ceramics was reported by Greskovich in [35].

Another important approach in developing new scintillators materials, which will be addressed in detail in chapter 3, consists in getting a control of the material on a nanometric scale. It is indeed very important to control the concentration and the homogeneity of the luminescent ions throughout the host lattice and to control the size of the grains in the case of the powders. Numerous excellent reviews can be found in the recent literature concerning the scintillating response of a wide range of nanostructured materials, especially based on oxide matrixes. In 2008 it was documented by Klassen et al. [36] that scintillator materials in the form of nanocrystalline powders are an emerging field of research as the nano-scale induces the appearance of new optical properties which, in turn, bring new conceptions for application of such materials and open opportunities for improvement of exploitation characteristics of the radiation detectors including their sensitivity, spatial and temporal resolutions, radiation hardness, etc. These potential advantages are attributed to the particular features of electron and phonon excitations, photon resonances, behaviour of point defects predetermined by nanoscopic dimensions of the particles, which are as small as typical spatial parameters of electrons, phonons and photons. Specific surface and structural effects as well as quantum and dielectric confinements occuring in the nanoparticles, particularly doped insulators, and their consequences on the optical and scintillating properties were reported and discussed in detail in a recent review by Dujardin et al. [37]. Manufacturing of nanopowders of scintillating materials attracts a certain interest of scientists and producers also for the possibility to fabricate transparent ceramics that could replace advantageously the corresponding single crystals whose production generally required longer manufacturing times and higher costs. Another very attractive solution is the direct preparation of scintillating thin films which recently have appeared to be an interesting alternative to reduce diffusion phenomena and to improve the scintillation properties of the commonly used phosphors.

2.2.2 Lanthanides (Rare Earths)

Lanthanides (numbers 57 to 71 in the periodic table of elements), together with scandium (21) and yttrium (39) are the group of elements with an incompletely filled 4*f* inner shell. The name "lanthanide" comes from the Greek word λανθανειν which means "to lie hidden". These elements are also called rare earths due to the fact that the minerals from which they were first isolated in the form of "earths" (archaic term of oxide) were believed to be quite rare. However, even the most "rare" rare earth elements, thulium, is still more abundantly present in the earth crust than gold

[38]. Yet rare earth ores are rare in the sense that their concentrations are more difficult to find than those of most other ores.

The first report on lanthanide ions dates from 1788, when B. Geijer documented the analysis of a stone found near Ytterby, Sweden. This mineral was called yttria and its composition was analyzed by Gadolin and Arrhenius. It took several scientists and a considerable amount of time and perseverance to isolate all the different lanthanides in their pure form; such difficulty arises from the fact that these elements are characterized by very similar chemical properties and their chemical separation is not a trivial issue. Presently the lanthanides are obtained industrially by treating their ores monazite and bastnäsite with caustic soda and hydrochloric acid [39]; the resulting solutions of chlorides of the lanthanide ions are then subjected to column chromatography separating them according to decreasing atomic number, and the ions are eluted in the order Lu^{3+} to La^{3+}.

Lanthanide ions are most stable in the trivalent form (Ln^{3+}) and have a $[Xe]4f^n5s^25p^6$ electron configuration with n varying from 0 to 14 (Table III). Nevertheless, the oxidation states II (Ln^{2+}) or IV (Ln^{4+}) are especially observed when they lead to:

1. electronic configuration of Xe, i.e. Ce^{4+} (f^0)
2. an half-filled 4f-shell, i.e. Eu^{2+} and Tb^{4+} (f^7)
3. a completely filled 4f-shell, i.e. Yb^{2+} (f^{14})

In consequence of the *lanthanide contraction* phenomenon, in which the 4f-eigenfuction is contracted, the *f*-shell behaves as an inner shell and it is shielded by the filled $5s^25p^6$ sub-shells (Fig. 2.8).

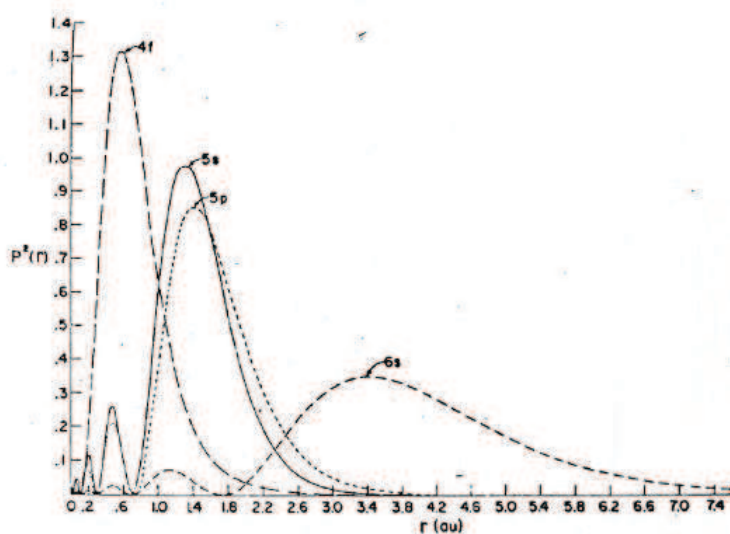**Fig. 2.8** Square of the radial wavefunction times the squared radius for the 4f, 5s, 5p and 6s electrons in Gd^+. For Ln^{3+} ions this picture will be contracted because of the larger effective nuclear charge.

Although this screening is small, *f*-electrons are weakly perturbed by charges of the surrounding ligands. They do not strongly interact with the environment and have little tendency to participate in chemical bond formation. The shielding of the 4*f* orbitals results in special spectroscopic properties with parity-forbidden 4*f*-4*f* absorption having very low molar absorption coefficients and characteristic narrow-line emission, mostly in the visible and near infrared ranges. The strategic importance of lanthanides is based on the unique optical and magnetic properties arising from the partly filled 4*f* shell. This has resulted in the widespread use of lanthanides in industrial and military applications. The optical properties are responsible for applications of lanthanides in lighting (fluorescent tubes, white light LEDs), displays (CRT, PDP), lasers, telecommunication (fiber amplifiers) and medical imaging (bio-labels, PET, CT). The magnetic properties are used in Nd, Tb and Sm based magnets with superior magnetic moments which find applications in e.g. wind turbines, hybrid cars and headsets. Other applications of lanthanides include catalysis (La, Ce), batteries (La), polishing agents (CeO_2), in metallurgy as additive to strengthen steel (mixture of lanthanide) and in glass to realize a higher refractive index.

Table III. Electronic configurations and Oxidation States of the Lanthanide Elements.

Element	Symbol	Electr. Conf. Ln	Electr. Config. Ln^{3+}	Oxidation States[1]	
Lanthanum	La	$[Xe]5d^16s^2$	$[Xe]$	**+III**	
Cerium	Ce	$[Xe]4f^15d^16s^2$	$[Xe]4f^1$	**+III**	+IV
Praseodymium	Pr	$[Xe]4f^35d^06s^2$	$[Xe]4f^2$	**+III**	(+IV)
Neodymium	Nd	$[Xe]4f^45d^06s^2$	$[Xe]4f^3$	(+II) **+III**	
Promethium	Pm	$[Xe]4f^55d^06s^2$	$[Xe]4f^4$	(+II) **+III**	
Samarium	Sm	$[Xe]4f^65d^06s^2$	$[Xe]4f^5$	(+II) **+III**	
Europium	Eu	$[Xe]4f^75d^06s^2$	$[Xe]4f^6$	+II **+III**	
Gadolinium	Gd	$[Xe]4f^75d^16s^2$	$[Xe]4f^7$	**+III**	
Terbium	Tb	$[Xe]4f^95d^06s^2$	$[Xe]4f^8$	**+III**	(+IV)
Dysprosium	Dy	$[Xe]4f^{10}5d^06s^2$	$[Xe]4f^9$	**+III**	(+IV)
Holmium	Ho	$[Xe]4f^{11}5d^06s^2$	$[Xe]4f^{10}$	**+III**	
Erbium	Er	$[Xe]4f^{12}5d^06s^2$	$[Xe]4f^{11}$	**+III**	
Thulium	Tm	$[Xe]4f^{13}5d^06s^2$	$[Xe]4f^{12}$	(+II) **+III**	
Ytterbium	Yb	$[Xe]4f^{14}5d^06s^2$	$[Xe]4f^{13}$	+II **+III**	
Lutetium	Lu	$[Xe]4f^{14}5d^16s^2$	$[Xe]4f^{14}$	**+III**	

[1] The most important oxidation states (commonly the most abundant and stable) are reported in bold. Other oxidation states, well characterized but less important, are reported in normal character. The less stable or still uncertain oxidation states are reported in brackets.

2.2.2.1 5d-4f transitions in lanthanide ions

More than a century of spectroscopy of lanthanide ions has involved detailed studies of the intraconfigurational 4f-4f transitions. Most of the aspects of these transitions are currently quite well understood. For the interconfigurational 5d-4f transitions the situation is more complicated. One of the reasons for this is the fact that these transitions are mainly located in the ultraviolet and vacuum ultraviolet spectral region, and were studied thoroughly only during the last two decades, triggered by an increased interest in the high-energy excited states of lanthanide ions. While the intraconfigurational 4f-4f transitions are electric-dipole forbidden and the corresponding luminescence decay times of the emitting $4f^n$ levels are typically in the μs to ms region, the interconfigurational 5d-4f transitions can be allowed and luminescence decay times in the ns time region are usually observed. For this reason 5d-4f emission of some lanthanide ions can be suitably exploited to realize new fast and advanced scintillation materials, especially for the medical diagnostic techniques where high timing resolution is required to improve the quality of the tomographic images.

The energy of the numerous 4f-levels of the lanthanides doped $LaCl_3$ can be found in the Dieke diagram (Fig. 2.9) [40] up to energies of 40000 cm^{-1}. In the last decade, the diagram has been extended into the vacuum ultraviolet region for the lanthanides in $LiYF_4$ by Meijerink et al. [41] (Fig. 2.10).

The positions of the $4f^{n-1}5d$ levels are much more influenced by the crystal field interaction than those of the $4f^n$ levels, which are well shielded from the crystalline environment. Due to the strong interaction of the 5d-electron with the neighboring anions in the compounds, the bonding strength changes upon 4f-5d excitation, giving broad absorption and emission bands instead of lines [42]. Typical bandwidths (full width at half maximum, FWHM) are 1000-4000 cm^{-1}. Efficient emission from $4f^{n-1}5d$ states has been observed for a limited number of lanthanide ions: Ce^{3+}, Pr^{3+}, Nd^{3+}, Er^{3+} and Tm^{3+}. The other lanthanide ions do not show 4f-5d emission due to the presence of $4f^n$ levels just below the lowest $4f^{n-1}5d$ state, allowing fast non-radiative relaxation to the $4f^n$ levels. For Er^{3+} ($4f^{11}$) and Tm^{3+} ($4f^{12}$) the dominant 5d-4f emission is from the high spin state and their emission decay time are in the μs range due to the spin-selection rule. This leaves Ce^{3+}, Pr^{3+} and Nd^{3+} as unique ions for which efficient and fast spin-allowed 5d-4f emission can be observed in the ns range. Of these three ions, the energy difference between the lowest 5d state and the 4f ground state is the smallest in Ce^{3+} (E ≤ 4.1 eV) and the largest in Nd^{3+} (E ~ 6.8 eV) [43]. At a smaller 5d-4f energy difference more compounds are suitable as potential host lattices. Fluorides, oxides and chlorides are characterized by a bandgap E_g of respectively 8-11, 4-7 and 5-8 eV. Accordingly the lowest 5d/4f levels of Ce^{3+} fit in all of these band gaps, those of Nd^{3+} practically only in fluorides,

and Pr^{3+} is an intermediate case. A schematic energetic diagram of energy levels of Ce^{3+}, Pr^{3+} and Nd^{3+} is shown in Fig. 2.11.
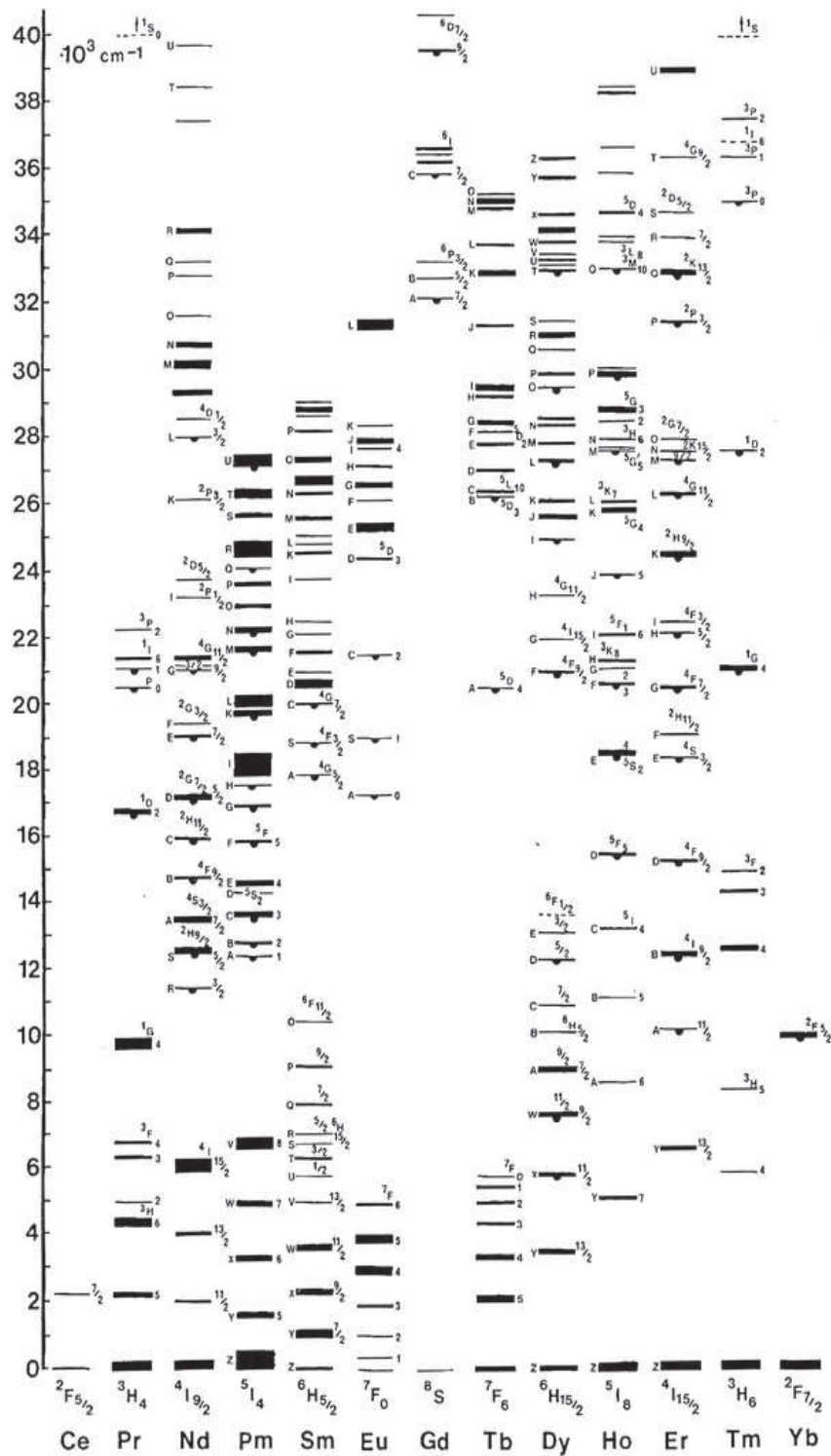

Fig. 2.9 Dieke's diagram of all observed $4f^n$ energy levels for trivalent lanthanide ions in $LaCl_3$ [40]. Levels from which emission was observed are indicated by a filled semicircle.
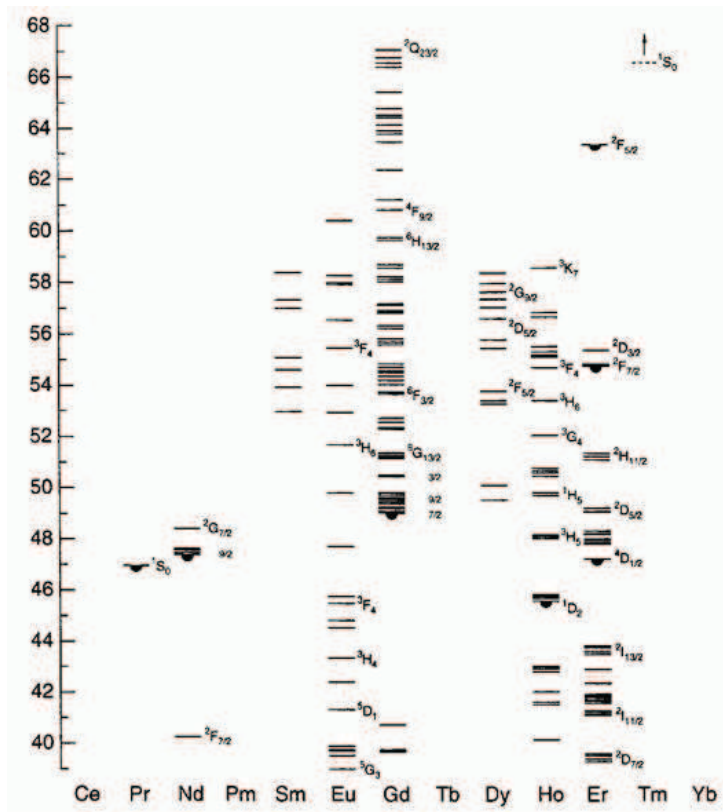
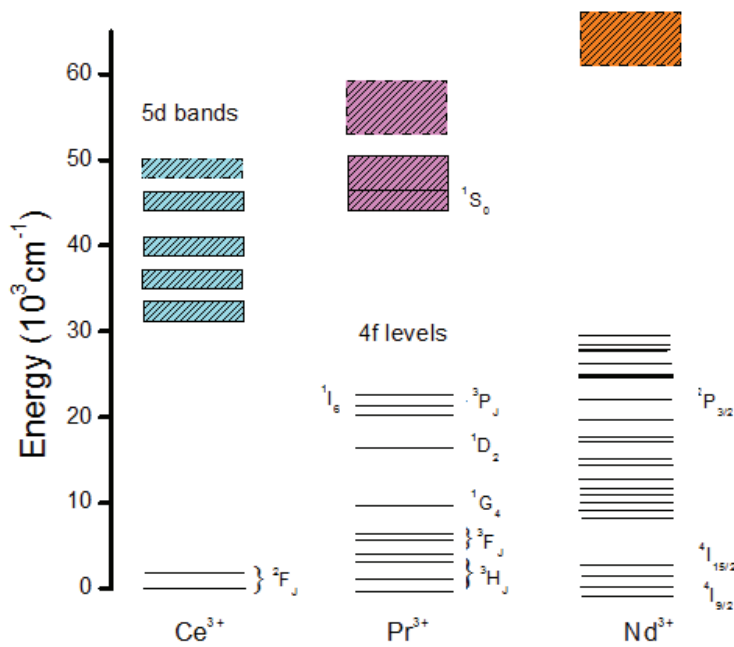**Fig. 2.10** Energy levels above 40000 cm^{-1} for the lanthanides in LiYF$_4$ [41].

Fig. 2.11 Energy levels of Ce^{3+}, Pr^{3+} and Nd^{3+} in a host lattice (adapted from [43]).

Configuration-coordinate diagram

The properties of a Ln^{3+} ion in a host lattice can be described more accurately by means of a configuration-coordinate diagram (Fig. 2.12). The configuration coordinate R is a measure of the distance between the lanthanide ion (Ln) and the neighbouring ions (L) of the host lattice. The potential energy of the lanthanide ion as a function of Q is represented by a parabola. This parabolic shape follows from the fact that the vibrational motion is assumed to be harmonic, i.e. the restoring force F is proportional to the displacement: $F = -k(Q-Q_0)$. A force of this form corresponds to a potential energy whose dependence on R is parabolic: $E = \frac{1}{2} \cdot k \cdot (Q-Q_0)^2$. The minimum Q_0 of the parabola corresponds to the equilibrium distance in the ground state. The quantum mechanical solution of this problem (known as harmonic oscillator) yields for the energy levels of the oscillator $E_v = (v + \frac{1}{2}) \cdot h \cdot v$, where v = 0, 1, 2, ..., h is the Plank constant and v is the frequency of the oscillator. Part of these levels are indicated in Fig. 2.12. For our purpose the more important information is that in the lowest vibrational level (v = 0) the highest probability of finding the system is at Q_0, whereas for high values of v it is at the turning points, i.e. at the edge of the parabola [44].

In optical absorption the centre is promoted from its ground state to an excited state. It is important to realize that electrons move much faster than rearranging nuclei therefore transitions (within a good approximation) take place in static surrounding (i.e. only in the vertical direction). The optical absorption starts from the lowest vibrational level, i.e. v = 0. Therefore, the most probable transition occurs at Q_0 where the vibrational wave function has its maximum value. The transition will end on the edge of the excited state parabola, since it is there that the vibrational levels of the excited state have their highest amplitude. This transition corresponds to the maximum of the absorption band. It is also possible, although less probable, to start at Q values larger or smaller than Q_0. This leads to the width of the absorption band because for $Q > Q_0$ the energy difference of the transition will be less than for $Q = Q_0$, and for $Q < Q_0$ it will be larger. If $Q = Q_0$, the two parabola lie exactly above each other and the band width of the optical transition vanishes: the absorption band becomes a narrow line.

After the absorption, the center return first to the lowest vibrational level of the excited state giving up the excess energy to the surroundings. The emission transition can be described in the same terms of that of absorption. From the lowest vibrational level of the excited state the system can return to the ground state spontaneously under emission of radiation. By emission, the center reaches a high vibrational state. Again relaxation occurs, but now to the lowest vibrational level of the ground state. The emission occurs at a lower energy than the absorption due to the relaxation processes. The energy difference between the maximum of the (lowest energy) excitation band and

that of the emission band is called Stokes shift. It will be immediately clear that the larger the value of ΔQ is, the larger the Stokes shift and the broader the optical bands involved.
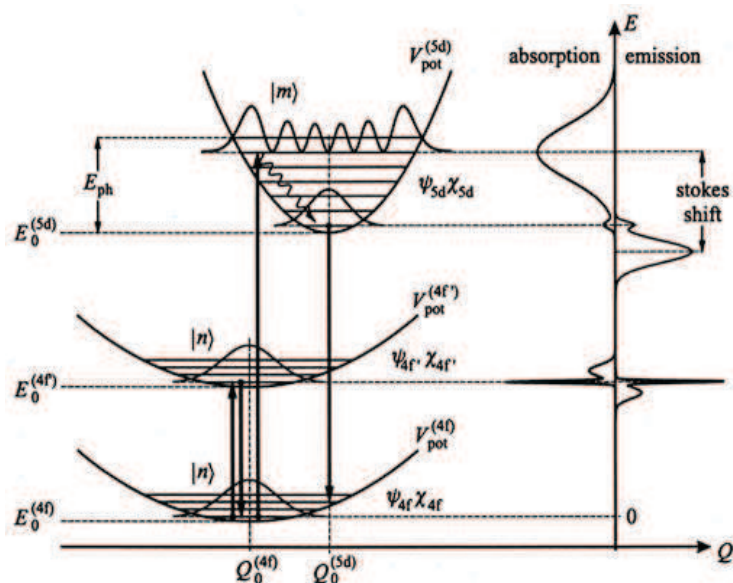

Fig. 2.12 Configuration coordinate diagram.

Excitation of a $4f$ electron to a $5d$ state involves a strong change in the Ln—L bond strength due to the strong interaction of the $5d$ orbitals with the surrounding ligands. As a result the equilibrium distance Ln—L changes much more ($\Delta Q \gg 0$) than observed for transitions between well shielded $4f$ states ($\Delta Q \sim 0$) and there is a strong coupling with vibrations, leading to strong vibronic transition both in absorption and emission. Actually the value of ΔQ represents a qualitative measure of the interaction between electrons and the vibrations of the optical center under consideration. It is usual to call the $\Delta Q = 0$ situation the weak coupling scheme, $\Delta Q > 0$ the intermediate coupling scheme, and $\Delta Q \gg 0$ the strong coupling scheme.

To support efficient $5d$-$4f$ transition, the ΔQ value should not be too large as thermal occupation of the crossing of the parabolas introduces quenching of the emission. On the other hand a ΔQ value too small could lead to an overlap between the absorption and emission band and re-absorption of an emitted photon by other lanthanide ions can occur. In general some re-absorption cannot be avoided [44].

Covalency and crystal field strength effects

Most of the scintillators presently used in CT and PET scanners are based on materials activated with Ce^{3+} ion, which exhibits efficient and relatively fast (~20-70 ns) 5d-4f electric-dipole emission

in a broad spectral range (400-600 nm) [45]. Taking into account that the radiative decay time increases as the second or third power of the emission wavelength, the possibility to use shorter emission wavelengths (in the blue or near UV spectral regions) can gives rise to faster time emission decays. For this reason recently much attention has been turned on the study of the 5d-4f emission of Pr^{3+} ions in wide band-gap compounds. The emitting 5d state of Pr^{3+} ions is located at about 12240 cm^{-1} higher energy than that for Ce^{3+} in the same host [46] and its emission lifetime is about 2-3 times shorter [30] allowing faster time responses for scintillators. As a result, the choice of the Pr^{3+} ion as an activator ion for wide band-gap hosts may constitute a promising alternative to the Ce^{3+} one in the development of new scintillator materials for applications requiring time-correlated registration of photons or working at higher count rate.

It is worth to point out that the position of the 5d-4f emission band strongly depends on both the covalence effect and the crystal field strength induced by the ligands (Fig. 2.12). As a result of covalent bonding between the 5d levels and the ligand orbitals, the 5d orbitals expand by partial delocalization over the ligands and consequently the energy is lowered. This effect is known with the name of *nephelauxetic effect* (from greek "cloud expanding") and it constitutes a qualitative measure of the covalency of the lanthanide-ligand bond. It was found that the common ligands can be ranked according to their ability to induce the expansion of the cloud. This order, which is almost independent of the central ion, strictly depends on the polarizibility of the ligand as well as the charge density on the surrounding anions.

The crystal field is responsible for the splitting of the 5d levels: the presence of ligands induces a splitting into a maximum of five crystal-field levels due to the differences in orientation of the d-orbitals with respect to the negatively charged ligands (Fig. 2.13). The splitting depends on the type and the distance of the ligands and the symmetry. Accordingly, for the same lanthanide ion the 5d-4f emission and thus the radiative decay time can vary strongly, depending on the type of host lattice.
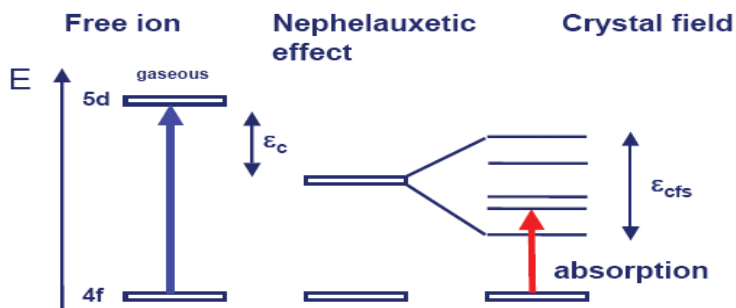

Fig. 2.13 Schematic representation of the influence of the covalence effect and the crystal field strength on the energy and the splitting of the 5d levels.

An illustrative example of these effects is clearly documented in [47] where the authors showed the shift exhibited by the lowest $5d$ energy level of Nd^{3+} ion by varying the type of the host lattice. Specifically, the authors observed that in phosphates MPO_4 and borates MBO_3 (where M = La, Y, Lu, Sc) the Nd^{3+} $4f^2 5d^1$ onset decreases in energy as the ionic radius of the metal ion decreases in the order Sc < Lu < Y < La, due to the increasing nephelauxetic effect. This causes the $4f^3$ energy levels to decrease as well, but to a much lesser degree. Furthermore, the smaller ionic radius causes an increase in the $5d$ crystal field splitting, lowering the $4f^2 5d^1$ onset even further. It was realized that when the energy gap between the lowest $4f^2 5d^1$ state and the $^2G(2)_{7/2}$ $(4f^3)$ state is 4000 cm^{-1} or less ($ScPO_4$ and all of the borates), efficient non-radiative relaxation occurred, populating the $^2G(2)_{9/2} (4f^3)$ state and leading to efficient radiation from this $4f^3$ level; conversely, when the energy gap is 7000 cm^{-1} or greater ($LaPO_4$) no non-radiative relaxation occurred, and fluorescence is observed only from the lowest $4f^2 5d^1$ state. For the systems $LuPO_4$ and YPO_4, which are characterized by an energy gap of about 5000 cm^{-1}, both competing processes occurred, so emission from both $4f^2 5d^1$ level and $^2G(2)_{9/2}$ are observed (Fig. 2.14).
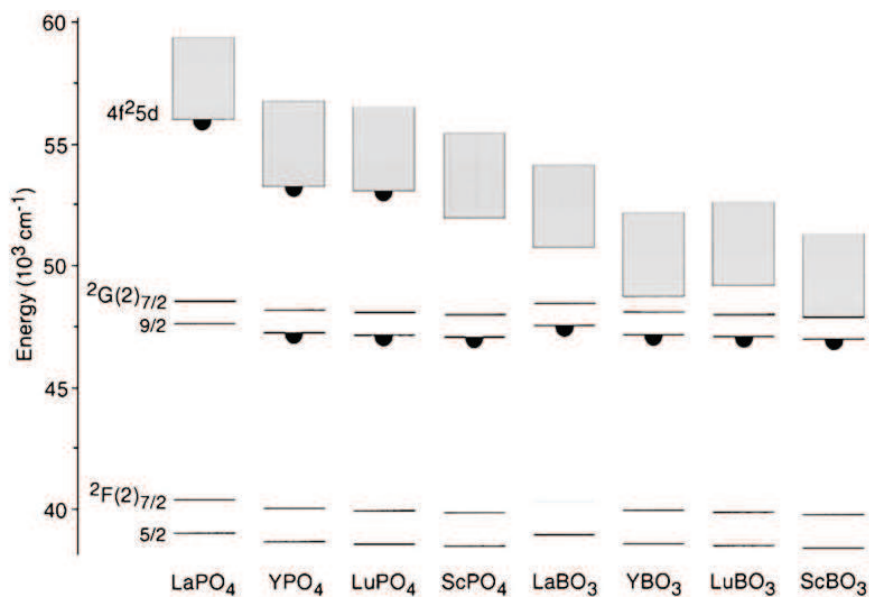
Fig. 2.14 Schematic energy level diagrams for Nd^{3+} in various MPO_4 and MBO_3 crystals, showing the positions of the $4f^2 5d$ and $^2G(2)_J$ levels (see [47] and references therein). Levels exhibiting emission are marked by a semicircle.

Also for the Pr^{3+} dopant ion the nephelauxetic effect and the crystal field strength are crucial to determine the efficiency of the scintillation process [48]. After high energetic excitation, for trivalent praseodymium two type of emission transitions can take place, i.e. either $4f5d \rightarrow 4f^2$ or

$4f^2 \rightarrow 4f^2$. The type of transition depends on the host lattice and the energetic location of states of the $4f5d$ electron configuration relative to the $^1S_0$ level of the $4f^2$ electron configuration, which is located at about 46500-46900 cm^{-1}. In the case the energetically extended $4f5d$ states overlap with the $^1S_0$ level (or are even energetically lower), the high-energetic excitation brings about the emission from the lowest state of the $4f5d$ configuration characterized by broad emission bands with emission lifetimes in the order of tens of nanoseconds. An efficient cascade emission due to the two-step intra-configurational $4f^2$-$4f^2$ transitions ($^1S_0 \rightarrow {}^1I_6$ followed by $^3P_0 \rightarrow {}^3H_4$) can occur after high-energetic excitation, if the $^1S_0$ level is located energetically lower than the lowest state of the $4f5d$ configuration (Fig. 2.15). This latter kind of emission has been observed mainly in fluoride hosts, where the high electronegativity of fluoride ions induces a small barycenter shift of the whole $4f5d$ electronic configuration.
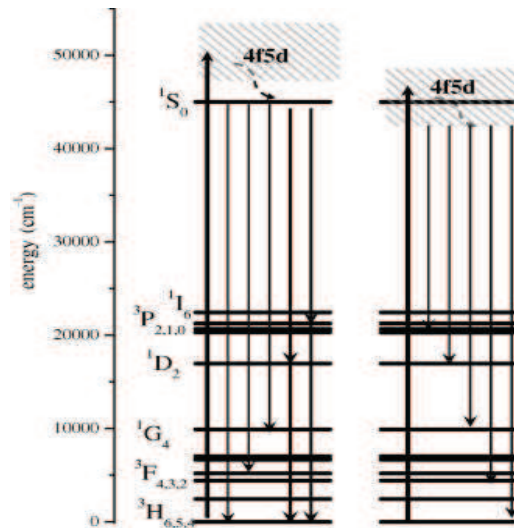
Fig. 2.15 Energy level scheme of Pr^{3+} showing the 4f^2 levels and two possibilities for the position of the $4f5d$ levels. On the left the lowest $4f5d$ level is above the $^1S_0$ level making quantum cutting from the $^1S_0$ level possible. On the right the $4f5d$ level is situated below the $^1S_0$ level and fast UV $5d$ emission to the lower $4f^2$ levels is possible potentially being a good scintillator.

As documented by S. Kück *et al* in [48], there are general considerations to evaluate, whether a host material lead to a $4f5d \rightarrow 4f^2$ (scintillation process) or $4f^2 \rightarrow 4f^2$ (quantum cutting) emission of the Pr^{3+} ion. From the physical point of view, a high coordination number of the Pr^{3+} ion generally leads to a small crystal field splitting of the $4f5d$ states, due to the fact that for a higher number of nearest neighbors, the spherical-symmetric part ε_0 of the perturbation increases, whereas the non-spherical-symmetric parte decreases:

$$\varepsilon_0\ (6) = \tfrac{3}{4}\varepsilon_0(8) = \tfrac{1}{2}\varepsilon_0(12) \tag{2.6}$$

$$\Delta(6) = -\tfrac{9}{8}\Delta(8) = -2\Delta(12) \tag{2.7}$$

where $\Delta = 10Dq$ is a measure for the energetic splitting and the number in brackets represents the coordination number (6 : octahedron, 8 : cube, 12 : cube-octahedron). As a result, for higher coordination numbers, the whole $4f5d$-configuration is elevated and the splitting is reduced. This prevents the possibility of observing a direct $4f5d \rightarrow 4f^2$ emission upon high-energetic excitation.

In addition to this, there is another important approach to estimate the energetic position of the lowest 5d state of Pr^{3+} ion in an appropriate host lattice in order to know the energetic separation from this latter to $^1S_0$ level, and thus to understand the most probable mechanism of energy relaxation after high-energetic excitation. This approach is based on the preliminary knowledge of the energy level scheme of Ce^{3+} ion, which is the most extensively investigated ion for scintillating materials. From the energetic position of the lowest $5d$ level in Ce^{3+}-doped materials, the energetic position of the lowest $5d$ level of Pr^{3+} ion in the same host can be simply estimated by the Dorenbos' relation [46]:

$$E\ [Pr^{3+},\ 5d] = E\ [Ce^{3+},\ 5d] + 12240\ \mathrm{cm}^{-1} \pm 750\ \mathrm{cm}^{-1} \tag{2.8}$$

where E is the energy of the lowest $5d$ level of Pr^{3+} and Ce^{3+}, respectively.

In similar way we can estimate the energy position of the lowest $5d$ levels for other lanthanide ions. For instance, for Nd^{3+} ion, which is another possible luminescent candidate for scintillator materials, the lowest 5d state in a generic host is estimated to be localized at:

$$E\ [Nd^{3+},\ 5d] = E\ [Ce^{3+},\ 5d] + 22700\ \mathrm{cm}^{-1} \pm 650\ \mathrm{cm}^{-1} \tag{2.9}$$

The lowest $5d$ state of Nd^{3+} is generally located in the deep UV (see. Fig. 2.11), so the prevision of the energy location of the lowest $5d$ state (by the equation 2.9) is particularly important not only to know the energy location of the above-mentioned level from the lower lying $4f$ level, but also to identify if 5d level can lie within the conduction band of the host lattice. In this latter case Nd^{3+} ion will not be able to produce any luminescence and it cannot be used for the realization of scintillating materials.

References

1.   Lecoq, P. and M. Korzhik, *Scintillator developments for high energy physics and medical imaging.* Nuclear Science, IEEE Transactions on, 2000. **47**(4): p. 1311-1314.

2.   *New Grolier Multimedia Encyclopedia*, N.Y.N. Grolier Inc., USA, Editor. 1993.

3.   C., B.S., *Radiologic Science for Technologists*, ed. U. Mosby C. V. St. Louis MO. 1975.

4.   Rutherford, E., J. Chadwick, and C.D. Ellis, *Radiations from radioactive substances*. 1930: The University press.

5.   Hofstadter, R., *Alkali Halide Scintillation Counters.* Physical Review, 1948. **74**(1): p. 100-101.

6.   Menefee, J., C.F. Swinehart, and E.W. O'Dell, *Calcium Fluoride as an X-Ray and Charged Particle Detector.* Nuclear Science, IEEE Transactions on, 1966. **13**(1): p. 720-724.

7.   Farukhi, M.R. and C.F. Swinehart, *Barium Fluoride as a Gamma Ray and Charged Particle Detector.* Nuclear Science, IEEE Transactions on, 1971. **18**(1): p. 200-204.

8.   Weber, M.J. and R.R. Monchamp, *Luminescence of $Bi_4Ge_3O_{12}$: Spectral and decay properties.* Journal of Applied Physics, 1973. **44**(12): p. 5495-5499.

9.   Cho, Z.H. and M.R. Farukhi, *Bismuth Germanate as a Potential Scintillation Detector in Positron Cameras.* Journal of Nuclear Medicine, 1977. **18**(8): p. 840-844.

10.   Lecoq, P., *The high energy physics demand for a new generation of scintillators.* Journal of Luminescence, 1994. **60–61**(0): p. 948-955.

11.   Melcher, C.L. and J.S. Schweitzer, *A promising new scintillator: cerium-doped lutetium oxyorthosilicate.* Nuclear Instruments and Methods in Physics Research Section A: Accelerators, Spectrometers, Detectors and Associated Equipment, 1992. **314**(1): p. 212-214.

12.   Lempicki, A., et al., *$LuAlO_3$:Ce and other aluminate scintillators.* Nuclear Science, IEEE Transactions on, 1995. **42**(4): p. 280-284.

13.   Lempicki, A., et al., *Cerium-doped orthophosphates: new promising scintillators.* Nuclear Science, IEEE Transactions on, 1993. **40**(4): p. 384-387.

14.   Khodyuk, I.V. and P. Dorenbos, *Nonproportional response of $LaBr_3$:Ce and $LaCl_3$:Ce scintillators to synchrotron x-ray irradiation.* Journal of Physics: Condensed Matter, 2010. **22**(48): p. 485402.

15.   Weber, M.J., *Inorganic scintillators: today and tomorrow.* Journal of Luminescence, 2002. **100**(1–4): p. 35-45.

16.   Cooper, L.N., *An introduction to the meaning and structure of physics*. 1970: Harper & Row.

17.   Brixner, L.H., *New X-ray phosphors*. Materials Chemistry and Physics, 1987. **16**(3–4): p. 253-281.

18.   Liu, B. and C.S. Shi, *Development of medical scintillator*. Chinese Science Bulletin, 2002. **47**(13): p. 1057-1063.

19.   Liu, B. and C. Shi, *Development of medical scintillator*. Chinese Science Bulletin, 2002. **47**(13): p. 1057-1063.

20.   Rodnyi, P.A., *Progress in fast scintillators*. Radiation Measurements, 2001. **33**(5): p. 605-614.

21.   Blasse, G., *Scintillator Materials*. Chemistry of Materials, 1994. **6**(9): p. 1465-1475.

22.   Shockley, W., *Problems related top-n junctions in silicon*. Cechoslovackij fiziceskij zurnal B, 1961. **11**(2): p. 81-121.

23.   Robbins, D.J., *On Predicting the Maximum Efficiency of Phosphor Systems Excited by Ionizing Radiation*. Journal of The Electrochemical Society, 1980. **127**(12): p. 2694-2702.

24.   Holstein, T., *Imprisonment of Resonance Radiation in Gases*. Physical Review, 1947. **72**(12): p. 1212-1233.

25.   Bizarri, G., *Scintillation mechanisms of inorganic materials: From crystal characteristics to scintillation properties*. Journal of Crystal Growth, 2010. **312**(8): p. 1213-1215.

26.   Bizarri, G. and P. Dorenbos, *Charge carrier and exciton dynamics in $LaBr_3:Ce^{3+}$ scintillators: Experiment and model*. Physical Review B, 2007. **75**(18): p. 184302.

27.   Vasil'ev, A.N., et al., *Theoretical investigations on the high light yield of the $LuI_3:Ce$ scintillator*. Journal of Luminescence, 2009. **129**(12): p. 1555-1559.

28.   Dorenbos, P. and C.W.E. van Eijk, *SCINT 95: proceedings of the International Conference on Inorganic Scintillators and Their Applications : Delft, The Netherlands, August 28-September 1, 1995*. 1996: Delft University Press.

29.   Koepke, C., A. Lempicki, and A.J. Wojtowicz, *Luminescence Quenching of Strongly Coupled Systems*. physica status solidi (b), 1993. **179**(1): p. 233-240.

30.   Henderson, B. and G.F. Imbusch, *Optical Spectroscopy of Inorganic Solids*. 2006: Clarendon Press.

31.   van Eijk , C.W.E., *Instrumentation for Detection of Radiation*. Radiation Protection Dosimetry, 1998. **77**(4): p. 245-252.

32.   Murty, R.C., *Effective Atomic Numbers of Heterogeneous Materials*. Nature, 1965. **207**(4995): p. 398-399.

33. Bearden, J.A. and A.F. Burr, *Reevaluation of X-Ray Atomic Energy Levels.* Reviews of Modern Physics, 1967. **39**(1): p. 125-142.

34. Nikl, M., V.V. Laguta, and A. Vedda, *Complex oxide scintillators: Material defects and scintillation performance.* physica status solidi (b), 2008. **245**(9): p. 1701-1722.

35. Greskovich, C. and S. Duclos, *CERAMIC SCINTILLATORS.* Annual Review of Materials Science, 1997. **27**(1): p. 69-88.

36. Klassen, N.V., et al., *Advantages and Problems of Nanocrystalline Scintillators.* Nuclear Science, IEEE Transactions on, 2008. **55**(3): p. 1536-1541.

37. Dujardin, C., et al., *Luminescence and Scintillation Properties at the Nanoscale.* Nuclear Science, IEEE Transactions on, 2010. **57**(3): p. 1348-1354.

38. Lide, D.R., *CRC Handbook of Chemistry and Physics, 85th Edition.* 2004: Taylor & Francis.

39. Housecroft, C.E. and A.G. Sharpe, *Inorganic Chemistry.* 2005: Pearson Prentice Hall.

40. Dieke, G.H., H.M. Crosswhite, and H. Crosswhite, *Spectra and energy levels of rare earth ions in crystals.* 1968: Interscience Publishers.

41. Meijerink, A. and R.T. Wegh, *VUV spectroscopy of lanthanides: Extending the horizon.* Rare Earths '98, 1999. **315-3**: p. 11-26.

42. Dorenbos, P., *The $4f^n \leftrightarrow 4f^{n-1}5d$ transitions of the trivalent lanthanides in halogenides and chalcogenides.* Journal of Luminescence, 2000. **91**(1–2): p. 91-106.

43. Vaneijk, C.W.E., P. Dorenbos, and R. Visser, *Nd(3+) and Pr(3+) Doped Inorganic Scintillators.* Ieee Transactions on Nuclear Science, 1994. **41**(4): p. 738-741.

44. Blasse, G. and B.C. Grabmaier, *Luminescent materials.* 1994: Springer-Verlag.

45. Korzhik, M., et al., *Development of scintillation materials for PET scanners.* Nuclear Instruments and Methods in Physics Research Section A: Accelerators, Spectrometers, Detectors and Associated Equipment, 2007. **571**(1–2): p. 122-125.

46. Dorenbos, P., *The 5d level positions of the trivalent lanthanides in inorganic compounds.* Journal of Luminescence, 2000. **91**(3–4): p. 155-176.

47. Burdick, G.W. and M.F. Reid, *Chapter 232 – transitions*, in *Handbook on the Physics and Chemistry of Rare Earths*, J.-C.B. Karl A. Gschneidner and K.P. Vitalij, Editors. 2007, Elsevier. p. 61-98.

48. Kück, S., et al., *Photon cascade emission in Pr^{3+}-doped fluorides.* Journal of Luminescence, 2003. **102–103**(0): p. 176-181.

Chapter 3

Experimental

3.1 Material synthesis

The materials investigated in this thesis were synthesized mainly by solid-state reaction and sol-gel process. It is our intention to briefly discuss the key points of these preparation methodologies.

3.1.1 Solid State Reaction (SSR) [1]

The solid state reaction route is the most widely used method for the preparation of polycrystalline solids from a mixture of solid starting materials. Solids do not react together at room temperature over normal time scales and it is necessary to heat them to much higher temperatures, often to 1000 to 1500 °C in order for the reaction to occur at an appreciable rate.

In order to understand the difference between reactions in solution and in the solid state, and the problem associated with the solid-state reactions, we have to consider the thermal reaction of two crystals of the compounds A and B which are in intimate contact across one face (Fig. 3.1) When no melt is formed during the reaction, the reaction has to occur initially at the points of contact between A and B, and later by the diffusion of the constituents through the product phase.

The first stage of the reaction is the formation of nuclei of the product phase C at the interface between A and B . This may be difficult, if a high degree of structural reorganization is necessary to form the product. After nucleation of product C has occurred, a product layer is formed. At this stage, there are two reaction interfaces: one between A and C, and another between C and B. In order of further reaction to occur, counter-diffusion of ions from A and B must occur through the existing product layer C to the new reaction interfaces. As the reaction progresses, the product layer becomes thicker. This results in increasingly longer diffusion paths and slower reaction rates, because the product layer between the reacting particles acts as barrier. In the simple case where

the rate of the reaction is controlled by lattice diffusion through a planar layer, the rate law has a parabolic form:

$$\frac{dx}{dt} = k \cdot x^{-1} \tag{3.1}$$

where x is the amount of the reaction (here equal to the thickness of the growing product layer), t is the time, and k is the rate constant.
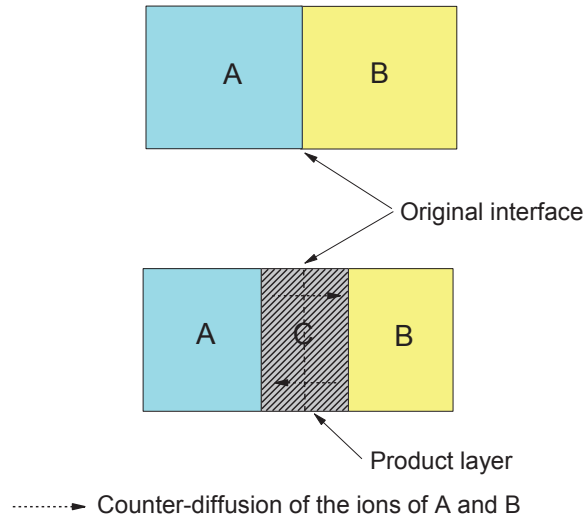

Fig 3.1 Reaction of two crystals (A and B) sharing one face. After initial formation of a product layer C, ions from A and B have to counter-diffuse through the product layer to form new product at the intefaces A/C and B/C (adapted from [1]).

Ions are normally regarded as being trapped on their appropriate lattice sites, and it is difficult for them to move to adjacent sites. Only at very high temperatures the ions have sufficient energy to diffuse through the crystal lattice. As a rule of thumb, two-thirds of the melting temperature of one component are sufficient to activate diffusion sufficiently and hence to enable the solid-state reaction.

The formation of the perovskite barium titanate ($BaTiO_3$) by solid-state reaction of $BaCO_3$ and TiO_2 may serve as an example to illustrate this point, but also to show that such considerations are sometimes oversimplifying the facts. $BaTiO_3$ is an important material for the fabrication of thermistors, capacitors and otpoelectronic devices. BaO (formed by decomposition of $BaCO_3$) has the rock salt structure (cubic close packing of the oxide ions, Ba^{2+} ions in octahedral sites), while TiO_2 (rutile structure) has a hexagonal close packing of the oxide ions and Ti^{4+} ions in half of the octahedral sites. The formation of $BaTiO_3$ takes place in at least three stages:

1. First BaO reacts with the outer surface regions of TiO_2 grains to form nuclei and a surface layer. This require reorganization of the oxide lattice at the $TiO_2/BaTiO_3$ interface.

2. Further reaction of BaO and the previously formed $BaTiO_3$ leads to the formation of the intermediate Ba-rich phase Ba_2TiO_4. The formation of this phase is necessary for the migration of Ba^{2+} ions.

3. Ba^{2+} ions from the Ba-rich phase Ba_2TiO_4 migrate into the remaining TiO_2 to form $BaTiO_3$.

From the above discussion it is clear that reaction between two solids may not occur even if thermodynamic considerations favor product formation. There are three important factors that influence the rate of reaction between solids:

1. The area of contact between the reacting solids and hence their surface areas.
2. The rate of nucleation of the product phase.
3. The rate of diffusion of ions through the various phases, and especially through the product phase.

Apart from the problem arising from nucleation and diffusion, the ceramic methods suffer from several additional disadvantages:

- ✓ formation of the undesirable phases;
- ✓ the homogeneous distribution of dopants is sometimes difficult to achieve;
- ✓ there are limited possibilities for an *in-situ* monitoring of the progress of the reaction;
- ✓ in many systems the reaction temperature cannot be raised as high as necessary for reasonable reaction rates, because one or more components of the reacting mixture may volatilize.

Additional information about the theoretical aspects of the solid-state reaction are extensively dealt in [1-3].

The basic steps involved in conventional solid-state route are described as follow:

i. Accurately weighing of high purity starting materials, fine grain powders, in stoichiometric proportion;

ii. grinding and mixing of the reactants by using an agata mortar with pestle (or ball milling) till complete homogeneity in colour and consistency; in some cases it is possible to use an inert dispersion medium such as ethanol or acetone;

iii. pressing of the powders under a pressure of about 10 tons to form a uniform and compact pellet;

iv. calcination of the pellet at high temperatures in air or inert conditions by using a muffle furnace; in several cases the calcination process is repeated twice (or more times) with intermediated grinding.

3.1.2 Sol-gel process

In the last decade research has been focusing more on improving the performances of known scintillators rather than developing new materials. It appears that a good way to improve scintillators is to get a control of the materials on the nanometric scale. It is indeed very important to control the size of the grains in case of powders and to control the dispersion of the doping ions in the host. For luminescent materials, this latter requirement is crucial since the light emission is usually due to doping ions like rare earths or transition metal ions. Quenching concentration is usually found to be higher for sol-gel derived materials because of better dispersion of doping ions and thus higher average distance between emitting centers. In addition, the high versatility of the sol-gel process allows to reach various compositions and to vary the nature and the concentration of the doping ions easily. Materials prepared by sol-gel chemistry are also usually obtained at temperatures much lower than those required for traditional solid-state chemistry.

The sol-gel process allows the obtainment of solid products by gelation rather than by crystallization or precipitation. The sol-gel process can be described as the creation of an oxide network by progressive polycondensation reactions or molecular precursors in a liquid medium, or as a process to form materials via sol, gelation of the sol and finally removal of the solvent. This method is considered as a "chimie douce" or soft chemical approach to the synthesis of metastable (amorphous) oxide materials.

Before turning to the mechanisms by which solids are eventually formed, the processing steps and applications of the final materials, the terms "sol" and "gel" must be defined:

✓ a *sol* is a stable suspension of colloidal solid particles or polymers in a liquid;

✓ a *gel* consists of a porous, three-dimensionally continuous solid network surrounding and supporting a continuous liquid phase ("wet gel"). In general, the sol particles can be connected by covalent bond, van der Waals forces, or hydrogen bonds. Gels can also be formed by entanglement of polymer chains. In most sol-gel systems used for materials synthesis, gelation (= formation of the gels) is due to the formation of

covalent bonds and irreversible. Gel formation can be reversible when other bonds are involved in gelation.

Figure 3.2 presents a scheme of the different processing routes leading from the sol a variety of materials:

- thin layers (films) are applied by spin-coating or dip-coating;
- by moulding the "sol" we obtain a wet gel that:
  - will form a dense ceramic structure after evaporation and heat treatment;
  - under super critical conditions, it will form a very porous material with an extremely low density (aerogel);
- by adjusting the sol viscosity it is possible to manufacture ceramic fibres;
- by precipitation, spray pyrolysis or emulsion techniques we will obtain ultra-fine and uniform ceramic powders.
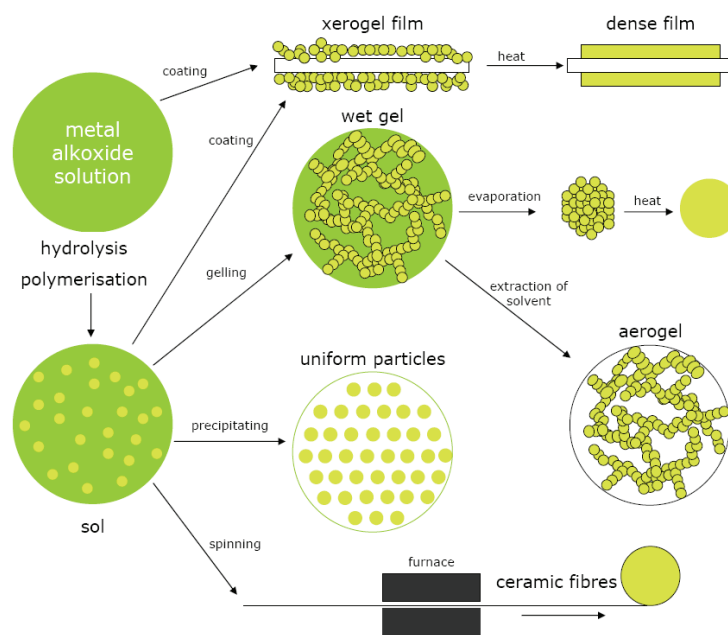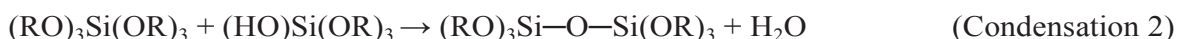

Fig. 3.2 Sol gel processing options

In this thesis, the sol gel process has been exploited to obtained some silicate materials, i.e. Lu_2SiO_5 and Y_2SiO_5. The coordination number of silicon is generally four, although coordination expansion can occur in transition states. Compared to the transition metals, silicon is less electropositive and therefore it is not very susceptible for a nucleophilic attack. This makes silicon compounds quite stable and easy to handle.

The sol-gel process involving silicon alkoxide can be described in two steps, the hydrolysis of the alkoxide and its polycondensation. For a given alkoxide of general formula $Si(OR)_4$, R being an alkyl chain, these reactions can be written as follows:

$$Si(OR)_4 + H_2O \rightarrow (HO)Si(OR)_3 + R\!-\!OH \qquad\qquad\qquad \text{(Hydrolysis)}$$

$$(HO)Si(OR)_3 + Si(OR)_4 \rightarrow (RO)_3Si\!-\!O\!-\!Si(OR)_3 + R\!-\!OH \qquad \text{(Condensation 1)}$$

$$(RO)_3Si(OR)_3 + (HO)Si(OR)_3 \rightarrow (RO)_3Si\!-\!O\!-\!Si(OR)_3 + H_2O \qquad \text{(Condensation 2)}$$

Usually, silicon alkoxides are very stable against hydrolysis. Step 1 thus requires catalysis usually performed by using acids or bases. Excellent review can be found in [4]. Briefly, base-catalyzed hydrolysis occur through an S_N2 mechanism involving a 5-fold coordinated silicon atom. On the other hand, acid catalysis proceeds through a limiting step corresponding to the protonation of an oxygen atom resulting in an S_N1 mechanism. Acid catalysis leads to a much quicker hydrolysis than basic catalysis resulting in different structures for the gels networks.

3.2 Instrumental setup

3.2.1 Synchrotron VUV spectroscopy measurements (DESY)

DESY (**D**eutsches **E**lektronen **S**ynchrotron) is a renowned synchrotron facility located in Hamburg, Germany, which was established on 18 December 1959. The experimental measurements presented in this thesis were performed at the HASYLAB (**Ha**mburger **S**ynchrotronstrahlungs**lab**or) laboratory at the Superlumi (I) station, using the radiation from the DORIS (**Do**ppel-**R**ing-**S**peicher) III storage ring. The setup consists of a positron storage ring where positrons are accelerated using a series of linear accelerators (linac), bending magnets and wigglers. The Superlumi station (Fig. 3.3) is a beamline of choice when it comes to VUV luminescence with very good spectral resolution in the excitation mode (~0.02 nm) and a very good timing resolution of the emission decay measurements (320 ps). The description of the entire setup can be found in the paper by Zimmerer [5]. The accessible spectral range, depending on the monochromator-detector combination, is 115-750 nm for emission and 50-335 nm for excitation spectra. Using a liquid-nitrogen-cooled CCD camera one can extend the range of the emission

measured to about 1050 nm. Reflectance spectra can also be measured at Superlumi station. Reflectance spectra can also be measured at Superlumi Station.
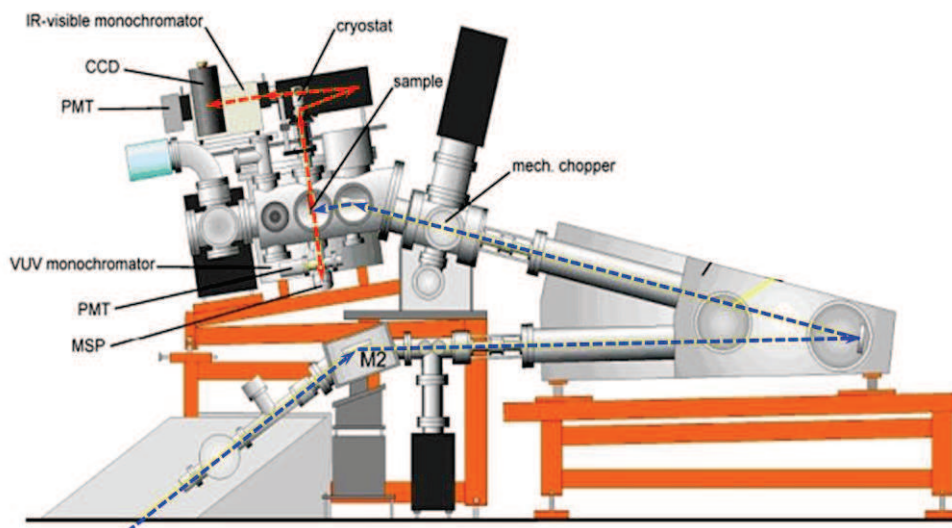

Fig. 3.3 Schematic representation of the Superlumi beamline at DESY synchrotron in Hamburg. The excitation beam from the DORIS storage ring passes through a high resolution primary monochromator. Different emission monochromators and detectors are shown.

The excitation source is pulsed and the typical number of bunches (or the number of positron packages traveling in the ring at the same time) selected in our experiments was *2* or *5* or *10*, depending on the setting; the time interval between the incoming bunches is 480 ns, or 192 ns, or 96 ns, respectively. These latter time values also correspond to the maximum timescale for the decay measurements in the three possible bunches modes used. Such time intervals are a result of the positron travelling with a speed very close to the speed of the light ($3 \cdot 10^5$ Km/s) in a storage ring of circumference of 289.2 m; this means that a single bunch of positrons takes 0.964 µs to travel around the ring one time. The maximum initial current in the ring is about 150 mA. The current translates to the intensity of the incident beam of the synchrotron radiation and decrease linearly in the time with the intensity.

The luminescence spectra can be measured in two distinct time windows ,TWs, fast and slow, making it possible to discriminate between fast and slow emissions. In case of the *2* bunches mode the times windows are set to select the signal within 4-35 (fast TW) and 248-415 ns (slow TW) relative to the beginning of SR pulse. At *5* bunches mode fast and slow TWs are set at 2-13 ns and

120-170 ns, respectively, whilst in case of *10* bunches mode the time windows are restricted to 2-11 ns and 50-61 ns, respectively.

Luminescence decay curves are recorded using time correlated photon counting with a time resolution of about 300 ps with a pulse length of about 130 ps. Time to Amplitude Conversion (TAC) is used for signal detection. TAC relies on ramping up a voltage linear in time after a trigger, simultaneously with the excitation pulse (the start pulse). When the detector measures a photon, a stop pulse is generated and the ramping of the voltage stops. The voltage is now a measure of the time elapsed between the excitation pulse and the emission of a photon. By measuring the voltage for many pulses and plotting the frequency for a voltage interval versus the voltage, a decay curve is obtained.

The measurements were performed in the ultra-high-vacuum (UHV) chamber ($\sim 10^{-9}$ mbar) in the temperature range of 8-300 K. The excitation spectra were corrected for the wavelength-dependent variation of the SR intensity using the sodium salicylate (NaSal) signal. A background signal corresponding to the dark count of the MCP detector was subtracted from the original spectra and decay curves.

3.2.2 X-ray powder diffraction (XRPD)

X-ray powder diffraction is a powerful technique primarily used for phase identification of a crystalline material and can provide information on unit cell dimensions. The analyzed material is finely ground, homogenized, and average bulk composition is determined.

X-ray powder diffraction is based on constructive interference of monochromatic X-rays and the electrons of the atoms of a polycrystalline compound. These X-rays are generated by a cathode ray tube, filtered to produce monochromatic radiation, collimated and directed toward the sample. The interaction of the incident rays with the sample produces constructive interference (and a diffracted ray) when conditions satisfy Bragg's Law:

$n\lambda = 2d \sin \theta$ (3.2)

where *n* is an integer, λ is the wavelength of incident wave, *d* is the spacing between the planes in the atomic lattice, and θ is the angle between the incident ray and the scattering planes.

This law relates the wavelength of electromagnetic radiation to the diffraction angle and the lattice spacing in a crystalline sample. These diffracted X-rays are then detected, processed and counted. By scanning the sample through a range of 2θ angles, all possible diffraction directions of

the lattice should be attained due to the random orientation of the powdered material. Conversion of the diffraction peaks to *d*-spacings allows identification of the compound because each material has a set of unique *d*-spacings. Typically, this is achieved by comparison of d-spacings with standard reference patterns.

Because the positions of the peaks in a powder pattern are determined by the size, shape, and symmetry of the unit cell and the peak intensities are determined by the arrangement of atoms within the cell, the powder pattern is a characteristic "fingerprint" of a phase. In a mixture of phases, the diffraction patterns overlap (but do not otherwise interfere), so it is possible to identify the components of a mixture. In practice, the experimental powder pattern is searched against the Powder Diffraction File, a database containing the patterns of > 700000 pure compounds, produced by the International Centre for Diffraction Data (www.icdd.com).

As the concentration of a phase in a mixture varies, the intensities of all of the peaks from this phase vary in concert (ideally). Thus, the concentrations of phases in a mixture can be determined by measuring the intensities of peaks in the powder pattern by the Rietveld refinement. In a Rietveld refinement, we use the crystal structures of all of the phases and diffraction physics to do a least-squares modeling of the full diffraction pattern. Among the refined parameters are scale factors for each phase, from which the quantitative analysis is derived. The Rietveld method corrects for and/or models many of the systematic errors that can plague a powder pattern, and thus can yield more accurate and more precise results than traditional methods. With normal care, accuracy and precision of about ±2 wt% can be achieved, and with additional effort, accuracy and precision as good as ±0.1 wt% can be attained. When an internal standard is added to the sample, the concentration of amorphous material can also be quantified.

The widths and shapes of the peaks in a powder pattern are determined by many factors, including contributions both from the diffractometer and the specimen. Once the instrumental factors are understood by measuring a sample having no size or strain broadening, the crystallite size and microstrain can be determined from the experimental peak widths.

As the crystallites (coherently scattering domains, not necessarily the same size as the particles) get smaller, the diffraction peaks get broader. Using the know diffraction physics, we can work backward, and compute the average crystallite size from the observed peak widths. An "infinite" crystallite is ~2000 Å in diameter, and by the time the crystallites get as small as 30-50 Å the peaks are hard to see. So, for nanocrystalline and microcrystalline materials, accurate crystallite sizes can be obtained using X-ray diffraction. A common application is studying the sintering of metals in

supported catalysts. For simple materials, even crystallite size distributions can be derived by analyzing the details of the peak shapes.

Microstrain broadening is the result of small changes in local lattice parameters resulting from defects, imperfections, and variations in the crystal structure. Solid solutions often exhibit microstrain broadening. The absolute value of mictostrain broadening may be hard to interpret, but changes in such broadening are often important practically. The dependence of mictostrain broadening with diffraction angle is different than that of size broadening, so the two effects can be separated, if a large enough range of diffraction angle is observed.

The X-ray powder pattern of a compound provides a convenient and characteristic fingerprint which can be used in qualitative analysis. Precise values of the d-spacing (which are properties of the materials itself, independent of the X-ray wavelength) and of estimated line intensities can be compared with those listed in the International Centre for Diffraction Data (ICDD), which contains thousands of X-ray powder patterns. Besides the routine identification of the phases, by X-ray powder diffractometer it is possible to determine their proportions by comparing the intensities of characteristic lines from each phase. Another important application concern the precise determination of the lattice parameters which contribute towards the overall characterization of a compound and the size of the particles

X-ray diffraction patterns of the compounds dealt in this thesis were measured with a Thermo ARL X′TRA powder diffractometer, operating in the Bragg-Brentano geometry and equipped with a Cu-anode X-ray source (K_α, λ = 1.5418 Å) with a Peltier Si(Li) cooled solid state detector (Fig. 3.4). The XRD patterns were collected with a scan rate of 0.4°/s and an exposure time of 0.72 s in the 5-90° 2θ range. The phase identification was performed with the PDF-4+ 2011 database supplied by the International Centre for Diffraction Data (ICDD). Polycrystalline samples were ground in a mortar and then put in a low background sample holder for the data collection.

Fig. 3.4 X-ray powders diffractometer used for the characterization of the compounds of this thesis.

References

1. Schubert, U. and N. Hüsing, *Synthesis of Inorganic Materials*. 2005: Wiley.

2. Smart, L.E. and E.A. Moore, *Solid State Chemistry: An Introduction, Third Edition*. 2005: Taylor & Francis.

3. Cheetham, A.K. and P. Day, *Solid State Chemistry: Techniques*. 1988: Clarendon Press.

4. Brinker, C.J. and G.W. Scherer, *Sol-gel Science: The Physics and Chemistry of Sol-gel Processing*. 1990: Academic Press.

5. Zimmerer, G., *Status report on luminescence investigations with synchrotron radiation at HASYLAB*. Nuclear Instruments and Methods in Physics Research Section A: Accelerators, Spectrometers, Detectors and Associated Equipment, 1991. **308**(1–2): p. 178-186.

Chapter 4

Results and Discussion

In the last decade there has been a considerable interest in the investigation of the 5d-4f interconfigurational optical transitions of rare earth (RE) ions in numerous wide band-gap materials due to their potential applications in important technological fields such as scintillating detectors, converting ionizing radiation (X- and γ-rays) to UV and visible light. There is a variety of radiation detector applications that desire scintillators with high light output, good attenuation power and a low level of afterglow, but absolutely require a fast scintillation decay time [1]. This is particularly true for a medical diagnostic imaging technique such as Positron Emission Tomography (PET) where a very high timing resolution is required to suppress random coincidences of incoming γ-rays allowing for high tomographic image quality.

Many of the presently used scintillators are based on materials doped with Ce^{3+} ion which exhibits efficient and relatively fast 5d-4f electric-dipole parity-allowed emission transitions located in the UV and visible spectral regions. The highest figure-of-merit modern Ce^{3+} based scintillators have decay times of 30-70 ns [2]. Recently, parity-allowed 5d-4f emission of Pr^{3+} ion has become of interest due to shorter lifetime that allows development of scintillators with faster time response [3, 4]. The Pr^{3+} 5d-4f emission is shifted by about 1.5 eV towards higher energy with respect to the Ce^{3+} emission in the same host [5]. Appearance of Pr^{3+} 5d-4f emission is subject to sufficiently strong crystal field which shifts the lowest $5d_1$ state of Pr^{3+} below the $^1S_0$ state of the ground $4f^2$ electronic configuration (situated around 210-215 nm).

Our search for novel materials showing fast 5d-4f emission of RE^{3+} ion has led us to the synthesis, characterization and spectroscopic study of new RE^{3+}-activated wide band-gap host lattices including the double phosphates $Ca_9Lu(PO_4)_7:Ce^{3+}$, $Ca_9Lu(PO_4)_7:Pr^{3+}$, $K_3Lu(PO_4)_7:Pr^{3+}$, $KLuP_2O_7:Pr^{3+}$ as bulk powders, the oxyorthosilicates $X1-Y_2SiO_5:Pr^{3+}$ and $X2-Lu_2SiO_5:Pr^{3+}$ as nano-powders and $X2-Y_2SiO_5:Pr^{3+}$ as ultrafine powder and the fluoride $BaMgF_4:Nd^{3+}$ as single crystal.

4.1 $Ca_9Lu(PO_4)_7:Ce^{3+}$ and $Ca_9Lu(PO_4)_7:Pr^{3+}$

4.1.1 Introduction

$Ca_9Lu(PO_4)_7$ (CLuP) compound is characterized by a high effective atomic number (~60.6) that is similar to one for $Lu_3Al_5O_{12}$ and potentially advantageous for gamma-scintillators. This host, belonging to the whitlockite family, has the rhombohedral crystal structure (space group $R3c$, No. 161) with a=10.434 Å and c=37.34 Å, and is isotypic with tricalciumbis phosphate (TCP) β-$Ca_3(PO_4)_2$ with a substitution scheme $(3Ca^{2+}) \rightarrow (2Lu^{3+}+1!)$ [6]. More detailed crystal structure analysis shows that, in principle, there are five possible cation sites (denoted as M_1-M_5 [7]) for the lanthanide dopants in the host due to the similarity between the ionic sizes of the Ca^{2+}, Ce^{3+} and Pr^{3+} ions [8]. In $Ca_9Lu(PO_4)_7$, as Bessière et al. recently reported [9], the Lu^{3+} ion shows a preferential occupation of the octahedral M_5 site (C_3 symmetry) (almost 52% of occupation reported as a percentage of total Lu^{3+} content). This ion occupies also the C_1-symmetric M_1, M_2 and M_3 sites (38%, 13% and 5% of occupation respectively) but not the octahedral C_3 symmetric one (M_4). In addition, the Pr^{3+} ion in $Ca_9Pr(PO_4)_7$ is found to occupy only the three bigger crystal sites with C_1 point symmetry (M_1, M_2 and M_3). In this case, M_3 is the dominant site with an occupation of almost 60% for Pr^{3+} [9]. Finally, in the light of this evidence, we believe that the Pr^{3+} dopant ion in $Ca_9Lu(PO_4)_7$ matrix should go only into M_1-M_3 sites. Reasonably, the occupation ratio of Pr^{3+} and Ce^{3+} for M_1, M_2 and M_3 sites in $Ca_9Lu(PO_4)_7$ can be speculated to be the same occupation ratio of these ions in $Ca_9Pr(PO_4)_7$ and $Ca_9Ce(PO_4)_7$, respectively. These values can be approximately read from the distribution diagram of lanthanide ions in all the possible doped sites (see Fig. 4 of Ref. [10]), and thus are 0.04: 0.18: 0.78 and 0.12: 0.25: 0.63, for Ce^{3+} and Pr^{3+} respectively.

CLuP is expected to be suitably transparent in the UV region, as shown by several double phosphates constituted of lanthanide ions (E_g = 7.3-9.5 eV) [11]. Moreover, it has been demonstrated that this phosphate host is characterized by high chemical and thermal stabilities [12] allowing for its long-time resistance in technological uses.

To the best of our knowledge a very little effort has been made so far on the synthesis and spectroscopic investigation of doped CLuP, although some other neat and doped complex phosphates have been thoroughly investigated [11, 13, 14] and some of them have been shown to be promising for several technological applications as potentially multifunctional materials, particularly phosphors and scintillators. Reports on luminescence properties of CLuP doped with

RE ions are limited by a few papers. Particularly, luminescence of Eu^{3+} doped CLuP was studied in [7]. Ce^{3+}, Mn^{2+} and Eu^{2+}, Mn^{2+} doubly doped CLuP compounds were studied in [15, 16] and found to be promising for application as red and white phosphors, respectively. At the same time, doped CLuP has never been studied in the context of potential scintillator applications. To fill in this gap we found it encouraging to perform a time-resolved spectroscopic study of Ce^{3+} and Pr^{3+} doped CLuP and investigate the efficiency and dynamics of 5d-4f emission as well as host-to-impurity energy transfer mechanisms occurred upon high-energy (VUV) excitation.

4.1.2 Experimental details

Polycrystalline samples of CLuP doped with 1 mol% of Ce^{3+} or 1 mol% of Pr^{3+}, respectively (substituting for Lu^{3+}), were synthesized using a solid state reaction at high temperature (1200°C, 10 h) from $CaCO_3$, $(NH_4)_2HPO_4$ (all reagent grade), Lu_2O_3 (Aldrich, 99.99%), $Ce(NO_3)_3 \cdot 6H_2O$ (Aldrich, 99.99%) and Pr_6O_{11} (Aldrich, 99.999%) following the method described elsewhere [7].

The materials obtained have been characterized by XRD using a Thermo ARL X′TRA powder diffractometer, operating in the Bragg-Brentano geometry and equipped with a Cu-anode X-ray source ($K_α$, $λ$ = 1.5418 Å). Time resolved VUV luminescence spectra have been measured using synchrotron radiation at the SUPERLUMI station of HASYLAB (DESY, Germany), described in more detail in section 3.2.1. The experimental results presented in this work were obtained in two different time periods when the storage ring was operated in different bunch modes that was out of our choice. Particularly, the spectrum presented by curve 3 in figure 2, all spectra shown in figure 5, decay curve recorded upon excitation at E_{exc} = 4.28 eV and the decay curve shown in figure 4 were taken at reduced (2) bunch mode. All other data were recorded at normal (5) bunch mode. A full time range available between two sequential SR pulses was about 480 ns and 192 ns for the reduced and normal bunch modes, respectively.

4.1.3 Structural characterization

The structural characterization of the synthesized samples was performed by X-ray powder diffraction (XRPD). All the diffraction peaks in the XRD patterns of Pr^{3+} and Ce^{3+}-doped CLuP samples are compatible with ICDD data on CLuP (PDF Card No. 04-001-9672) (Fig. 4.1).

No other phases are detected, indicating that the samples synthesized are single phases. In addition, we observed a small expansion of the cell volume as a consequence of doping with Ce^{3+} or Pr^{3+}. In fact, the cell parameters of the Pr^{3+} doped sample and the undoped one are

$a=b=10.442(1)$ Å, $c=37.378(3)$ Å and $a=b=10.434$ Å, $c=37.34$ Å (PDF Card No. 04-001-9672), respectively. As a consequence, the cell volume of the doped sample [3529.40(7) Å^3] is slightly larger than for the undoped one (3520.52 Å^3). The same effect was observed in the case of the sample doped with Ce^{3+}, which was characterized by the cell parameters $a=b=10.448(1)$ Å, $c=37.379(3)$ Å and volume of 3533.56(5) Å^3.
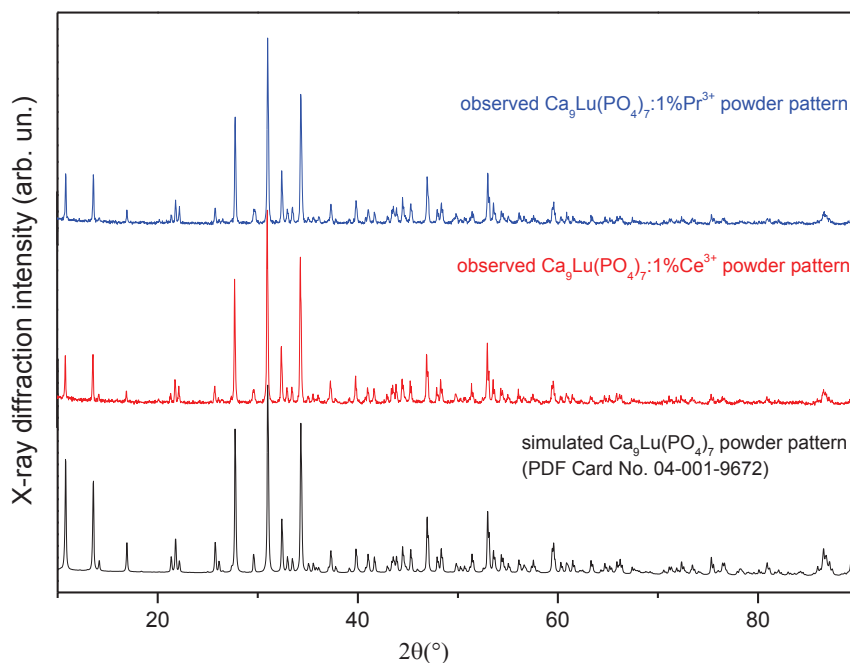

Fig. 4.1 X-ray powder patterns of the CLuP: 1%Ce^{3+}, CLuP: 1%Pr^{3+} and simulated CLuP

4.1.4 VUV Luminescence spectroscopy of CLuP:Ce^{3+}

The time-integrated emission spectrum of Ce^{3+} in CLuP obtained at 300 K upon direct VUV excitation into the Ce^{3+} 5d levels at $E_{exc}= 4.96$ eV (see below) is presented in figure 4.2, curve 1. The intense and broad emission band extending from 2.95 to 4.00 eV and centered at about 3.49 eV is assigned to the interconfigurational radiative transitions from the lowest 5d energy level of Ce^{3+} to the states of the ground 4f^1 electronic configuration (4f^{0}5d$^1\rightarrow$4f^1). This observation is in good agreement with results presented in [15]. Generally the Ce^{3+} spectra demonstrate a doublet emission band due to the spin-orbit splitting of the ground state into $^2F_{5/2}$ and $^2F_{7/2}$ levels. At room temperature (RT) the double structure is mostly washed out because of thermal broadening. However, in the time-integrated emission spectrum recorded at nearly liquid He temperature (figure 4.2, curve 3) the doublet band becomes resolved and exhibits two maxima centered at 3.41

eV and 3.64 eV. The separation of about 0.23 eV between these maxima is in agreement with the typically observed spin-orbit splitting between $^2F_{5/2}$ and $^2F_{7/2}$ states of Ce^{3+} ions. The RT time-integrated emission spectrum recorded upon excitation at 8.55 eV that corresponds to transitions above the band-gap (figure 4.2, curve 2) shows a profile very similar to that observed upon direct intra-centre excitation indicating an existence of energy transfer from host to impurity.
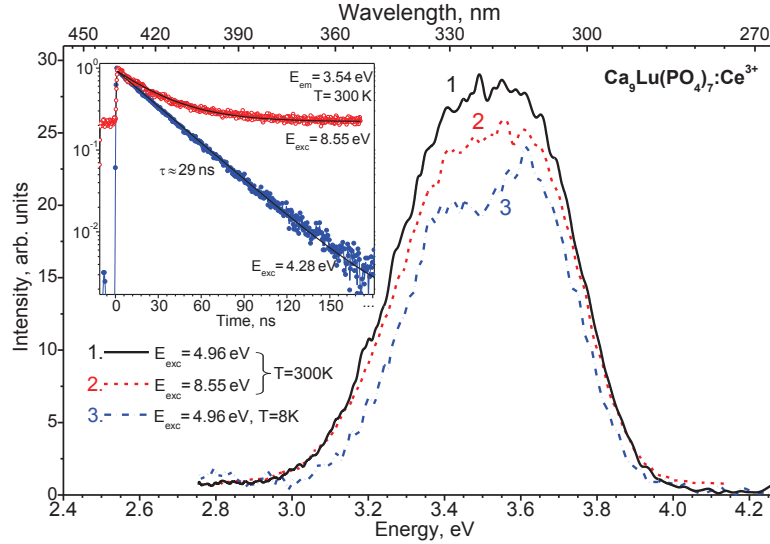

Fig. 4.2 Time-integrated emission spectra of CLuP:Ce^{3+}. Inset shows decay curves recorded monitoring Ce^{3+} emission at 3.54 eV upon intra-center (1, 3) and host excitation (2) at T=300K (1, 2) and T = 8K (3).

With the aim of understanding the 5d energy level structure of Ce^{3+} in CLuP and the processes responsible for the host-to-impurity energy transfer we studied time-resolved UV-VUV excitation spectra for Ce^{3+} 5d-4f emission. When the Ce^{3+} ion is embedded in a crystalline host, the mean energy of the 5d configuration is shifted downwards relative to the free ion value and the 5d levels split into at most five different crystal field components.

Figure 4.3 shows time-integrated and time-resolved excitation spectra of CLuP:Ce^{3+} recorded at 300 K monitoring emission at 3.54 eV. The UV part of the time-integrated excitation spectrum is characterized by a broad structured band with well pronounced maxima at 3.95, 4.26, 4.68, 5.02 and 5.59 eV. As it is seen from the time-resolved spectra, the band is dominated by a fast decaying emission signal. We assign this structured band to transitions from the ground $4f^1$ state of the Ce^{3+} ions to the five crystal field levels of 5d state. A weak feature located at about 6.14 eV (labeled with an asterisk) dominates in the fast time gated spectrum that suggests its possible intra-center origination. It may be tentatively assumed that this feature is connected with population of the 6s state of Ce^{3+}.
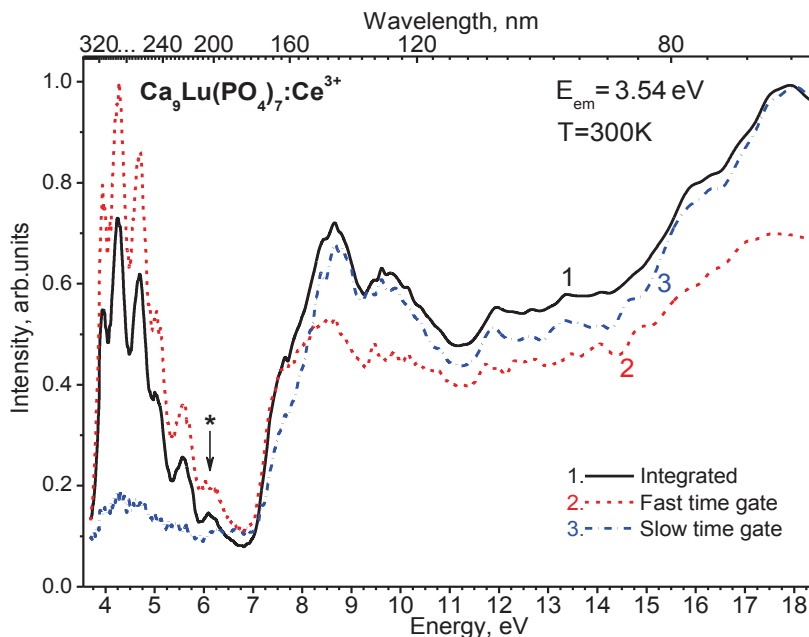
Fig. 4.3. Time-resolved and time-integrated excitation spectra of CLuP:Ce^{3+} recorded monitoring Ce^{3+} 5d-4f emission at 3.54 eV.

The VUV part of the CLuP:Ce^{3+} time-integrated excitation spectrum appears as an intense complex structure with low-energy onset at about 7.1 eV. The onset is quite sharp in the range of about 7.1 – 7.6 eV and becomes rather moderate at higher energy following by a well pronounced maximum at about 8.65 eV. The time-resolved spectra demonstrate a somewhat different behaviour around the onset. Particularly, the fast time gated spectrum reveals a faster rise in the range of 7.1 – 7.3 eV compared to the slow time gated one. At higher energy the signal detected within slow time gate dominates and determines the shape of the time-integrated spectrum. An intense maximum in the time-integrated spectrum is observed near 8.65 eV. The behaviour shown by the excitation spectra suggest that onset at 7.1 eV represents the beginning of fundamental optical absorption of the host. The interplay between fast and slow time gated excitation spectra around the fundamental absorption edge is quite typical for complex oxides with low symmetry of the oxygen ion and results from a multiplet character and lack of uniformity of the valence band [17]. Although it is not straightforward to determine the band gap of CLuP from our experimental data, we may suppose that transitions to conduction band begin in the energy range of about 7.8 - 8.5 eV that is consistent with band gap values of other phosphates such as REPO$_4$ and A$_3$RE(PO$_4$)$_2$-type (RE - rare earth, A-alkali metal ions) [11]. Above 9 eV and up to about 15 eV the time-integrated and time-resolved spectra generally demonstrate a similar structure and moderate variation of intensity. The rise of intensity occurring above 15 eV may be caused by the development of multiplication of electronic excitations when each excitation photon creates more than one electron-hole pair [18].

The inset in figure 4.2 displays the decay curves for the Ce^{3+} emission monitored at 3.54 eV at RT upon intra-center and host excitation at 4.28 and 8.55 eV, respectively. The decay curve corresponding to intra-center excitation is well fitted with a single-exponential function with lifetime τ of about 29 ns. The decay curve recorded upon host excitation shows a significant contribution of a slow decay component (probably of micro- or millisecond lifetime) presented as a piling-up. Meanwhile, the main decay component of the host excited emission is found to be characterized by a lifetime equal to the one obtained for the direct intra-center excitation. The slow decay component in the host excited Ce^{3+} emission shows the existence of delays in energy transfer processes which may occur due to retrapping of electronic excitations by defects. No build-up of the luminescence at very short time after the SR excitation pulse is observed neither upon intra-center nor host excitation indicating that the population of the Ce^{3+} 5d emitting level occurs in less than 1 ns and the excited state does not experience any thermally assisted depopulation. It is worth noting that the lifetime of the Ce^{3+} emission measured upon direct 4f-5d excitation remains nearly the same when sample is cooled down to 8 K suggesting no thermal quenching for the 5d-4f emission within the temperature range 8 – 300 K.

4.1.5 VUV Luminescence spectroscopy of CLuP:Pr^{3+}

Figure 4.4 shows time-resolved and time-integrated emission spectra of CLuP doped with 1% Pr^{3+} obtained at 300 K upon Pr^{3+} $4f^2 \rightarrow 4f^1 5d^1$ excitation at 6.20 eV. The time-integrated mode emission spectrum is dominated by a broad band with two prominent maxima at about 4.44 and 5.06 eV. These emission features are well pronounced in the fast time gated spectrum and are identified as the parity-allowed interconfigurational optical transitions from the lowest excited Pr^{3+} $4f^1 5d^1$ state to the ^3H_J and ^3F_J multiplets of the ground $4f^2$ electronic configuration ($4f^1 5d^1 \rightarrow 4f^2$). The weak broad band centered around 2.82 eV and dominating within the slow time gated spectrum is probably due to a defect related emission. Additionally, a very weak emission peak at 2.04 eV present in the slow time gated spectrum is assigned to intraconfigurational Pr^{3+} $4f^2 \rightarrow 4f^2$ transition from the $^1D_2$ level to the ground state $^3H_6$. It is interesting to point out an absence of $^3P_0$ emission that is likely to be quenched by multiphonon relaxation (MPR) to $^1D_2$ multiplet, as observed in the case of the phosphates $LaPO_4$ and $LiLaP_4O_{12}$ at similar dopant concentrations [19, 20]. The MPR process can be very efficient because of the high phonon frequency of the host lattice; the typical maximum phonon frequency of the P-O stretching vibration of the PO_4^{3-} molecular group is in the range of 1200-1400 cm^{-1} [21].
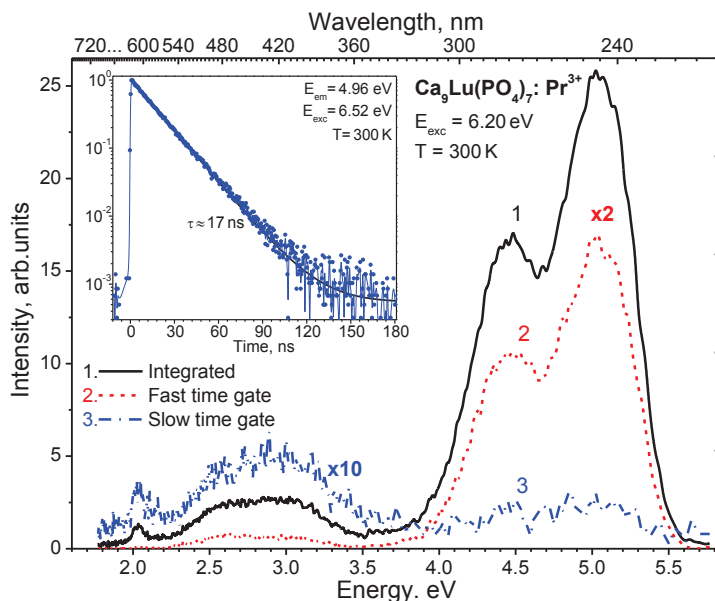
Fig. 4.4 Time-integrated and time-resolved emission spectra of CLuP:Pr^{3+} recorded at T = 300K upon excitation at 6.20 eV. Inset shows decay curves recorded monitoring Pr^{3+} emission at 4.96 eV.

Increasing the excitation energy to 8.27 eV, that corresponds to the intrinsic absorption of the host lattice, leads to significant transformation of the emission spectra (figure 4.5) due to the appearance of a broad emission band centered at 3.86 eV. The band clearly dominates in the slow TW spectrum and demostrates a little departure from Gaussian shape at its low-energy side that may be due to contribution of the 2.82 eV emission band. The band is tentatively assigned to a defect emission. We should note that the intra-center and host excited emission spectra revealed no obvious difference when recorded at RT and near He liquid temperature (not shown).
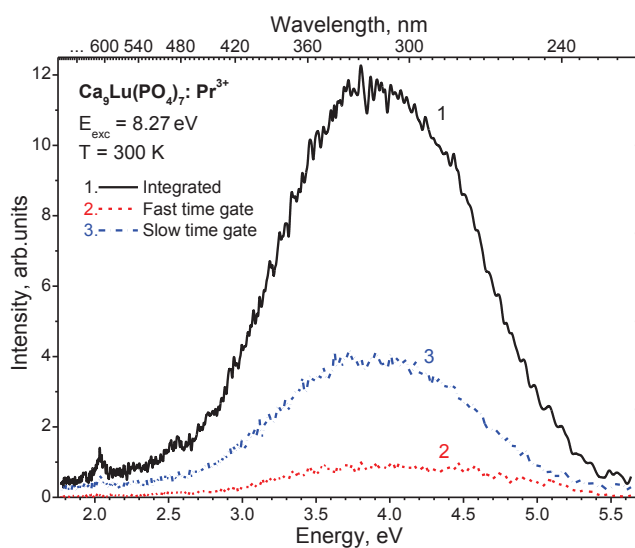

Fig. 4.5 Time-integrated and time-resolved emission spectra of CLuP:Pr^{3+} recorded at T = 300K.

The decay curve of the of Pr^{3+} 5d-4f emission monitored at 4.96 eV and excited at 6.25 eV at RT is shown in the inset of figure 4.4. The time profile demonstrates a single exponential behaviour with approximate lifetime $\tau \approx 17$ ns that agrees well with Pr^{3+} 5d-4f emission lifetime observed in other phosphates (17 ns in YPO_4 [22], 16-17 ns in $Sr_3La(PO_4)_3$ and $Ba_3Lu(PO_4)_3$ [14]). The lifetime was found to remain nearly the same when sample is cooled down to 8 K. No build-up was observed either at RT or at T=8K. The lifetime of the Pr^{3+} 5d-4f emission is a factor 1.7 faster than observed for Ce^{3+} that is in line with the higher energy of Pr^{3+} emission as compared to Ce^{3+} (see above). Theoretically, the radiative lifetime of an excited center is proportional to λ_{em}^2 or λ_{em}^3 [23] that means a factor of 2-3 is to be expected in our case.

Figure 4.6 shows the RT time-integrated and fast time gated excitation spectra recorded monitoring the Pr^{3+} 5d-4f emission at 4.81 eV and RT time-integrated excitation spectrum recorded monitoring the defect related emission at 2.82 eV. Excitation spectrum of Pr^{3+} 5d-4f emission taken within slow time gate did not reveal any remarkable features and appeared to be very weak (not shown). A strong structured excitation feature spread from about 5.3 to 7.5 eV and composed of few local maxima dominates in the fast time gated spectrum. We assign this feature to superposition of excitation bands corresponding to population of $4f^15d^1$ states. As long as a maximum corresponding to the lowest energetic 4f-5d transition is not well pronounced we found it useful to compare excitation spectra of $CLuP:Pr^{3+}$ and $CLuP:Ce^{3+}$ around the energy range of 4f-5d transitions. It is well established that the spectral positions of the main 4f-5d excitation bands of Pr^{3+} can be predicted by simply blue shifting of the excitation spectrum observed for Ce^{3+} by about 1.51 ± 0.09 eV (12240 ± 750 cm^{-1}) [5]. We found a good correlation to be observed when shift of 1.57 eV is applied (see confronted Ce^{3+} and Pr^{3+} excitation spectra in the inset of figure 4.6). Basing on this comparison we assign the low-energy shoulder of this band centered at 5.49 eV to the 4f-5d excitation transition occurred from $^3H_4$ ground state to the lowest energetic $5d_1$ level of Pr^{3+}. The higher energetic maxima at 5.80, 6.20, 6.60 and 7.12 eV are likely to represent $5d_2$, $5d_3$, $5d_4$ and $5d_5$ crystal field states, respectively.

The Stokes shift of the Pr^{3+} emission, calculated as energy difference between the maxima of the lowest energy Pr^{3+} $4f^2 \rightarrow 4f^15d^1$ excitation band and the highest energy Pr^{3+} $4f^15d^1 \rightarrow 4f^2$ emission band is about 0.384 eV (3100 cm^{-1}). According to the model recently proposed by Srivastava et al. [24], the Stokes shift of the Pr^{3+} emission should be lower than ≈ 3200 cm^{-1} to give rise to domination of radiative $4f^15d^1 \rightarrow 4f^2$ transitions in the relaxation of Pr^{3+} $4f^15d^1$ excited state over 4f-4f transitions. A weak feature in time-integrated and fast-time gated excitation spectrum of Pr^{3+} 5d-4f emission is observed as a sideband around 7.4 – 9 eV. This is completely different from what is observed in excitation spectra of Ce^{3+} (see figure 4.3) in the same energy range which corresponds to beginning of the host fundamental absorption.
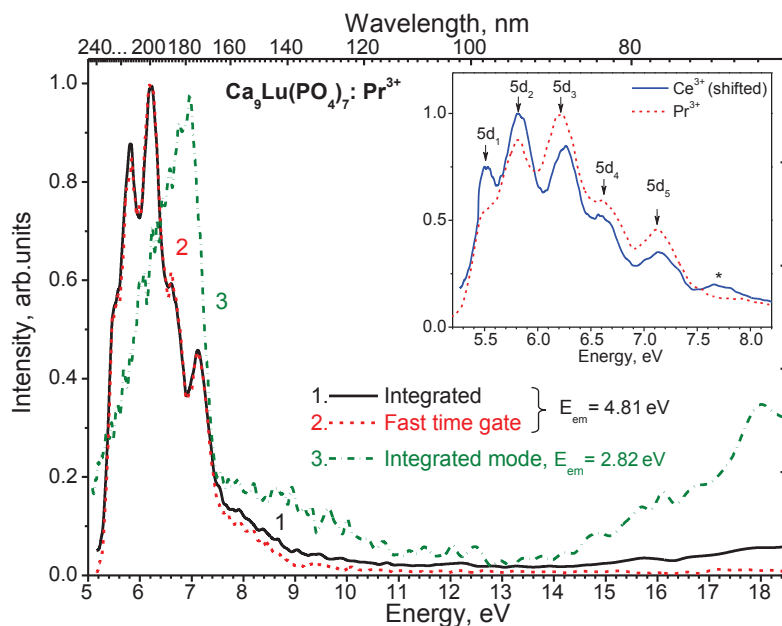
Fig. 4.6 Excitation spectra of CLuP:Pr^{3+} recorded at T = 300K monitoring Pr^{3+} 5d-4f emission at 4.81 eV in integrated mode (1) and within fast time gate (2) and excitation spectrum of the defect-related emission at 2.82 eV in integrated mode (3). The Inset shows confronted excitation spectra of CLuP:Pr^{3+} and CLuP:Ce^{3+} shifted by 1.57 eV towards higher energy.

Above 9 eV no significant excitation features are observed. The absence of 5d-4f emission upon excitation over the bandgap is due to the inefficient energy transfer from intrinsic electronic excitations to the 4f^{1}5d^1 levels of Pr^{3+} indicating that the host→Pr^{3+} energy transfer is far from being the only way to release the energy absorbed by host. The time-integrated excitation spectrum of the intrinsic defect emission (E$_{em}$ = 2.82 eV) recorded at 300 K shows a broad complex band in the range of 5.07 - 7.5 eV (figure 4.6). A weak structure is also observed in the range of 7.5 – 11 eV that represents excitation (creation) of defects via host absorption. Increase of emission intensity upon excitation above 14 eV cannot be unambiguously interpreted at this stage without additional study. It can either occur due to correction procedure performed on a low intensity spectrum or could be connected with the manifestation of multiplication of photons [18] that is expected to be observed in this energy range.

The analysis of the experimental data obtained for Ce^{3+} and Pr^{3+} doped CLuP suggests the existence of a factor limiting the efficiency of the host-to-impurity energy transfer; this factor appears to be strongly pronounced for Pr^{3+} doped sample and negligible for Ce^{3+} doped one. Indeed, excitation and emission spectra obtained for CLuP:Pr^{3+} demonstrate strong broad features related to the defect absorption. At the same time, no defect emission is observed for the CLuP:Ce^{3+}. To explain these phenomena we propose the following model.

First of all, it should be noted that the energies of the 4f-5d transitions and the absorption of the defect states are very close; this results in the development of complex competitive relaxation channels for the excited states. Analysis of the emission and excitation spectra of CLuP:Pr^{3+} suggests the existence of multiple structure of the excited states of the defects, which experience significant Stokes shift. The absorption of the defects competes with 4f-5d transitions of Pr^{3+}. At the same time the emission of the defects may be transferred to Ce^{3+}. By taking into account that the defect states actively trap the host electronic excitations we suppose that in case of CLuP:Ce^{3+}, the defect excited states relax non-radiatively to some of the Ce^{3+} 5d states causing an important fraction of the energy to be dissipated in the host. At the same time no emission from the defect states is observed for CLuP:Ce^{3+} as they are not the lowest energy ones. The 4f-5d emission of Ce^{3+} demonstrates significant contribution of slow decay component (see inset in figure 4.2) that reflects the dynamics of defect-to-Ce^{3+} ions feeding process. In the case of CLuP:Pr^{3+}, the $4f^1 5d^1$ states are shifted up towards higher energy for about 1.57 eV. In this case the defect excited states are likely to relax without transferring the energy to the Pr^{3+} $4f^1 5d^1$ states and this process acts as a dominating relaxation channel for the host electronic excitations. Finally, as long as the defect states appear below $4f^1 5d^1$ states, the defect emission occurs (see figures 4.5 and 4.6).

We believe that the nature of defects present in CLuP is at least partially to be attributed to the disordered nature of the host. Similar spectroscopic manifestation of the disordered originated defects was observed by some of us in [14]. Obviously, the above suggested model may be further improved. To this end it may be useful to perform a more detailed temperature-dependent spectroscopic study for RE doped and undoped CLuP. Besides, study of thermoluminescence effects may be required to get more insight into the nature and energy structure of defects.

4.1.6 Conclusions

Ce^{3+} and Pr^{3+}-activated CLuP samples have been synthesized by solid-state reaction. The time-resolved VUV spectroscopic investigation of the luminescence properties of CLuP:Ce^{3+} and CLuP:Pr^{3+} was performed for the first time applying synchrotron radiation. Particularly, the 5d energy levels of Ce^{3+} and Pr^{3+} ions, host absorption and host→Ce^{3+}/Pr^{3+} energy transfer processes were investigated.

Fast 5d-4f emission has been observed from both samples upon direct intra-centre VUV excitation but only in the case of CLuP:Ce^{3+} sample efficient host-to-impurity energy transfer has been revealed. Presumably, as shown by some of us for other double phosphates [14], the disordered nature of the host induces the presence of defects which actively trap the host electronic

excitations. As long as 5d states of Ce^{3+} are energetically situated below the defect excited states, they experience an efficient non-radiative feeding from defects. In case of Pr^{3+} doped CLuP, no efficient host→Pr^{3+} energy transfer is observed due to the fact that the defect emission occurs at lower energies than the 4f-5d excitation.

The decay kinetics of the 5d-4f emission upon VUV intra-centre excitation is characterized by a lifetime of 29 ns for Ce^{3+} and 17 ns for Pr^{3+}. The lifetime has been found to be nearly temperature independent within the range 8-300 K for both Ce^{3+} and Pr^{3+} doped compounds. Although the Ce^{3+} doped CLuP demonstrates intense 5d-4f luminescence upon host excitation its decay dynamics is significantly contributed by the slower decaying component of micro- or millisecond lifetime. The latter fact is obviously unwanted for the scintillator materials.

To get more benefits from CLuP as a potential host for scintillator application it may be challenging to study double codoped CLuP:Tb^{3+},Ce^{3+}. Existence of Tb^{3+} ions may provide an additional effective channel for capturing of the host electronic excitation and is expected to provide faster energy transfer to Ce^{3+} ions (Tb^{3+}→ Ce^{3+}) in comparison with competitive defect-to-Ce^{3+} channel.

4.2 $K_3Lu(PO_4)_2$:Pr^{3+}

4.2.1 Introduction

The $K_3Lu(PO_4)_2$ (KLuP) is characterized by a high effective atomic number of ~44.5, that is higher than one for $Y_3Al_5O_{12}$ (29.5) or $YAlO_3$ (31.4) widely used as scintillator materials, and potentially advantageous for X- and γ-ray detection. This host crystallizes with a trigonal unit cell, space group P-3, density 3.9 g/cm^3 at RT. In this case, the lutetium ion is six-coordinated by the oxygen atoms of the phosphate groups with two non-equivalent sites in the lattice. For this host material two phase transition are known to occur at lower temperature [25]. The first transition occurs at ~250 K and a monoclinic phase ($P2_1$/m space group) is obtained. The Lu ion retains the six-fold coordination but it occupies only one crystal site. The second phase transition occurring at ~140 K leads to a crystal structure with the same monoclinic space group but coordination of the Lu ion changes to a 7-fold one.

The absorption edge of KLuP is expected to be localized at rather high energy as shown by several double phosphates constituted of lanthanide ions (E_g = 7.3-9.5 eV) [11, 25] making this compound suitable as efficient host for various optical applications including fast scintillators and vacuum ultraviolet phosphors. To the best of our knowledge, the time-resolved spectroscopy and excited state dynamics of Pr^{3+} ion in KLuP upon VUV excitation with synchrotron radiation has not been reported in literature so far although the Pr^{3+} 5d-4f emission in KLuP:Pr^{3+} powders has been demonstrated in a recent paper [24]. It is also worth to mention that some scintillating and luminescent properties of Ce^{3+} in KLuP single crystals as well as in other double phosphate of $A_3Lu(PO_4)_2$-type (A = Li, Rb, Cs) have been thoroughly studied elsewhere [25-27]. Meanwhile some RT VUV spectroscopic properties of Pr^{3+}-doped $ALuP_2O_7$-type alkali lutetium diphosphates (A = Na, K, Rb, Cs), that are other compounds in the same Lu_2O_3-A_2O-P_2O_5 system, have been investigated in [28] to demonstrate an efficient host-to-Pr^{3+} energy transfer.

In this contribution the synthetic procedure and structural characterization of KLuP doped with Pr^{3+} ion are described in detail. Time-resolved emission and excitation spectra as well as luminescence decay curves at different temperatures measured upon selective excitation with synchrotron radiation (SR) in the UV-VUV region are presented and analyzed. The prospective applications of this luminescent material are discussed.

4.2.2 Experimental details

Polycrystalline sample of KLuP doped with 1 mol% of Pr^{3+} (substituting for Lu^{3+}) were synthesized using a solid state reaction from K_2CO_3, $(NH_4)_2HPO_4$ (all reagent grade), Lu_2O_3 (Aldrich, 99.99%) and Pr_6O_{11} (Aldrich, 99.999%). Appropriate amounts of the reagents were mixed and heat treated in a horizontal furnace in air for 4 hours at 600 °C and 1 hour at 950 °C with intermediate regrinding. In between investigations the samples were stored at RT in dark and dry conditions.

X-ray powder diffraction patterns (XRPD) were measured with a Thermo ARL X′TRA powder diffractometer, operating in the Bragg-Brentano geometry and equipped with a Cu-anode X-ray source (K_α, $\lambda = 1.5418$ Å). Preliminary synchrotron X-ray diffraction powder patterns of an undoped KLuP sample at RT and 220 K were collected in transmission geometry at the MCX beamline located at the multidisciplinary Synchrotron Light Laboratory (ELETTRA) in Trieste (Italy).

Differential scanning calorimetry (DSC) experiments were performed to follow the phase behaviour of the sample under investigation using a Q1000, TA Instruments at a heating rate of 10°C/min. The samples were sealed in aluminum DSC pan for the measurement.

Time-resolved VUV spectroscopic measurements were carried out using the SUPERLUMI facility at HASYLAB of DESY (Hamburg, Germany), described in more detail in section 3.2.1. The time-resolved spectra were recorded within two time gates (TGs): 2-11 ns (fast time gate) and 50-61 ns (slow time gate) relative to the beginning of the SR pulse. The time-integrated spectra were recorded counting the emission signal within the whole time period of 96 ns available between SR pulses at a 10 bunch mode (BM) of the storage ring.

4.2.3 Structural characterization

The structural characterization at RT of the synthesized Pr^{3+} doped sample was performed by means of X-ray powder diffraction (XRPD). All the diffraction peaks in the XRPD pattern of Pr^{3+}-doped KLuP sample are compatible with ICDD data of the trigonal (*P*-3 space group) KLuP (PDF Card No. 01-085-1586) (Fig. 4.7). No other phases are detected indicating that the sample synthesized is a single phase. In addition, we observed a small expansion of the cell volume as a consequence of substitution of Lu^{3+} ion (ionic radius 0.861 Å, in six-fold coordination [8]) with the larger Pr^{3+} one (0.99 Å, in six-fold coordination [8]). The cell volume of the Pr^{3+} doped sample and the undoped one are 617.07(1) $Å^3$ and 616.66(1) $Å^3$, respectively.
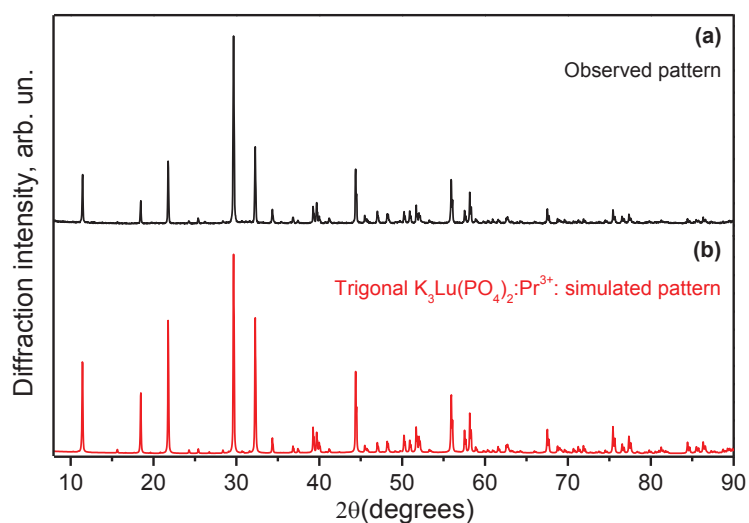
Fig. 4.7 Experimental XRPD pattern of the KLuP:1%Pr^{3+} powder at 300K (a) and simulated XRPD pattern of the trigonal KLuP (b).

A supplementary structural characterisation has been performed by means of the Rietveld refinement on the synchrotron X-ray powder diffraction pattern. The corresponding results will form the groundwork of a future paper. For the present work an important issue worthy to be mentioned is that, on average, the Lu-O bond lengths in the case of trigonal phase are Lu(1)-O = 2.16(1) Å and Lu(2)-O = 2.14(1) Å, whereas in the case of the monoclinic phase, stable in the temperature range 140-250 K, the average Lu-O bond length for the only available Lu^{3+} crystal site seems to be longer than in the case of the trigonal one. The Rietveld refinement on the powder pattern of the low-temperature monoclinic phase is only preliminary.

The differential scanning calorimetry (DSC) of KLuP:Pr^{3+} sample is shown in Fig. 4.8.
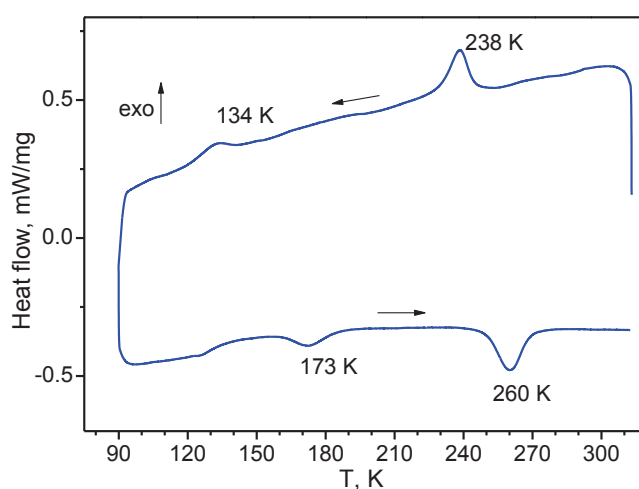

Fig. 4.8 DSC scan profile of CLuP:Pr^{3+} powders. Both up- and down-T scan rate are 10 K/min.

The DSC scan decreasing the temperature shows distinct exothermic peaks at approximately $T_1 = 238$ K and $T_2 = 134$ K associated with the two phase transitions documented in [25]. These crystal structural transformations appears to be fully reversible even though the scan increasing the temperature evidences a slight hysteresis for both transitions ($T_1 = 260$ K and $T_2 = 173$ K).

4.2.4 Luminescence spectroscopy and dynamics

Fig. 4.9 gathers the RT time-resolved and time-integrated emission spectra of KLuP:Pr^{3+} recorded upon direct intra-centre and host excitation respectively. The RT spectra of KLuP:Pr^{3+} obtained upon direct intra-centre excitation at 190 nm (Fig. 4.9-a) are dominated by a broad band extending from 225 and 375 nm and centered at about 275 nm. This band is well pronounced in the fast TG spectrum and it is assigned to the parity-allowed interconfigurational transitions from the lowest excited 5d state to the states of the ground 4f^2 electronic configuration of Pr^{3+} ion (4f^{1}5d^1→4f^2). The tail observed on the long wavelength side of the emission indicates the presence of another emission overlapping with the dominant Pr^{3+} emission, consistent with the availability of two distinct crystallographic sites for Pr^{3+} in the RT trigonal KLuP phase [25].
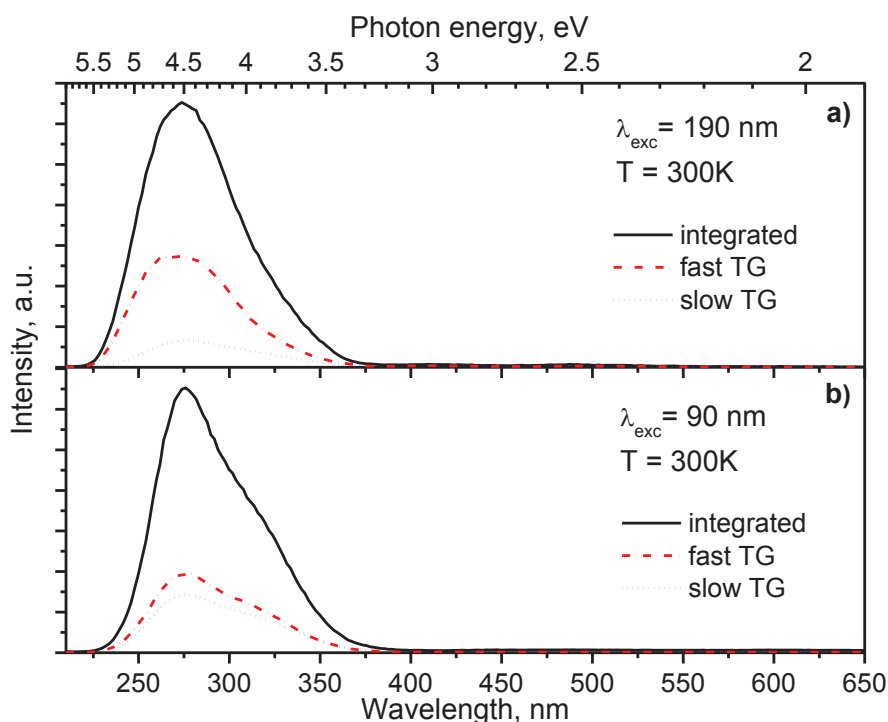

Fig. 4.9 Time-integrated and time-resolved emission spectra of KLuP:Pr^{3+} powders recorded upon selective excitation at 190 nm (a) and 90 nm (b) at 300K.

Fig. 4.9-b presents the RT time-integrated and time-resolved spectra recorded upon excitation at 90 nm; this corresponds to transitions far above the band-gap (E_g). A typical bandgap energy for many double phosphates is about 7.3-9.5 eV (170-130 nm) as suggested in [11] by the analysis of VUV reflection spectra. The time-integrated spectrum is similar to that observed upon direct intra-centre excitation showing a broad band extending from 225 and 380 nm, most relevant in the fast TG spectrum. A shoulder pronounced at about 325 nm reflects the presence of the two different Pr^{3+} emitting sites which are integrally excited under bandgap excitation. At the same time, the nearly twofold increase of the signal intensity detected within slow TG around the features related to the Pr^{3+} 5d-4f transitions indicates the existence of some delayed host-to-impurity energy transfer processes. Furthermore, it is worth noting that for both direct and host excitations no emission features associated with the 4f-4f transitions from the $^3P_0$ and $^1D_2$ levels are observed. This can be explained on the basis of the Stokes shift (see below).

Fig. 4.10 collects the time-integrated emission spectra of KLuP:Pr^{3+} recorded at 8, 190 and 300 K upon intra-centre excitation at 190 nm. Interestingly, the position and the profile of the Pr^{3+} 5d-4f emission band become significantly different with increasing temperature from 8 to 300 K, in agreement with what was observed for KLuP:Ce^{3+} single crystals in [25].

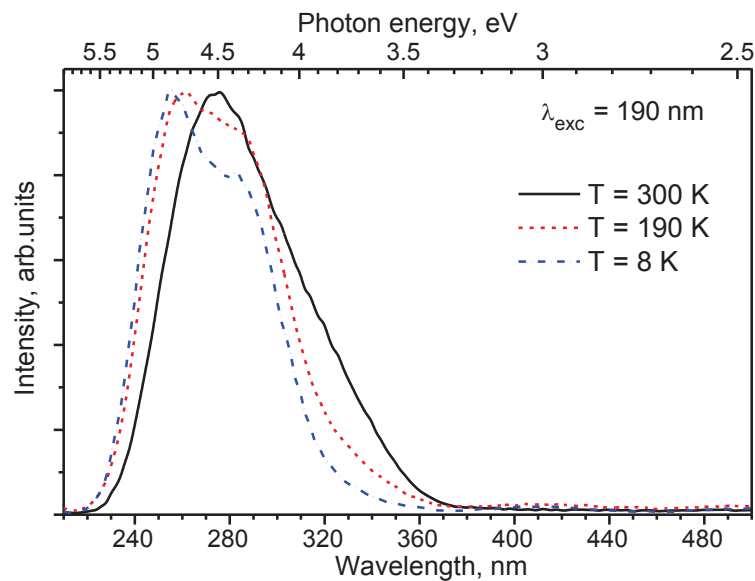**Figure 4.10** Time-integrate emission spectra of KLuP:Pr^{3+} powders recorded upon intra-centre excitation at 190 nm at 8, 190 and 300K.

Since in KLuP the dopant ions substitute only for the Lu^{3+} ions, the above-mentioned changes have to be linked with the crystal structure transformations of KLuP and consequently with the local lutetium coordination and symmetry changes. As matter of the fact, the energy of the

$4f^1 5d^1 \rightarrow 4f^2$ emission band strongly depends on both the covalence effect and the crystal field strength induced by the ligands. As a result of covalent bonding between the 5d and the ligand orbitals, the 5d orbitals expand by partial delocalization over the ligands and consequently the energy is lowered (nephelauxetic effect). The red shift of the Pr^{3+} 5d-4f emission band observed with increasing temperature from 8 to 300 K is linked to a possible increase of the covalency of the Lu–O bonds moving from the monoclinic low temperature phase to the trigonal RT one. This hypothesis correlates with preliminary results of our structural study of synchrotron X-ray powder diffraction suggesting a decrease of the Lu-O bond length when crystal structure changes from the monoclinic to trigonal (see above).

Fig. 4.11 shows time-integrated and time-resolved excitation spectra of KLuP:Pr^{3+} recorded monitoring emission at 320 nm for RT and at 280 nm for T = 8 K. The UV part of the time-integrated excitation spectrum recorded at RT (Fig. 4.11-a) is characterized by a broad structured band consisting of maxima at about 231, 222 nm and low intensity features spread from about 170 to 210 nm. As can be seen from the time-resolved spectra, the UV band is dominated by a fast decaying emission signal. We assign this structured band to transitions from the ground $4f^2$ state to the various 5d crystal field levels of Pr^{3+} ion (in the two possible Lu sites of the RT trigonal KLuP phase).
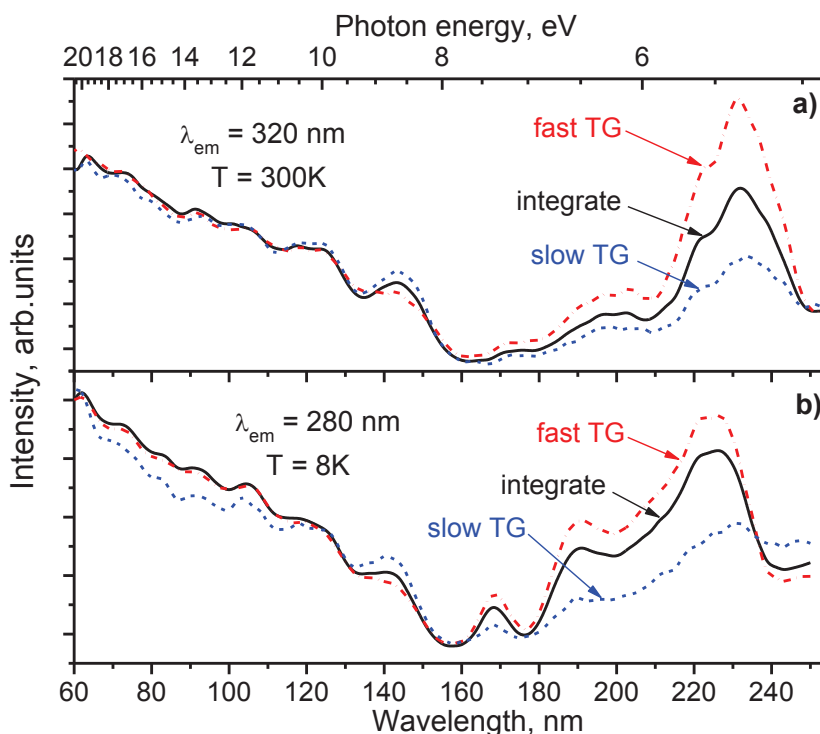

Fig. 4.11 Time-integrated and time-resolved excitation spectra monitoring 5d-4f emission of Pr^{3+} in KLuP:Pr^{3+} powders at T=300K (a) and T=8K (b).

On the base of data on 4f-5d transition energy for the Ce^{3+} ion in KLuP at RT [25] and known energy shift of ~12240 cm^{-1} between 5d states of Ce^{3+} and Pr^{3+} [5] the first Pr^{3+} 4f-5d transition can be expected at 235 nm, which is in good agreement with the data presented in Fig. 4. The Stokes shift for the RT Pr^{3+} 5d-4f transitions was estimated after suitable deconvolution of the band profiles and resulted to be about 2800 cm^{-1}. This is in agreement with the model for Pr^{3+} emission proposed by Srivastava et *al.* [24] which suggests that 5d-4f transitions dominate over 4f-4f ones when the Stokes shift is lower than ~3200 cm^{-1}

At near liquid He temperature the excitation spectra (Fig. 4.11-b) demonstrate significant change in the spectral range above 160 nm compared to the RT ones reflecting the above-mentioned crystallographic structural phase transformation of KLuP and nephelauxetic effect. The lowest energy 4f-5d excitation maximum is observed at about 225 nm being blue-shifted relative to that at RT by about 1100 cm^{-1}. Well pronounced maxima related to higher-energy 4f-5d transitions are observed at about 191 and 168 nm.

Excitation processes related to energy transfer from the host electronic excitations are observed in the excitation spectra below ~160 nm and ~157 nm for RT and T = 8 K, respectively. This correlates with the bandgap energies reported for similar double phosphates in Ref. [11]. We note that the excitation spectra do not demonstrate any sharp rising excitation feature at the beginning of fundamental observation that indicate lack of the excitonic energy transfer mechanism. At the same time, a gradual rise of excitation spectra towards shorter wavelength suggests that host-to-Pr^{3+} energy transfer is dominated by the recombination mechanism. One of the reasons for domination of recombination mechanism may be connected with low energy of relaxed excitons that is insufficient for reabsorption by Pr^{3+} 5d states. We did not observe an exciton emission from our Pr^{3+} doped samples that is probably due to the fact that intrinsic electronic excitations are mostly captured by Pr^{3+} ions. At the same time, we were unable to find any published reports on exciton emission in KLuP. Nevertheless, by analogy with energy of self-trapped exciton emission in other phosphates (~23800 cm^{-1} in YPO_4 [29], ~22600 cm^{-1} in $LiY(PO_4)_3$ [30]) we suppose that in case of KLuP it is very probably located at energy much lower than that required for 4f-5d absorption of Pr^{3+} in this material (> 43000 cm^{-1}).

The temperature dependent decay curves of the Pr^{3+} 5d-4f emission upon both intra-centre and bandgap excitations are presented in Figures 4.12-a and 4.12-b, respectively. Based on the emission spectra recorded at different temperatures, we performed the decay measurements at spectral points best corresponding to Pr^{3+} 5d-4f emission in the particular phases: at λ_{em} = 320 nm for Pr^{3+} emission in the trigonal RT phase for T = 300 and 240 K, and at λ_{em} = 280 nm for Pr^{3+} emission in the monoclinic low temperature phase for T ≤ 190 K. At T = 8 K the intra-centre excited Pr^{3+} 5d-4f

emission demonstrates a nearly single exponential decay curve which can be suitably fitted with a lifetime τ = 14.8 ns.
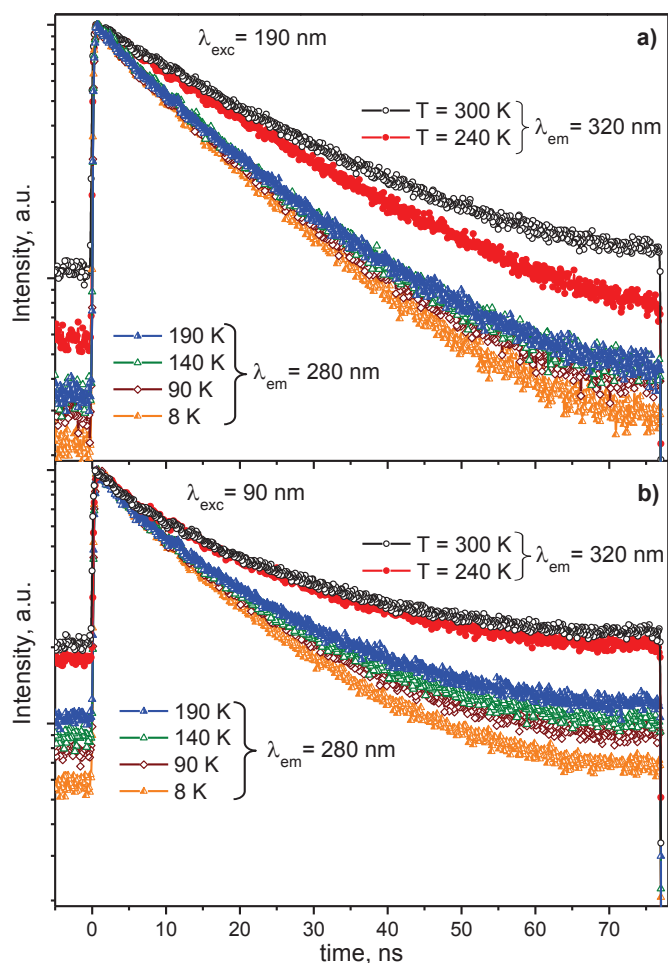

Fig. 4.12 Decay curves recorded monitoring 5d-4f emission of Pr^{3+} upon intra-centre excitation at 190 nm (a) and host excitation at 90 nm (b) at various temperatures.

Interestingly, at higher temperatures the decay curves demonstrate a slight contribution from a shorter decay component that is likely due to a partial quenching of the emission by some quenching centers. We note that somewhat similar effect was observed in the decay curves recorded for KLuP single crystals and for other double phosphate of $A_3Lu(PO_4)_2$-type (A = Li, Rb, Cs) doped with Ce^{3+} ions [25-27]. In addition, the emission decay profiles become progressively longer with temperature increasing, that correlates with the previously observed shift of the Pr^{3+} 5d-4f emission band toward longer wavelengths (Fig. 4.10). To qualitatively analyse the effect of the temperature on the excited state dynamics of Pr^{3+} in KLuP we approximated the non-exponential

decay profiles as a sum of two exponential functions and quantified the decay processes by using an average decay time τ_{avg} as suggested in [31]:

$$\tau_{avg} = (A_1\tau_1^2 + A_2\tau_2^2)/(A_1\tau_1 + A_2\tau_2) \tag{4.1}$$

where τ_1 and τ_2 represent short- and long-lifetimes, respectively, and A_1 and A_2 the corresponding intensity coefficients. The calculated average decay time for the decay curves recorded at 90, 140, 190, 240 and 300 K are summarized in Table I.

Table I. Average decay times for Pr^{3+} 5d-4f luminescence in KLuP at various temperatures upon both intra-centre ($\lambda_{exc} = 190$ nm) and band-gap ($\lambda_{exc} = 90$ nm) excitation.

T(K)	λ_{em} (nm)	τ_{avg} (ns)	
		$\lambda_{exc} = 190$ nm	$\lambda_{exc} = 90$ nm
90	280	15.1	15.2
140	280	15.7	15.6
190	280	16.0	16.5
240	320	19.4	19.5
300	320	20.3	19.9

The lifetime for the 320 nm emission at RT is a factor 1.5 faster than that observed for 280 nm emission at 8 K. On the basis of a recent analysis carried out by Zych et *al.* [32]; considering that the maximum emission intensity in the RT spectrum is located at $\lambda_{em} = 275$ nm and that revealed in the spectrum at 8 K is located at $\lambda_{em} = 256$ nm, a factor of 1.2 is to be expected in our case.

The decay curves recorded upon host excitation at various temperatures (Fig. 4.12-b) show a significant contribution of a slow decay component (probably with a micro- or millisecond lifetime) presented as a piling-up, that could be related to the presence of defects (afterglow). Nevertheless, the main decay component is found to be characterized by an average decay time very similar to that calculated for the curves recorded upon direct excitation (see Table I). Furthermore, it is important to note that the decay curves do not display any significant rise of the emission intensity just after the excitation pulse indicating that the excitation energy is very rapidly transferred to the emitting centers; this is a crucial requirement to produce a good scintillator material for applications such as those based on time-correlated detection of photons.

4.2.5 Conclusions

In summary, KLuP doped with Pr^{3+} ions has been synthesized by a solid state reaction. The time-resolved VUV luminescence spectroscopic properties of the material have been studied using synchrotron radiation. Upon both direct intra-centre and band-gap excitation the emission of KLuP:Pr^{3+} is dominated by Pr^{3+} 5d-4f interconfigurational radiative transitions. The VUV excitation spectra clearly demonstrated a high efficiency of the host-to-Pr^{3+} energy transfer in KLuP. Luminescence spectra as well as decay curves displayed significant changes with the temperature within the range 8-300 K reflecting the crystal phase transitions of this compound documented in [25]. The decay curves of the 5d-4f emission of Pr^{3+} recorded upon both direct and band-gap excitation at 8 K are characterized by decay times of about 15 ns. The increase of the lifetimes up to about 20 ns evidenced at RT correlates with shift of the Pr^{3+} 5d-4f emission towards longer wavelength and is determined by the phase changes followed by increase of the covalency in the Pr-O bonds. Finally, the VUV spectroscopic properties of KLuP:Pr^{3+} along with its high effective atomic number revealed good potentialities for application of this material as a fast scintillator. To support the latter, additional experimental studies of scintillating properties such as energy resolution, light yield and decay time upon excitation with pulsed X- or gamma-ray sources are required.

4.3 $KLuP_2O_7:Pr^{3+}$

4.3.1 Introduction

$KLuP_2O_7$ host is characterized by a high effective atomic number of ~52.3, similar to that of $Lu_3Al_5O_{12}$, and potentially advantageous for γ-ray scintillators. Due to the wide band gap and the suitability for doping with rare earth activators, the optical properties of several alkali rare-earth phosphates belonging to the A_2O-RE_2O_3-P_2O_5 (A = alkali metal ion, RE = rare earth metal) system have been recently investigated under VUV and X-ray radiation to demonstrate the potential as scintillating materials [27, 33] Some room temperature luminescence properties of Ce^{3+} and Pr^{3+} doped $KLuP_2O_7$ have been studied in [28, 34]. Particularly, it was shown that Ce^{3+} doped $KLuP_2O_7$ produces efficient and fast *d-f* emission upon X-ray excitation with a lifetime of the dominating decay component of about 27 ns [34]. The results obtained for Pr^{3+} doped $KLuP_2O_7$ in [28] included intra-centre (4*f*-5*d*) excited emission spectrum and excitation spectra recorded down to about 140 nm. To the best of our knowledge, time-resolved vacuum ultraviolet (VUV) spectroscopy and excited state dynamics under excitation with synchrotron radiation (SR) of Pr^{3+} doped $KLuP_2O_7$ has not been reported in the literature so far. Moreover, this promising material is lacking a low-temperature study that would help to establish the nature of host-to-impurity energy transfer.

In this contribution we present and analyze time-resolved emission and excitation spectra as well as luminescence decay curves measured at room and liquid helium temperature upon selective excitation with synchrotron radiation (SR) in the UV/VUV region (down to about 61 nm). In addition, the prospective applications of this luminescent material are discussed.

4.3.2 Experimental details and structural information

Powder crystalline materials having stoichiometry $KLu_{0.99}Pr_{0.01}P_2O_7$ (*i. e.* containing 1 mol % Pr^{3+} substituting for Lu^{3+}) were obtained by solid state reaction from high purity KNO_3, $(NH_4)_2HPO_4$, Lu_2O_3 and Pr_6O_{11} (the last two reagents 4N). Appropriate amounts of the reagents were mixed and heat treated in a horizontal furnace in air for 1 h at 400 °C and 24 h at 750 °C with intermediate regrinding.

Powder X-ray diffraction patterns were measured with a Thermo ARL X′TRA powder diffractometer, operating in the Bragg-Brentano geometry and equipped with a Cu-anode X-ray source (K_α, $\lambda = 1.5418$ Å) with a Peltier Si(Li) cooled solid state detector.

All the diffraction peaks in the powder patterns of Pr^{3+}-doped $KLuP_2O_7$ (Fig. 4.13) are compatible with ICDD data on $KLuP_2O_7$ (PDF Card No. 01-076-7386). No other phases were detected, indicating that the synthesized sample is a single phase. This compound crystallizes in a monoclinic structure belonging to space group $P2_1/c$ (n° 14) [34].
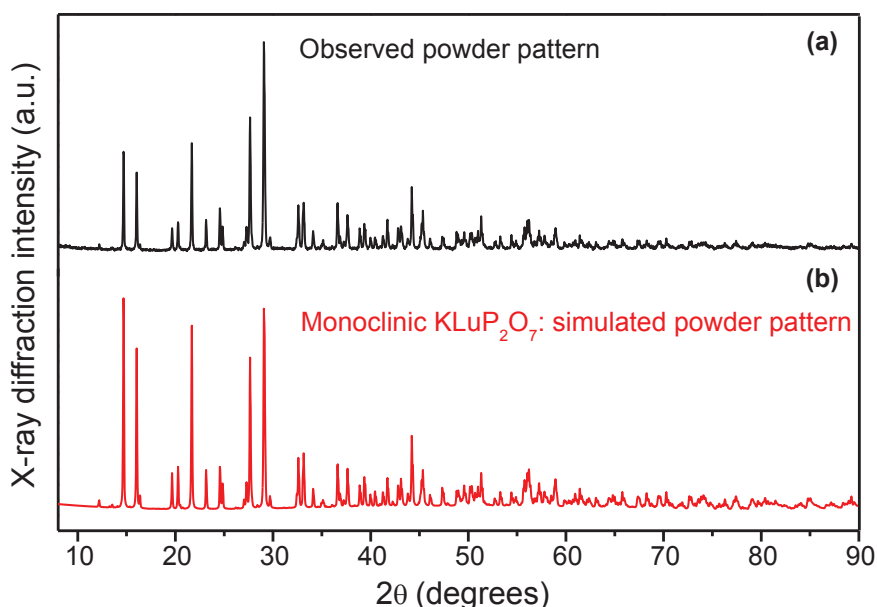
Fig. 4.13 Experimental powder pattern of the $KLuP_2O_7$:1% Pr^{3+} powders (a) and simulated pattern of $KLuP_2O_7$ (PDF card number 01-076-7386) (b).

The crystalline structure of $KLuP_2O_7$ offers only one site for Lu^{3+} (or Pr^{3+}) with a coordination number of 6 of a C_1 point symmetry. In addition, we observed a small expansion of the cell volume as a consequence of substitution of Lu^{3+} ion (ionic radius 0.861 Å, in six-fold coordination [8]) by the larger Pr^{3+} ion (0.99 Å, in six-fold coordination [8]). The cell volume of the Pr^{3+} doped sample and the undoped one are 666.45(1) Å^3 and 665.94(1) Å^3 (PDF Card No. 01-076-7386 and [34]), respectively.

Time-resolved VUV spectroscopic measurements were carried out at the SUPERLUMI station of HASYLAB (Hamburg, Germany) described in more detail in section 3.2.1. The time-resolved spectra were recorded within two time gates (TG): 2-11 ns (fast TG) and 50-71 ns (slow TG) relative to the beginning of the SR pulse. The time-integrated spectra were recorded counting

the emission signal within the whole time period of 96 ns available between SR pulses at 10 bunch mode of the storage ring.

4.3.3 Results and discussion

Fig. 4.14 shows emission spectra of $KLuP_2O_7:Pr^{3+}$ recorded upon SR excitation at T = 300 K. The time-resolved and time-integrated spectra obtained upon direct intra-center excitation at 210 nm (5.9 eV) (Fig. 4.14-a) show by a broad band located in the UV spectral region (225-350 nm). This band is well pronounced in the fast time gated spectrum, and it is assigned to the parity-allowed 5d-4f transitions from the lowest excited state of the $4f^1 5d^1$ configuration to the multiplets belonging to the $4f^2$ ground configuration of Pr^{3+}. No emission features associated with 4f-4f transitions from the $^3P_0$ and $^1D_2$ levels which are expected to be located around 490 and 600-650 nm, respectively, are observed.
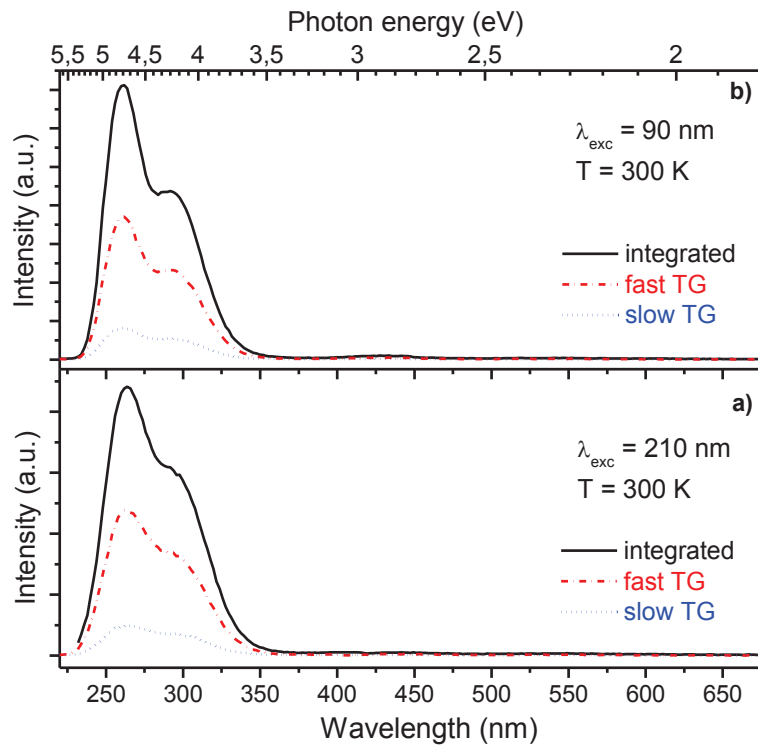

Fig. 4.14 Time-integrated and time-resolved emission spectra of $KLuP_2O_7:Pr^{3+}$ powders recorded upon selective excitation at 210 nm (a) and 90 nm (b) at 300 K.

Fig. 4.14-b presents room temperature time-integrated and time-resolved emission spectra recorded upon excitation at 90 nm (13.8 eV) that corresponds to excitation across the band-gap.

The latter is located around 7.7 eV (~160 nm) in many phosphates of the type $AREP_2O_7$ (RE = Y, Lu) [11] and in other complex phosphates does not exceed 9.3 eV (see [14] and references therein). The spectra show profiles quite similar to that observed upon direct intra-centre excitation, indicating a fast and efficient energy transfer from the host to the impurity.

Time-integrated and time-resolved excitation spectra recorded for Pr^{3+} 5d-4f emission measured at 300 and 8 K are shown in Figs. 4.15-a and 4.15-b, respectively. The intra-centre Pr^{3+} 4f-5d transitions to the crystal field components belonging to the $4f^1 5d^1$ configuration are observed as an unresolved band in the UV region between 200 and 250 nm (5 - 6.4 eV) that is in agreement with the $KLuP_2O_7$:Pr^{3+} excitation spectrum presented in [28]. The lowest energetic maximum in this band that is most pronounced at low temperature is located around 230 nm (5.39 eV). This is consistent with the position (231 nm) predicted with the Dorenbos model [5], using the data on the energy of 4f-5d transitions for Ce^{3+} in the same host [28].
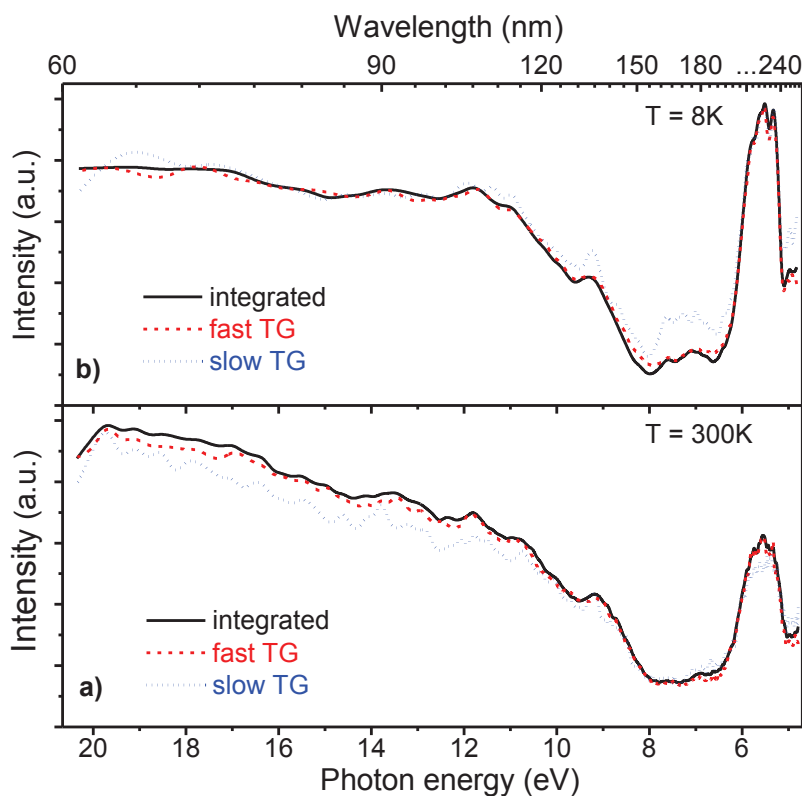

Fig. 4.15 Time-integrated and time-resolved excitation spectra monitoring 5d-4f emission of Pr^{3+} in $KLuP_2O_7$:Pr^{3+} powders at T = 300 K (a) and T = 8 K (b).

The time-integrated excitation spectrum recorded at T = 8 K shows a relatively broad excitation feature centered at 175 nm and most pronounced in the slow time gated spectrum. This

weak band can be attributed to the defect absorption. A gradual rise of the excitation spectra observed below 159 nm (> 7.8 eV) and 155 nm (> 8 eV) at T = 300 and 8 K, respectively, is likely to be connected with a beginning of the fundamental absorption of the host that correlates with the bandgap energies reported for similar double phosphates in Ref. [11]. The absence of an excitonic peak suggests that the host-to-impurity energy transfer mechanism is dominated by a recombination mechanism.

The decay curves of the Pr^{3+} 5d-4f emission measured at 8 and 300 K upon both intra-centre and band-gap excitations are presented in Fig. 4.16. Upon direct excitation into the $4f^1 5d^1$ states at 210 nm (5.9 eV) the decay curves are single exponential with a lifetime of about 20 ns both at 8 and 300 K (Figs. 4.16-a and 4.16-b) that suggests the absence of any intra-center quenching mechanisms up to T = 300 K.
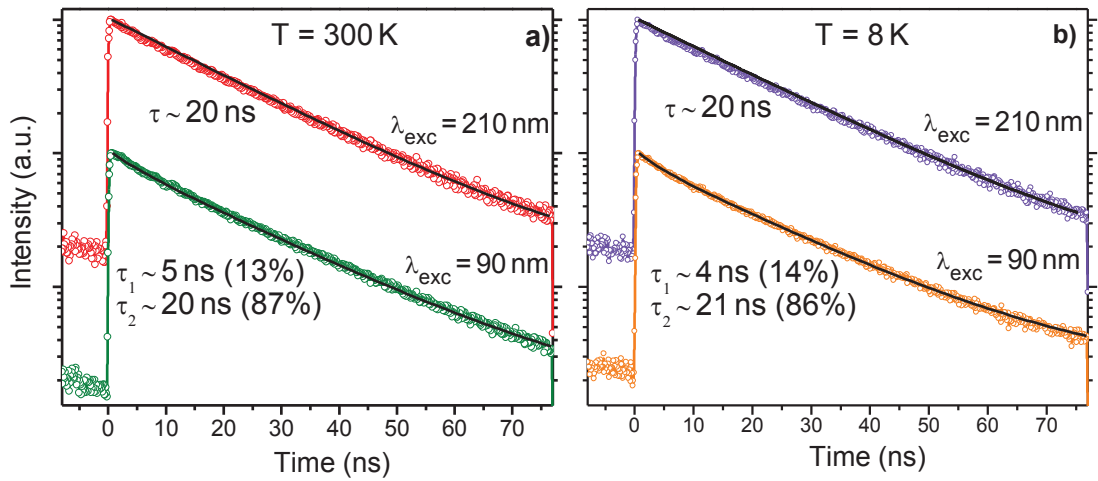

Fig. 4.16 Decay curves recorded monitoring *5d-4f* emission of Pr^{3+} at 300 nm upon intra-centre excitation at 210 nm and host excitation at 90 nm at *T* = 300 K (a) and *T* = 8 K (b).

This value is very close to the radiative lifetime [32] and this fact, together with the absence of temperature dependence, indicates clearly that non-radiative quenching processes are not operative in the material under investigation. On the other hand, the decay curves obtained upon band-gap excitation (Figs. 4.16-a and 4.16-b) demonstrate the existence of an additional faster decay component with lifetime τ_1 = 4-5 ns whose intensity accounts for about 13-14 % in total decay process. The presence of a faster decay component can be tentatively explained as a result of surface quenching. The latter comes from the fact that VUV photons with energy exceeding the bandgap are absorbed in a very thin (submicron) layer of the sample due to very high host absorption. As a result some part of the electronic excitations transfer energy to Pr^{3+} ions localised

in the vicinity of surface related defects which may play a role as quenching centers. We note that a somewhat similar effect was observed in the decay curves recorded for $KLuP_2O_7$ powders doped with Ce^{3+} upon X-ray excitation [34]. It may thus be concluded that host-to-Pr^{3+} energy transfer is characterized by a very fast dynamics that seems to be independent of excitation energy across the range from the beginning of fundamental absorption to the upper limit of the measurement (20.4 eV). The letter is particularly suggested by the fact that the fast and slow time gated excitation spectra closely follow the time-integrated ones in this energy range at both T = 8 and 300 K. In addition, it is worth noting that the Pr^{3+} 5d-4f emission decay curves do not reveal any significant rise time within the time resolution capabilities of the setup (better than 1 ns). This indicates that excited Pr^{3+} $4f^1 5d^1$ states do not experience any thermally assisted population of the emitting level that is typically connected with delocalisation of electrons from shallow traps. Overall, the results of the study of dynamic and time-resolved VUV spectroscopic properties of $KLuP_2O_7$ doped with Pr^{3+} revealed its potentials for fast scintillator applications. Obviously, additional experimental studies of scintillation properties such as energy resolution, light yield and decay time upon excitation with pulsed X- or γ-ray sources are required to establish the scintillation performance of the material.

4.3.4 Conclusions

In summary, $KLuP_2O_7$ doped with Pr^{3+} ions has been synthesized by solid state reaction. The time-resolved VUV luminescence spectroscopic properties of the material have been studied using synchrotron radiation. Upon both direct intra-center and band-gap VUV excitation the emission of $KLuP_2O_7$:Pr^{3+} is dominated by Pr^{3+} 5d-4f interconfigurational radiative transitions with a lifetime of approximately 20 ns. The lifetime is found to be temperature independent within the range 8–300 K and no build-up of the luminescence at short time scale is observed. The VUV excitation spectra clearly demonstrated high efficiency of host-to-Pr^{3+} energy transfer in $KLuP_2O_7$:Pr^{3+}. Due to the efficient and fast host-to-impurity energy transfer along with the good chemical stability of the matrix, $KLuP_2O_7$:Pr^{3+} may provide a new interesting addition to the arsenal of available dense scintillators for detection of γ-rays.

4.4 X2-Lu$_2$SiO$_5$:Pr^{3+} nanopowders

4.4.1 Introduction

Since its discovery by Melcher and Schweitzer in 1992 [35], lutetium oxyorthosilicate Lu$_2$SiO$_5$ (LSO) activated with Ce^{3+} ions has stimulated a great interest as possible single crystal scintillator material due to its mechanical and thermal stabilities, high density (7.4 g/cm^3), high light yield (~30000 photons/MeV) and short decay time (~40 ns). To the best of our knowledge, 5d-4f luminescence of Pr^{3+} ions in nanocrystalline LSO has not been reported in literature so far, although the luminescence spectroscopy of sol-gel prepared LSO powders doped with Ce^{3+} has been documented [36]. Meanwhile, luminescence and scintillation properties of single crystals of LSO:Pr^{3+} as well as Lu$_2$Si$_2$O$_7$:Pr^{3+} (LPS), that is another compound in the same Lu$_2$O$_3$-SiO$_2$ system, have been thoroughly investigated [37-39]. At the same time, we point out that scintillator materials in the form of nanocrystalline powders are an emerging field of research as the nano-scale induces the appearance of new optical properties which, in turn, bring new conceptions for application of such materials and open opportunities for improvement of exploitation characteristics of the radiation detectors including their sensitivity, spatial and temporal resolutions, radiation hardness, etc. [40-42]. For these reasons, nanosized scintillating materials hold good promises for future applications in new generations of devices for medical diagnostics, security inspection, radiation monitoring, etc.

Based on these considerations, we found it interesting to synthesize and study the spectroscopic properties of nanocrystalline X2-LSO doped with Pr^{3+}. Since the optical properties of nanomaterials are strongly dependent on size, morphology, and synthesis conditions, we performed a transmission electron microscopy (TEM) study of the product synthesized. To evaluate the potential of nanocrystalline X2-LSO:Pr^{3+} for scintillator and X-ray phosphor applications we performed a luminescence spectroscopic investigation of the material upon VUV and X-ray excitation. Time-resolved experimental methods were used to investigate the dynamics Pr^{3+} 5d-4f emission of the host-to-impurity energy transfer.

The material was synthesized by an innovative soft chemistry route, namely the sol-gel process [43], which allows producing nanocrystalline LSO:Pr^{3+} at a low cost with a higher morphology control of the particles and a better dispersion of doping ions throughout the host compared to the traditional methods.

4.4.2 Experimental details

Nanocrystalline powders of X2-LSO doped with 1 mol% of Pr^{3+} have been prepared by the sol-gel process, slightly modifying the method described in [44]; the resulting amorphous powders were heat treated in air at 1100°C for 3 hours. In between investigations the samples were stored at RT in dark and dry conditions.

X-ray diffraction patterns (XRPD) were measured with a Thermo ARL X′TRA powder diffractometer, operating in the Bragg-Brentano geometry and equipped with a Cu-anode X-ray source (K_{α}, $\lambda = 1.5418$ Å) with a Peltier Si(Li) cooled solid state detector.

TEM analysis was performed using a Philips CM200 HR-TEM operating at an accelerating voltage of 200 kV. The nanocrystalline X2-LSO:Pr^{3+} powder was dispersed in ethanol and sonicated for 10 minutes to ensure a homogeneous dispersion. A small drop was deposited on a nickel grid of 200 mesh coated with an amorphous-carbon film and dried in vacuum before being put into the TEM chamber. The particle size was determined by measuring the nanoparticles from TEM images using "Image J" software.

The time-resolved VUV spectroscopic measurements were carried out at the SUPERLUMI station of HASYLAB (Hamburg, Germany) described in more detail in section 3.2.1. The time-resolved spectra were recorded within two time gates (TGs): 2-13 ns (fast time gate) and 120-170 ns (slow time gate) relative to the beginning of the SR pulse. The time-integrated spectra were recorded counting emission signal within the whole time period of 192 ns available between SR pulses at normal (5) bunch mode (BM) of the storage ring. The decay curves were recorded at reduced (2) BM allowing a longer time range.

X-ray induced luminescence was stimulated using a Tungsten tube (Philips) operated at 35 kV, 25 mA with a 0.7 mm thick aluminium filter in the beam. The X-ray excited steady-state spectra were recorded at room temperature (RT) using an Ocean Optics 4000B spectrometer with the light guided to the spectrometer via an optical fibre.

All the emission spectra presented in the paper were recorded using 420 nm long pass filter to eliminate the second-order effects of the UV emission.

4.4.3 Structural characterization

The structural characterization of the synthesized sample was performed by X-ray powder diffraction (XRPD). All the diffraction peaks in the XRPD patterns of Pr^{3+}-doped X2-LSO nanopowders are compatible with the monoclinic X2 phase of LSO [45] (Fig. 4.17), as proved by

Rietveld calculations (MAUD program) [46]. No other phases are detected, indicating that the sample synthesized is single phase.
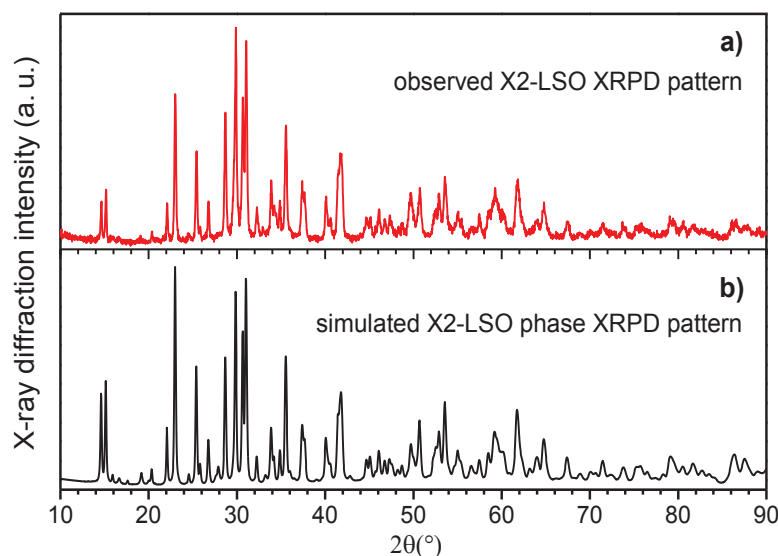

Fig. 4.17 Experimental XRPD pattern of the X2-LSO: 1%Pr^{3+} nanocrystalline powders (a) and XRPD pattern of X2-LSO simulated from the X-ray single crystal structure reported in [45]).

X2-LSO crystallizes in the monoclinic system with space group C2/c (no. 15). Lutetium ions occupy two crystallographic sites of low symmetry (C_1) with seven and six oxygen neighbours, respectively [45]. It is worth noting that the site with 7-fold coordination is larger than the one with 6-fold coordination. According to the substitution of 1% of Lu^{3+} (ionic radius 0.97 Å, in 8-fold coordination [8]) with the same amount of the larger Pr^{3+} ion (1.14 Å, in 8-fold coordination [8]), we observed a small expansion of the cell volume. In fact, the lattice parameters of the doped and the undoped sample are a=14.239(2) Å, b=6.644(1) Å, c=10.272(1) Å, β=122.137(6)° and a=14.2774 Å, b=6.6398 Å, c=10.2465 Å, β=122.224° [45], respectively. As a consequence, the cell volume of the doped sample [822.90(1) Å^3] is slightly larger than that of the undoped one (821.74 Å^3). Several representative TEM images of X2-LSO:Pr^{3+} nanoparticles are gathered in Fig. 4.18. The nanoparticles are fairly uniform and tend to loosely aggregate. The size of nanoparticles was measured over 80 nanoparticles using an oval shape approximation. Results showing the average major and minor sizes as well as the size distribution are presented in Fig. 4.19. Average dimensions of the nanoparticles are about 35 x 44 nm in the oval shape approximation. An average minor-to-major size ratio is about 80% with quite narrow distribution of about 12%. Note, the monoclinic structure of X2-LSO can be seen in the high-resolution TEM images.
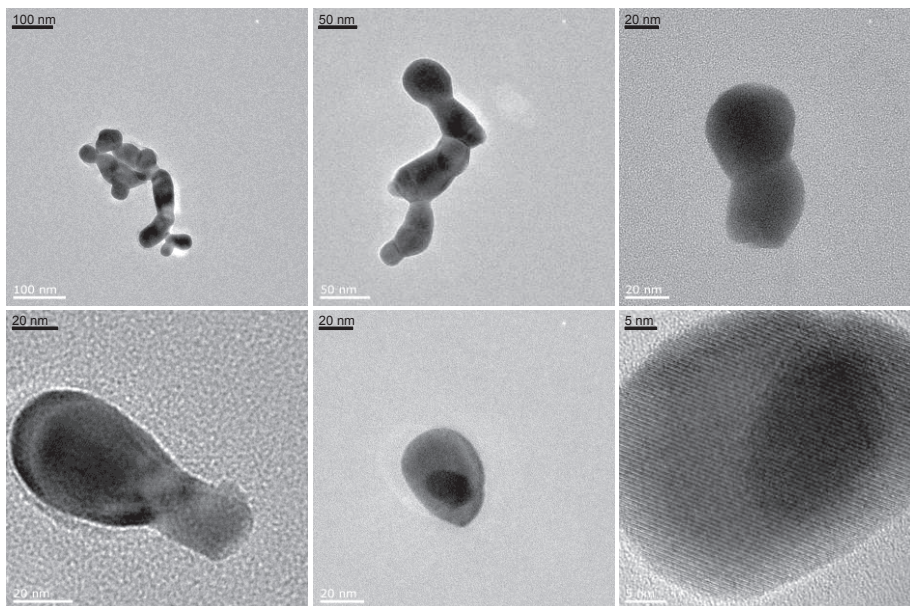
Fig. 4.18 TEM images of X2-LSO: 1%Pr^{3+} nanoparticles. The white scale bars were added to the images by the image processor of Philips CM200 HR-TEM at the time of measurement. The black scale bars were added manually for easier reading.
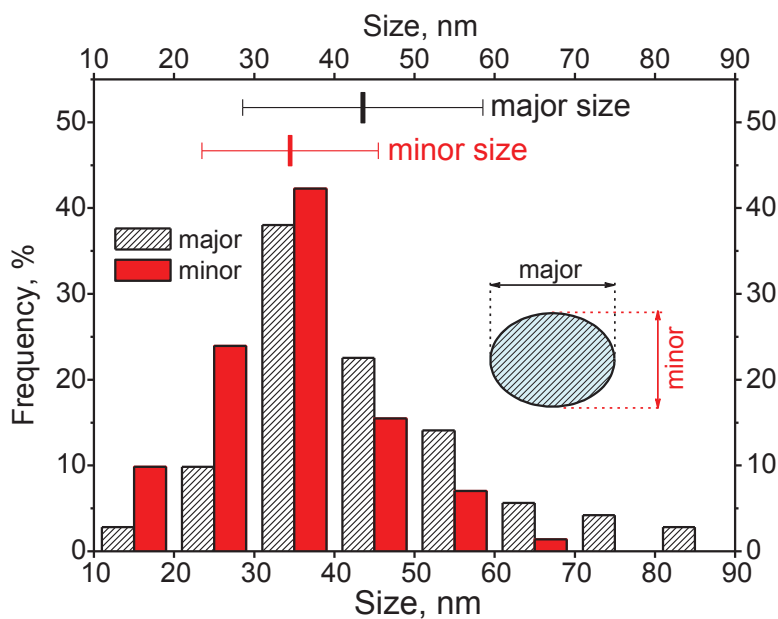

Fig. 4.19 Size distribution measured over 80 nanoparticles using an oval shape approximation (vertical bars); average major and minor sizes of the nanoparticles and standard deviation (top of the graph, values with standard error bars).

4.4.4 Luminescence spectroscopy and dynamics

Fig. 4.20 gathers emission spectra of nanocrystalline X2-LSO:Pr^{3+} recorded upon SR and X-ray excitation at T = 300 K.
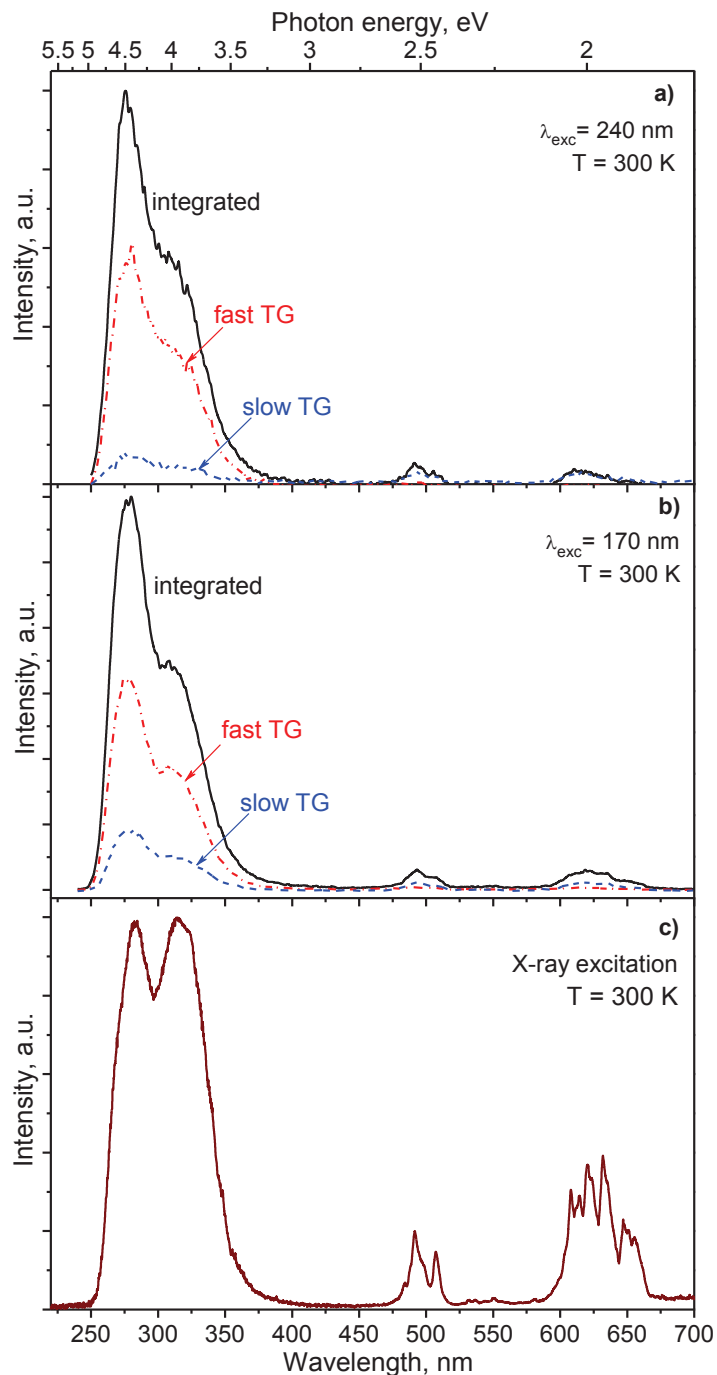

Fig. 4.20 Time-integrated and time-resolved emission spectra of X2-LSO:Pr^{3+} nanopowders recorded upon selective excitation at 240 nm (a) and 170 nm (b) with SR and X-ray excited steady-state emission spectrum. All the spectra were recorded at T = 300 K.

Time-resolved and time-integrated emission spectra of nanocrystalline LSO:Pr^{3+} obtained upon direct intra-centre excitation at 240 nm (Fig. 4.20-a) are dominated by a broad band located in the UV region. The band is well pronounced in the fast TG spectrum and is assigned to the parity-allowed 5d-4f transitions from the lowest excited 5d state to the multiplets of the $4f^2$ ground configuration of Pr^{3+}. Additionally, very weak emission features around 490 and 600-650 nm present in the slow time gated spectrum are assigned to 4f-4f transitions from the $^3P_0$ and $^1D_2$ levels. Fig. 4.20-b presents RT time-integrated and time-resolved emission spectra recorded upon excitation at 170 nm, that corresponds to transitions across the band-gap. The latter (E_g) is located at about 6.6 - 6.8 eV ($\sim$ 184 nm) as suggested by the analysis of available VUV reflection and excitation spectra and band-structure calculations (see [47, 48] and references therein). The spectra show spectral profiles quite similar to that observed upon direct intra-centre excitation. No additional spectral features nor change of the relative intensity of the Pr^{3+} emission components related to 5d-4f and 4f-4f transitions are observed in the host excited spectra. At the same time, one may notice a nearly twofold increase of the intensity of signal detected within slow TG around the features related to Pr^{3+} 5d-4f transitions indicating the existence of some delayed host-to-impurity energy transfer processes. Fig, 4.20-c shows the X-ray excited steady-state emission spectrum of the X2-LSO:Pr^{3+} nanopowder. Apart from the different relative intensities of the emission features, the spectrum is generally similar to the above discussed SR excited time-integrated emission spectra. The different profile of the X-ray and SR excited spectra is due to the different spectral sensitivity of the employed emission spectrometers. It is worth noting that the intensity of the measured X-ray excited emission signal was well above average for the setup; this is useful for the discussion about the efficiency of the energy transfer from host electronic excitations to Pr^{3+} ions.

Time-integrated and time-resolved excitation spectra recorded for Pr^{3+} 5d-4f emission at 300 K are presented in Fig. 4.21. The time-resolved spectra are scaled by factor 3 for better representation. Intra-centre Pr^{3+} 4f-5d transitions to the lowest energetic $5d_1$ and $5d_2$ crystal field components are presented in the spectra by a doublet excitation band in the UV region. As can be seen from the time-resolved spectra this band is mainly formed by the signal detected within the fast TG. The intense onset observed in the time-integrated and the time-resolved spectra near 195 nm represents the beginning of fundamental optical absorption of the host, particularly creation of free excitons [49]. In these conditions the quantum yield of the nanopowder is close to the one observed upon direct 4f-5d excitations of Pr^{3+} ions. Below about 184 nm, where the exciting photons create separate electron-hole pairs, the time-integrated and fast TG excitation spectra demonstrate a tendency to rise gradually until about 105 nm. This observation suggests the presence of quite efficient host-to-impurity energy transfer that is dominated by a recombination mechanism.
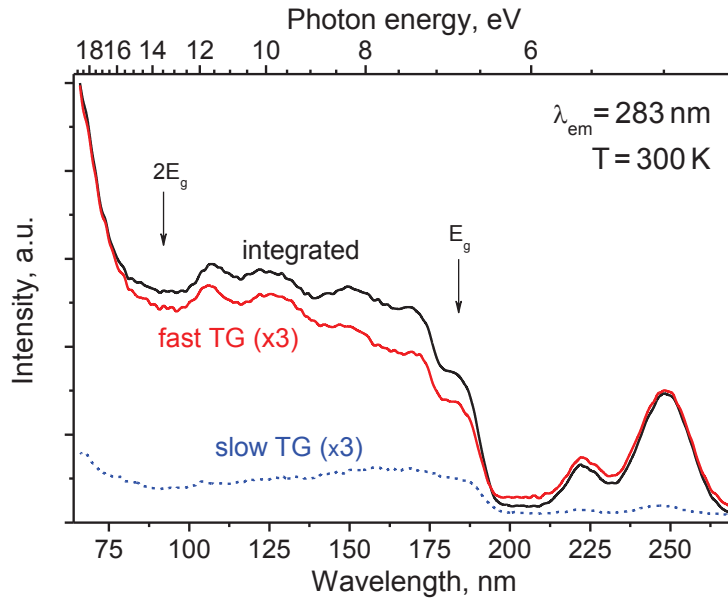
Fig. 4.21 Time-integrated and time-resolved excitation spectra monitoring 5d-4f emission of Pr^{3+} in X2-LSO:Pr^{3+} nanopowders at T = 300 K.

Following the well developed conception of migration losses [50-52] it may be expected to observe an opposite behaviour of the spectra, particularly a decrease of quantum yield caused by the increase of the mean distance between "genetically" connected (created with the same photon) electrons and holes due to increased escape during the thermalization stage. The slow TG spectrum demonstrates the development of a delayed energy transfer processes whose contribution (fraction) is nearly constant upon excitation across the band gap. The drastic increase of excitation efficiency below about 92 nm that corresponds to $2E_g$ is related to the multiplication of electronic excitations when inelastic scattering of primary electronic excitations results in creation of secondary ones [50-53].

The fact that the intensity of the 4f-5d excitation bands is noticeably lower than that for the host-related VUV features in the time-integrated spectrum may be connected with the wavelength dependent Rayleigh scattering of excitation light on nanoparticles as suggested elsewhere for nanophosphors of similar size [54]. This problem, however, requires further experimental and theoretical investigation to get insight into the nature of light interaction with assembled nanoparticles and their aggregates.

The decay curves of the Pr^{3+} 5d-4f emission taken upon both intra-centre and band-gap excitations at different temperatures are presented in Fig. 4.22-a and Fig. 4.22-b, respectively. At T = 8 K the intra-centre excited Pr^{3+} 5d-4f emission demonstrates an approximate single exponential decay curve which can be satisfactory fitted with a lifetime τ = 20 ns. This is somewhat shorter than the lifetime of 25 ns reported for LSO:Pr^{3+} single crystal [26, 37]. The 8 K decay curve

recorded upon band-gap excitation shows the appearance of slower decay components. The band gap excited decay curve can be fitted using a double exponential function with $\tau_1 = 20$ ns and $\tau_2 = 88$ ns. The τ_1 parameter was kept fixed at 20 ns in the fitting and was regarded as an intrinsic radiative lifetime (τ_{rad}), a fundamental characteristic of an emitting centre which is supposed to be independent on excitation energy. The values of other parameters used to fit the 8 K decay curves can be found in Fig. 4.22. We note that the 8 K band-gap excited decay curve also demonstrates the existence of a much slower decay component (possibly of (micro- or millisecond range) which appears as an increased constant level (piling) due to overlay of the emission decay pulses excited by continuous sequences of excitation pulses arriving with a high repetition rate (see [26] for details). The conditions for the decay measurements with reduced BM available at the DORIS III storage ring give rise to a minimization of this effect in comparison to usual timing conditions available at the facility.

At higher temperatures the intra-centre decay curves show a departure from the exponential behaviour reflecting the development of a complex quenching processes. In addition, the decay curves are characterized by a slight increase of the intensity of the slower (sub-microsecond) decay components. A fitting of such decay curves can be quite ambiguous, mainly due to the fact that the choice of an adequate fitting function able to match the real physical processes lying behind the quenching of emission in nanoparticles is obviously a very challenging task. We suppose that in nanocrystalline X2-LSO:Pr^{3+} the typical quenching of Pr^{3+} 5d-4f emission observed in LSO:Pr^{3+} single crystals induced by photoionization [37, 55] is accompanied by a quenching due to surface defects, as commonly expected for nanophosphors (see [40], [56, 57] and references therein). We should note, however, that in some cases the extent of surface related quenching effect may be controlled by the preparation method [58]. The appearance of the slower decay components observed in higher temperature decay curves even upon intra-centre excitation is probably related to retrapping of delocalized 5d electrons by non-parent Pr^{4+} ions.

To qualitatively analyze the temperature induced quenching of intra-centre excited luminescence we quantified the decay processes by using an average decay time τ_{avg} as suggested in [59]

$$\tau_{avg} = \int_0^\infty I(t)t\,dt \left/ \int_0^\infty I(t)\,dt \right. , \tag{4.2}$$

where $I(t)$ represents the luminescence intensity at time t.

At T = 8 K the average decay time is equal to the lifetime obtained with single exponential fitting function (see above). When the temperature increases up to 300 K a substantial shortening

down to 11 ns occurs (Fig. 4.22-a). The temperature dependence of the Pr^{3+} decay time in nanocrystalline $LSO:Pr^{3+}$ is different from that reported for $LSO:Pr^{3+}$ single crystals [37, 38]. Particularly, the onset of temperature quenching observed near 70 K for the nanocrystalline X2-$LSO:Pr^{3+}$ occurs at lower temperature than that for $LSO:Pr^{3+}$ single crystal (~220 K). At the same time the slope of the temperature dependence is steeper in case of the crystal. This, however, can be related to obvious limitations in the evaluation procedure which integrates effects resulting in both the thermal quenching of the Pr^{3+} 5d-4f emission and slow sub-microsecond processes related to retrapping of 5d electrons.
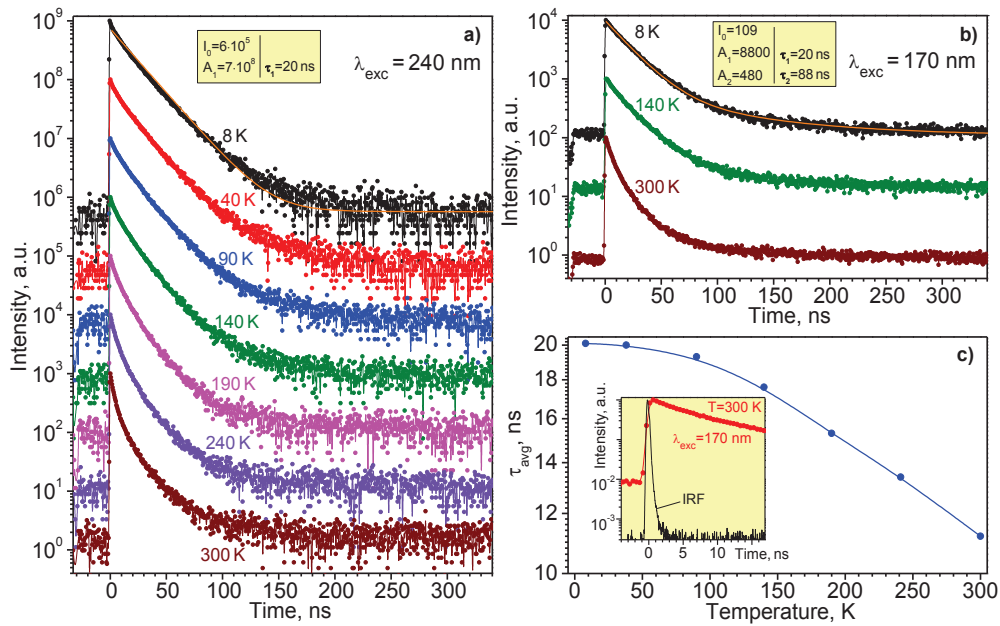

Fig. 4.22 Decay curves recorded monitoring Pr^{3+} 5d-4f emission at 283 nm upon intra-centre excitation at 240 nm (a), host excitation at 170 nm (b) at different temperatures; temperature dependence of the average decay time for intra-centre excited Pr^{3+} 5d-4f emission with the solid line as a guide for the eye (c). The 8 K decay curves in panels (a) and (b) are confronted with the fitting functions $I(t) = I_0 + A_1 \cdot exp(-t/\tau_1)$ and $I(t) = I_0 + A_1 \cdot exp(-t/\tau_1) + A_2 \cdot exp(-t/\tau_2)$, respectively. Rounded-off values of the fitting parameters are shown in the panels. The inset in panel (c) shows a zoom-in of IRF compared with the host excited 300 K decay curve.

Some degree of the non-exponential decay is also observed for the band-gap excited decay curves of the Pr^{3+} 5d-4f emission recorded at T = 140 K and T = 300 K. A simple recombination of electron-hole pair on an impurity centre is a single-exponential process. Hence, the deviation from the exponential behaviour observed in the band-gap excited decay curves is determined by the host-to-impurity energy transfer and quenching processes. Given the fact that the effective diffusion length of the host electronic excitations is comparable with the size of nanoparticles we may suppose that this increases the possibility of their transfer to Pr^{3+} ions localised near the surface of the nanoparticles. Such ions, in turn, may experience some degree of non-radiative quenching on

defects related to small perturbations on surfaces of the nanoparticles [60]. It is also worth mentioning the quite often observed tendency of impurity ions, and lanthanides in particular, to segregate on the surface of nanoparticle phosphors (see [61-63] for reference). This may also give rise to quenching of luminescence due to increased number of closely spaced emitting centres.

As a last remark regarding to dynamics of the host-to-impurity energy transfer in nanocrystalline X2-LSO:Pr^{3+}, we note that no significant build-up of the luminescence is observed upon band-gap excitation. This is shown by example in the 300 K band-gap excited decay curve compared with the instrumental response function (IRF) in Fig. 4.22-c, Inset. Although time the sampling interval of the registration system was not especially adjusted to record the build-up stage in more details, the data presented suggest that the population of the Pr^{3+} 5d emitting levels occurs in less than 1-2 ns. This is useful for scintillator applications based on time-correlated detection of photons.

The overall results on the time-resolved VUV spectroscopy and X-ray excited emission suggest that nanocrystalline X2-LSO:Pr^{3+} demonstrates quite promising luminescence properties in terms of efficiency of host-to-impurity energy transfer that can be favourable for X-ray phosphor and scintillator applications.

4.4.5 Conclusions

In summary, nanocrystalline powders of monoclinic X2-LSO:Pr^{3+} have been successfully synthesized using the sol-gel process. The structural characteristics and nanoscale morphology have been studied with XRD and TEM. The X2-LSO:Pr^{3+} nanoparticles have shown to characterized by an oval shape with average dimensions of 35x44 nm.

The investigation of the luminescence properties of the nanocrystalline X2-LSO:Pr^{3+} powders has been based on time-resolved VUV spectroscopy and accompanied by measurement of X-ray induced emission. The experimental results revealed efficient and fast transfer of host electronic excitations to emitting Pr^{3+} ions. Some evidence of thermally induced quenching processes has been observed and mainly attributed to surface related defects. Finally, nanocrystalline X2-LSO:Pr^{3+} belongs to a new class of nanosized optical materials with potential scintillator and X-ray phosphor applications.

4.5 X1- and X2-Y$_2$SiO$_5$:Pr^{3+} nanopowders

4.5.1 Introduction

Structural studies show that YSO contains isolated SiO$_4$ tetrahedral and non-silicon-bonded oxygen. This compound crystallizes in two different monoclinic structures depending on the heat treatment temperature: X1 type (synthesized at temperature less than 1190°C), space group P2$_1$/c [64] and X2 type (synthesized at temperature above 1190°C), space group B2/b [65]. In each of these two phases there are two possible Y^{3+} sites in the YSO matrix, Y1 and Y2. These two sites are attributed to the differences in coordination numbers (CN). In X1-YSO, Y1 and Y2 sites are coordinated by 9 and 7 oxygen atoms, respectively and in X2-YSO by 7 and 6 oxygen atoms, respectively.

YSO is characterized by a density of about 4.5 g/cm^3 and a effective atomic number of ~39 [66], which is similar to that of YPO$_4$ (32.5) [66] and YAlO$_3$ (31.4) [66] widely used as scintillator materials and particularly interesting for fast γ-ray detection in nuclear medicine. The luminescence and scintillation properties together with the polycristalline powder preparation and single crystal growth of the Ce^{3+}-doped YSO and LSO or (Lu,Y)$_2$SiO$_5$ structures were the subject of numerous studies in the recent years [38, 67-70] because of the efficient and fast 5d-4f luminescence of Ce^{3+} center in these hosts and their possible application in the field of luminescent phosphors and scintillators. This fact has initiated an effort to investigate the Pr^{3+}-doped analogues in order to obtain a potential faster emission which can be used in modern PET scanners. To the best of our knowledge, 5d-4f luminescence of Pr^{3+} ions in nanocrystalline YSO has not been reported in literature so far, although the optical and luminescence properties of Pr^{3+}-doped YSO single crystal have been thoroughly investigated from several authors [38, 71, 72]. To evaluate the potential of nanocrystalline X2-YSO:Pr^{3+} for scintillator applications we performed a luminescence spectroscopic investigation of the material upon VUV excitation by using synchrotron radiation as excitation source. Time-resolved experimental methods were used to investigate the dynamics Pr^{3+} 5d-4f emission of the host-to-impurity energy transfer.

4.5.2 Experimental details and structural characterization

In a typical experiment stochiometric amounts of $Y(NO_3)_3 \cdot 6H_2O$ (Aldrich, 99%) and $Si(OC_2H_5)_4$ (Aldrich 98%) were dissolved in a water/ethanol (v/v = 1/5) solution; 1 mol% of Pr^{3+} ion (ionic radius 1.14 Å, in eight-fold coordination [8]) as $Pr(NO_3)_3 \cdot 6\,H_2O$ (Aldrich, 99.99%) was introduced substituting for Y^{3+} ion (ionic radius 1.015 Å, in eight-fold coordination [8]). The solution was stirred at 70°C for 3h to form a precursor complex gel which was dried at 100°C for 24h. The formation of X1 and X2 phases were confirmed by XRD analysis of the powders annealed at 1000°C and 1500°C, respectively (Fig. 4.23 and Fig. 4.24). In between investigations the samples were stored at RT in dark and dry conditions.

X-ray diffraction patterns (XRPD) were measured with a Thermo ARL X′TRA powder diffractometer, operating in the Bragg-Brentano geometry and equipped with a Cu-anode X-ray source (K_α, $\lambda = 1.5418$ Å) with a Peltier Si(Li) cooled solid state detector. All the diffraction peaks in the powder patterns of Pr^{3+}-doped X1 and X2-YSO are compatible with ICDD data on YSO (PDF Card No. 00-052-1810 and 00-036-1476, respectively). No other phases were detected, indicating that the synthesized samples are single phases. The estimated size of the crystallites, from the XRD pattern, is 54 nm for X1 phase and >150 nm for X2 phase.
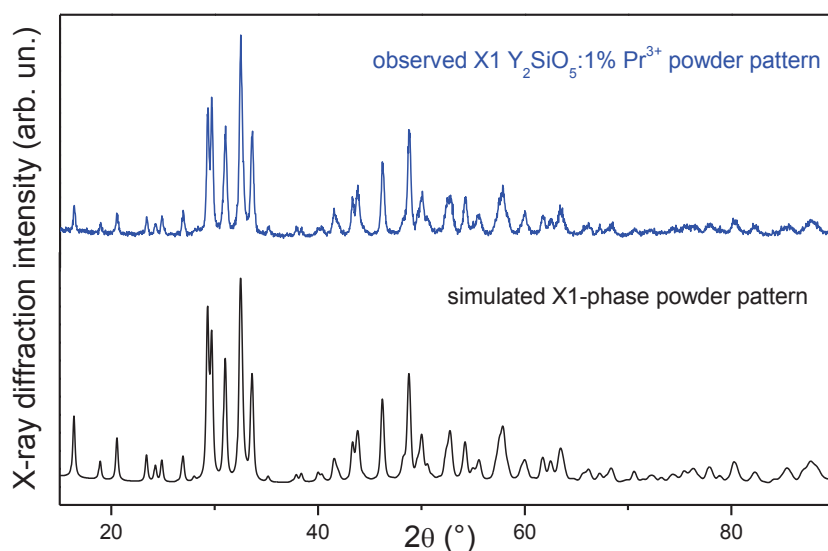

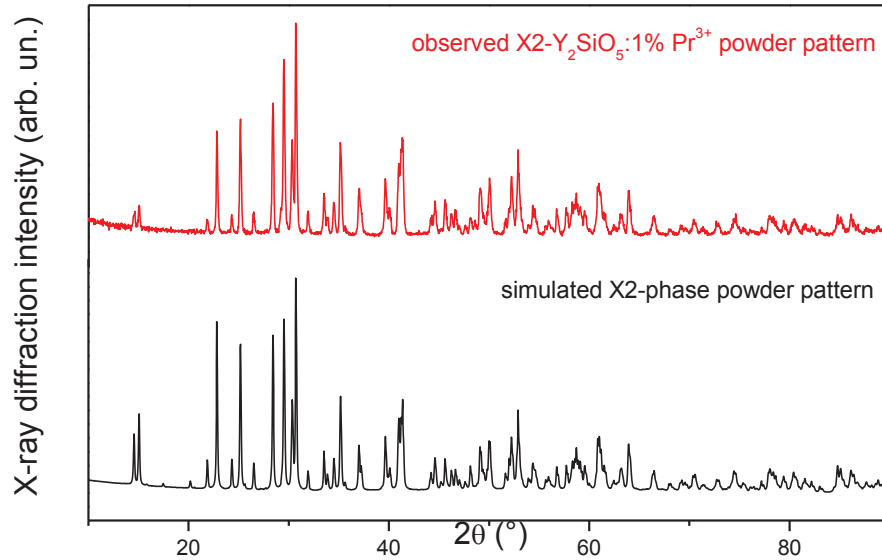**Fig. 4.23**. X-Ray powders patterns of the synthesized X1-YSO:Pr^{3+} and simulated X1-YSO

Fig. 4.24 X-Ray powders patterns of the synthesized X2-YSO:Pr^{3+} and simulated X2-YSO

The time-resolved VUV spectroscopic measurements were carried out at the SUPERLUMI station of HASYLAB (Hamburg, Germany) described in more detail in section 3.2.1. The time-resolved spectra were recorded within two time gates (TGs): 2-13 ns (fast time gate) and 120-170 ns (slow time gate) relative to the beginning of the SR pulse. The time-integrated spectra were recorded counting emission signal within the whole time period of 192 ns available between SR pulses at normal (5) bunch mode (BM) of the storage ring. The decay curves were recorded at reduced (2) BM allowing a longer time range.

4.5.3 Luminescence spectroscopy and dynamics

Fig. 4.25 presents RT time-integrated and time-resolved emission spectra of both X1 and X2 phases recorded upon excitation at 170 nm, that corresponds to transitions across the band-gap. The latter (E_g) is located at about 6.7 eV (~ 180 nm) as suggested by the analysis of available VUV reflection and excitation spectra [73]. Time-integrated spectra are dominated by a broad band located in the UV spectral region and characterized by two prominent maxima located at about 290 and 339 nm in the X1-YSO:Pr^{3+} and 277 and 314 nm in the X2-YSO:Pr^{3+}. These emission features, which were found to be characterized by a fast decaying emission signal (2-13 ns range), are identified as the parity-allowed interconfigurational transitions from the lowest excited 5d$_1$ state to the multiplets of the ground 4f^2 electronic configuration of Pr^{3+} ion. The energy shift observed between the two emission maxima in X1- and X2-YSO:Pr^{3+} emission spectra is connected with the

different crystal field strength around the Pr^{3+} dopant ions and due to the different coordination number of the two available Y1 and Y2 crystallographic sites in X1-YSO and X2-YSO (see section 4.5.1). These spectral features which are very similar to that observed upon direct intra-centre excitation (not shown) indicate an efficient energy transfer from host-to-impurity. Further emissions were observed in the visible spectral region and centred around 500 and 610 nm for both the compounds. These latter features, which were attributed to the intraconfigurational Pr^{3+} $4f^2 \rightarrow 4f^2$ transitions from the $^1D_2$ and $^3P_0$ levels to the ground state $^3H_4$, are obviously not influenced by the crystal field strength and result localized at around the same wavelengths in X1- and X2-phase. The broad and weak emission band located around 400 nm in the X1-YSO:Pr^{3+} time-integrated spectrum was tentatively assigned to a defect emission.
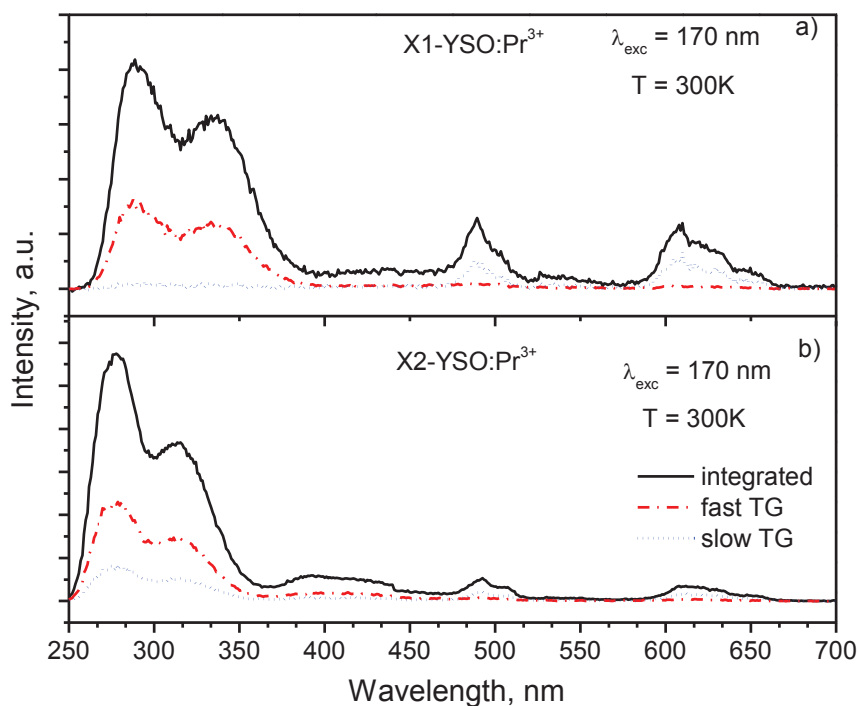

Fig. 4.25. RT-time-resolved and time-integrated emission spectra of X1-YSO:Pr (a) and X2-YSO:Pr (b) upon band-gap excitation at 170 nm.

The time-integrated excitation spectra of Pr^{3+} 5d-4f emission (Fig. 4.26) in X1- and X2-YSO are characterized by a strong doubled band in the UV region, which is assigned to the transitions from the ground 4f state $^3H_4$ to the lowest $5d_1$ and $5d_2$ crystal field levels of Pr^{3+}, and by a broad structured band spread over the VUV range with low-energy onset near 180 nm which represents the beginning of fundamental optical absorption of the host. It is worth nothing that the spectra show a different location of the lowest 4f-$5d_2$ transition for the two phases (219 nm in X1-phase

and 208 nm in X2-phase) indicating a different splitting of the Pr^{3+} 5d states. Consequently, the energy separation between the $5d_1$ and $5d_2$ levels suggests a weaker host-dopant interaction in the case of the Pr-doped X1-YSO. The lowest energetic $5d_1$ band is located at nearly the same energy in the two phases (247 and 246 nm). These values are consistent with the positions (252 and 249 nm for X1- and X2-YSO:Pr^{3+}, respectively) predicted with the Dorenbos model [5], using the data on the energy of 4f-5d transitions for Ce^{3+} in the same hosts.

It is important to point out that the contribution of fast time gated signal in the time-integrated one remains similar to that observed for direct 4f-5d excitation (not shown). These facts indicate an efficient and fast energy transfer of the host electronic excitation to the emitting Pr^{3+} 5d state and suggest good potentials of X1- and X2-YSO:Pr^{3+} to become promising scintillators as nano- and ultafine-powders.
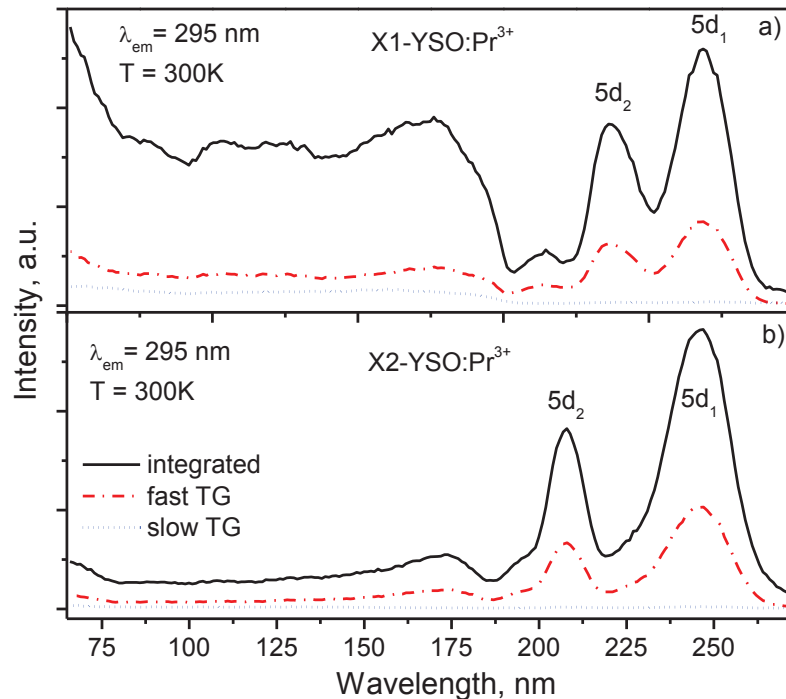

Fig. 4.26. RT-time-resolved and time-integrated excitation spectra of X1-YSO:Pr^{3+} (a) and X2-YSO:Pr^{3+} (b) monitoring Pr^{3+} 5d-4f emission at 295 nm.

The decay curves of the Pr^{3+} 5d-4f emission taken upon intra-centre excitation at RT and 8K were found to deviate from an exponential behaviour (Fig. 4.27). This is likely to be caused by a quenching of emission due to surface defects as obviously expected for nanophosphors (see [40] and references therein). We do not exclude that the complex profile of the decay curves can also be

due to the presence of two crystallographic sites for Pr^{3+} in the two YSO structure. The decay curves were thus quantified using an average decay time τ_{avg} previously expressed in equation 4.2.

At T = 8 K the decay kinetics of the Pr^{3+} 5d-4f emission taken upon direct intra-centre excitation is characterized by an average decay time of 14 ns in X1-YSO and 21 ns in X2-YSO. This latter value is very similar to the leading Pr^{3+} 5d-4f emission decay component found by Novoselov [74] and Pejchal [38] in X2-YSO single crystals grown by the micro-pulling down method (0.25 at.% of Pr^{3+} in the melt). About the decay kinetics of Pr^{3+} in X1-YSO single crystals no data was found in literature to make a comparison with our results. The lower average decay time found for Pr^{3+} in X1-phase is likely due to the smaller size of the particles that induce a greater contribution of the surface defects and then a greater emission quenching compared to that found for Pr^{3+} in the bigger X2-phase particles. When the temperature increases up to 300 K no significant changes in average decay time was observed suggesting the absence of any intra-center quenching mechanisms up to T = 300 K. This behaviour is in line with that found by Pejchal et al. in [38] for bulk crystals where a substantial shortening in decay time was observed just over 350 K and induced by photoionization process.
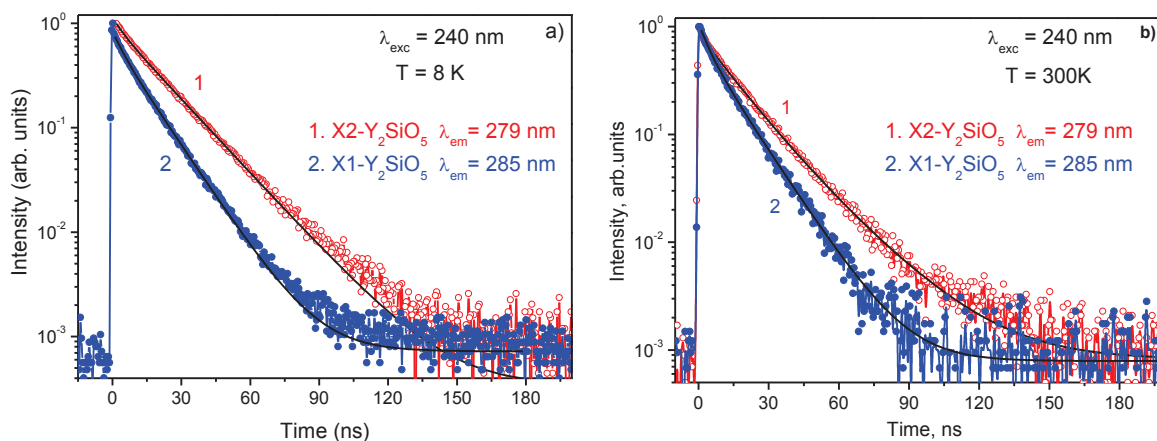

Fig. 4.27 Decay curves of 5d-4f emission of Pr^{3+} in X1- and X2-YSO upon direct excitation at 240 nm at 8K (a) and at room temperature (b).

A slight non-exponential behaviour was also observed for the band-gap excited decay curves of the Pr^{3+} 5d-4f emission recorded at RT (Fig. 4.28). A simple recombination of electron-hole pair on an impurity centre is a single-exponential process. Hence, the deviation from the exponential behaviour observed in the band-gap excited decay curves could be determined by the host-to-impurity energy transfer and quenching processes, as mentioned in case of LSO:Pr^{3+}. The calculated average decay times for X1-YSO: Pr^{3+} ($\tau_{avg} \sim 20$ ns) and X2-YSO:Pr^{3+} ($\tau_{avg} \sim 33$ ns) have resulted to be slightly longer than those calculated for the curves obtained upon direct

excitation and possibly due to the afterglow. As matter of the fact afterglow has been demonstrated to be quite common in several oxyorthosilicates [68, 75] after irradiation with γ- and X-rays or deep UV light and it severely limits the effectiveness and energy resolution of the corresponding scintillators. Besides, a study of thermoluminescence may be required to get more insight into the energy structure of any trapping centers responsible of the afterglow. Furthermore, it is important to note that the decay curves do not display any significant rise of the emission intensity just after the excitation pulse indicating that the excitation energy is very rapidly transferred to the emitting centers.
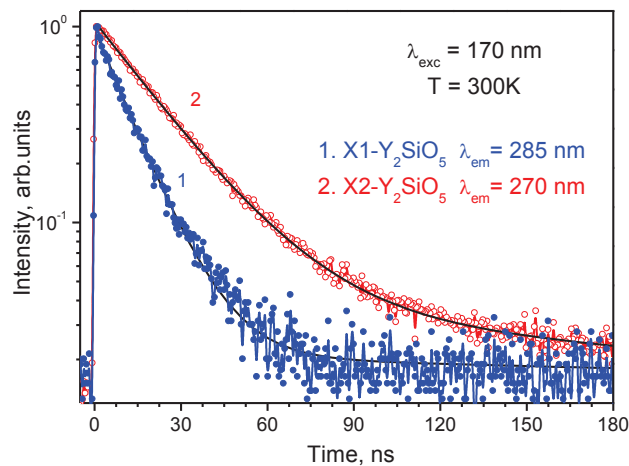

Fig. 4.28 RT decay curves of 5d-4f emission of Pr^{3+} in X1- and X2-YSO upon band-gap excitation

4.5.4 Conclusions

   In summary, X1-YSO:Pr^{3+} as ultrafine powders and X2-YSO:Pr^{3+} as nanocrystalline powders have been successfully synthesized using the sol-gel process. The investigation of the luminescence properties of the these materials have been based on time-resolved VUV spectroscopy by using synchrotron radiation as excitation source. The experimental results revealed efficient and fast transfer of host electronic excitations to emitting Pr^{3+} ions. The lifetimes (14 ns for X1- and 21 ns for X2-phase) are found to be nearly temperature independent within the range 8–300 K and no build-up of the luminescence at short time scale is observed. In conclusion, due to the efficient and fast host-to-impurity energy transfer along with the good chemical stability of the matrixes, X1- and X2-YSO:Pr^{3+} as nano- and ultrafine-powders, respectively, may provide a new interesting addition to the arsenal of available dense scintillators.

4.6 BaMgF$_4$:Nd^{3+} single crystal

4.6.1 Introduction

BaMgF$_4$ (BMF), one of the few ferroelectric fluorides reported up to now, is a nonlinear crystal which exhibits an extraordinary transparency range extended from the deep UV (~125 nm) to the mid-infrared (~13 μm) [76]. This constitutes an exceptional window for the observation of optical processes or transitions not possible in other systems, and offers a unique chance to fabricate optical devices operating in the UV and mid-IR, where other nonlinear materials cannot be used. Regarding its photonic applications, frequency conversion processes in both visible and UV spectral region have been recently reported by using different schemes. Namely, a collinear second harmonic generation (SHG) as well as conical Cerenkov SHG processes have been recently achieved by using 1D and 2D ferroelectric domain structures, respectively. Further, a very efficient UV third harmonic generation (THG) at 385 nm has been also demonstrated by means of a $\chi^{(3)}$ process [77].

In this context, the use of this BMF ferroelectric crystal as a host matrix for optically active ions appears as a very interesting subject [78, 79]. In the last years there has been an increasing interest in the study of the parity-allowed 5d-4f transitions of various trivalent rare earth ions (RE^{3+}) incorporated in wide band-gap host lattices for potential applications in the field of scintillators, UV and VUV phosphors and lasers [80-82]. The VUV-UV broad band emission resulting from the interconfigurational 5d-4f transitions of appropriately chosen RE^{3+} ions, combined with the use of the compact pumping sources, may provide the possibility to realize coherent and tunable VUV-UV radiation sources. Among these dopant ions, Nd^{3+} ion seems a particularly promising candidate in the development of potential self-frequency converted all solid-state lasers operating in the UV and VUV and mid-IR spectral region. The potential use of Nd^{3+}-doped BMF single crystals for self-frequency-doubling lasers has already been documented in a recent paper [83] where the spectroscopy properties of this material have been thoroughly investigated under excitation in the near IR region. However, to the best of our knowledge the spectroscopic characteristics of the interconfigurational 5d-4f transitions of Nd^{3+} ion in BMF have not been reported in literature so far, although the Nd^{3+} laser action in VUV-UV spectral region based on the 5d-4f transitions has already been demonstrated in other similar fluoride single crystals such as LaF$_3$ and LiYF$_4$ [84, 85]. In this contribution we investigate the 5d-4f transitions of Nd^{3+} ions in BMF crystals upon selective excitation with synchrotron radiation in the VUV-UV

region in order to understand the basic spectroscopic and dynamical properties of the highly excited Nd^{3+} dopant states, therefore exploring the possibility of obtaining tunable VUV-UV solid state optical devices.

4.1.1 Instrumental details and structural information

Luminescence measurements were carried out at the SUPERLUMI station of HASYLAB (Hamburg, Germany) described in more detail in section 3.2.1. The measurements were performed at the reduced (two) bunch mode of the storage ring that allowed better time separation for time-resolved spectroscopic measurements that was performed employing time-correlated single photon counting (TCSPC) technique. The time-resolved spectra were recorded within two time windows (TWs): 3-35 ns (fast TW) and 248-430 ns (slow TW) relative to the beginning of the SR pulse. The time-integrated spectra were recorded detecting emission signal within the whole time period of 480 ns available between SR pulses.

BMF crystallizes in the orthorhombic system, with space group $Cmc2_1$ [86]. The room temperature structure is non-centrosymmetric, with 4 molecules per unit cell. The Ba^{2+} ion has a coordination number of 9, while Mg^{2+} is octahedrally coordinated. The ionic radius of Nd^{3+} is much closer to the one of Ba^{2+}, and therefore the dopant ion was proposed to enter into the Ba^{2+} sites [83]. The charge compensation required by Nd^{3+} doping could be achieved by cation vacancies or by interstitial F^- ions [87]. For this research two Nd^{3+} doped $BaMgF_4$ single crystals were grown using the Czochralski technique under CF_4 atmosphere [76]. One of the samples contained 0.02 mol% of Nd^{3+} ions relative to Ba^{2+}. Another sample contained 0.02 at% of Nd^{3+} ions and 0.15 mol% of Na^+. The latter was used for charge compensation.

4.6.3 Results and discussion

The time-integrated emission spectrum of $BMF:Nd^{3+}$, recorded in the UV spectral region (200-430 nm) at room temperature (RT) upon VUV intra-centre excitation ($\lambda = 164$ nm), is dominated by a strong double band extending from 210 to 300 nm and a weaker and unresolved band centered at about 370 nm (Fig. 4.29). These emission features, which were found to be characterized by a fast decaying emission signal, are identified as parity-allowed interconfigurational transitions from the lowest $4f^25d^1$ state to the multiplets belonging to the ground $4f^3$ electronic configuration of Nd^{3+} dopant ions. In particular, the band peaking at 226 nm is assigned to the transition to the ^4F_J ($4f^3$) states, whilst the one peaking at 257 nm is assigned to

the transition to the ^4G_J ($4f^3$) states [88]; finally, the weak and unresolved band located at 370 is attributed to the transitions to the ^4D_J ($4f^3$) states [88].
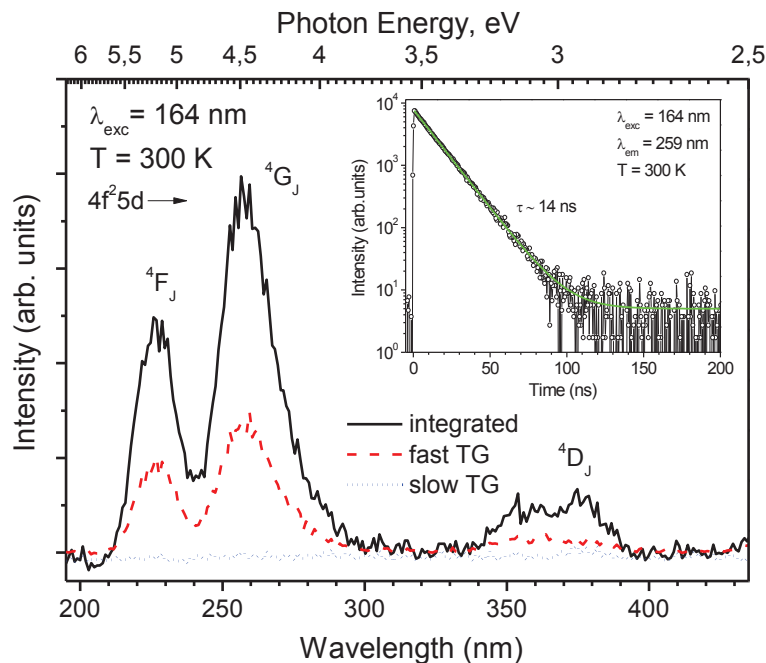

Fig. 4.29 RT time-resolved and time-integrated emission spectra of BMF:Nd^{3+} crystal upon excitation at 164 nm. Inset shows the decay curve recorded monitoring Nd^{3+} emission upon direct excitation at 300 K.

We point out that we were unable to record emission features related to the transition to the ground multiplet ^4I_J ($4f^3$), which are expected to be located at about 175-185 nm for Nd^{3+} ion in a fluoride host. The reason for this were technical issues during our beamtime. Nevertheless, it is reasonable to state that the VUV emission features related to transitions to ^4I_J ($4f^3$) terminating states are the strongest ones in the 5d-4f emission spectrum of BMF:Nd^{3+}. This was observed in many different oxide and fluoride hosts and it is well proven by calculation of oscillator strengths for Nd^{3+} 5d-4f transitions (see [21, 88-90] and references therein). The low temperature spectrum did not reveal any noticeable difference compared to the spectrum recorded at RT (Fig. 4.30).
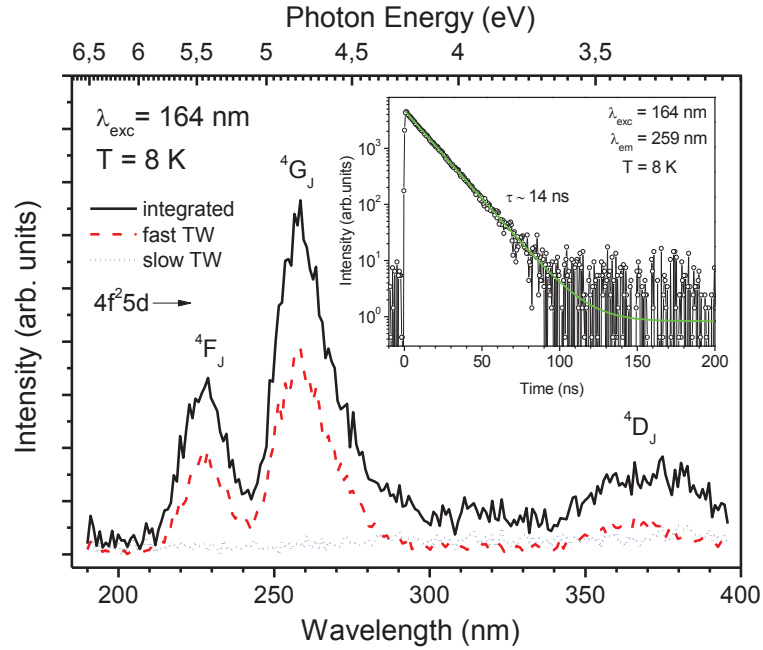
Fig. 4.30 Time-resolved and time-integrated emission spectra of BMF:Nd^{3+} crystal upon excitation at 164 nm at 8 K. Inset shows the decay curve recorded monitoring Nd^{3+} emission upon direct excitation at 8 K.

Fig. 4.31 shows the time-integrated and time-resolved excitation spectra recorded monitoring Nd^{3+} 5d-4f emission at RT. The time-integrated spectrum is characterized by a strong structured feature spread in the range 135-175 nm with the lowest energy maximum at 165 nm. The feature is predominantly formed by a signal detected in the fast TW and is assigned to the transitions from the ground state $^4I_{9/2}$ to the levels belonging to the $4f^25d^1$ configuration of Nd^{3+}.

On the basis of experimentally observed spectral position of the first excitation maximum for Ce^{3+} in BMF when substituting the Ba^{2+} sites (~260 nm, 38460 cm^{-1}) [91, 92], which agrees with the theoretical calculation [93] , and the energy difference between the first 4f-5d transition of Nd^{3+} and Ce^{3+} (22700 cm^{-1} [5]), we estimate a first 4f-5d excitation maximum to be at about 164 nm (61160 cm^{-1}). This is in excellent agreement with our experimental data. On the other hand, the spectroscopic data documented in Refs. [91], [92] and [94] allow estimating a Stokes shift for Ce^{3+} 5d-4f emission in BMF that is about 4400 cm^{-1}. Assuming that the Stokes shift for the rare earth ions having very close ionic radius should be pretty much the same, we can approximately locate the first emission maximum related to the ground $^4I_{9/2}$ ($4f^3$) terminating state as ~176 nm (56760 cm^{-1}).
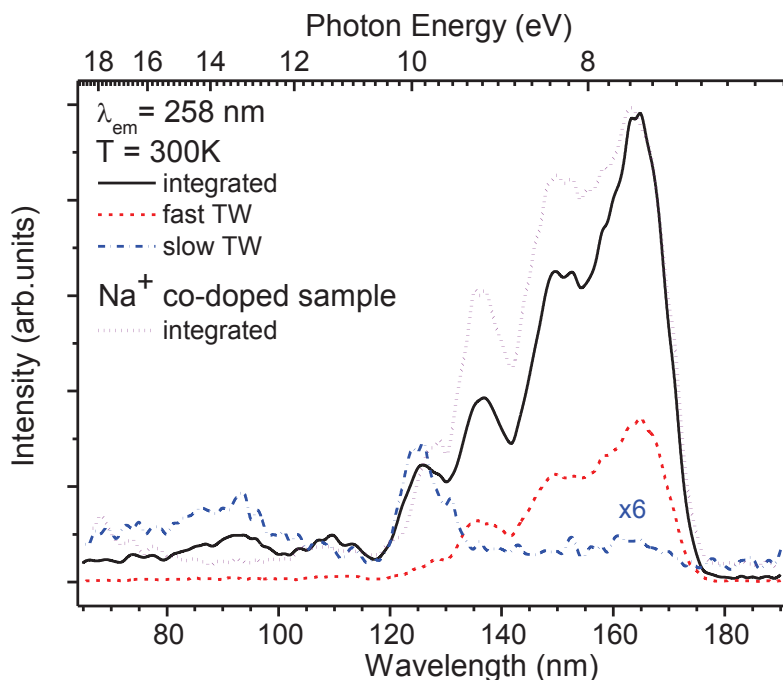
Fig. 4.31 RT time-resolved and time-integrated excitation spectra of BMF:Nd^{3+} and Na$^+$ co-doped BMF:Nd^{3+} crystals recorded monitoring Nd^{3+} 5d-4f emission at 258 nm.

The excitation peak at 125 nm (9.93 eV) is well pronounced in the spectrum recorded within slow TW. In fact, excitation of BMF:Nd^{3+} crystal at about 125 nm or at shorter wavelengths gives rise to an emission spectrum which is virtually lacking any features related to Nd^{3+} 5d-4f transitions and it is composed of a nearly symmetrical broad band extending from about 210 to 475 nm and centered near 310 nm (Fig. 4.32). This emission band is dominated by a signal detected within slow TW. A nature of this emission band as well as the excitation feature at 125 nm is most likely connected with intrinsic electronic excitations in BMF.

To the best of our knowledge BMF lacks a systematic spectroscopic study of the host absorption characteristics. However, some publications report transmission and excitation spectra of undoped BMF which suggest that the fundamental absorption edge of the host should start at about 9.5 eV [76, 92]. As long as BMF represents a BaF$_2$-MgF$_2$ system, it should keep carrying some electronic properties of the binary components (although the crystal structure of BMF is different from BaF$_2$ and MgF$_2$) including a large band gap which is about 11 eV for BaF$_2$ [95] and 12.8 eV for MgF$_2$ [96]. The optically recorded beginning of fundamental absorption can be connected with excitonic absorption. In the case of binary fluorides characterised by a strong exciton-phonon interaction this implies an observation of broad (up to 1.5-2 eV) excitonic features in excitation or absorption spectra [97]. On this basis, the observed feature in the excitation spectrum at 125 nm (Fig. 4.31)

can be connected with excitonic absorption of BMF. In turn, the 310 nm emission band observed upon excitation into this feature (Fig. 4.32) can be tentatively assigned to self-trapped exciton (STE). This is worth comparing with position of a STE emission band in BaF_2 (~307 nm) and MgF_2 (~387 eV) (see [97] and references therein). Nonetheless, based on our experimental results, a defect nature for the 310 nm emission band cannot be ruled out. The unambiguous assignment of this emission requires further investigation in undoped BMF crystals being beyond the scope of this work.
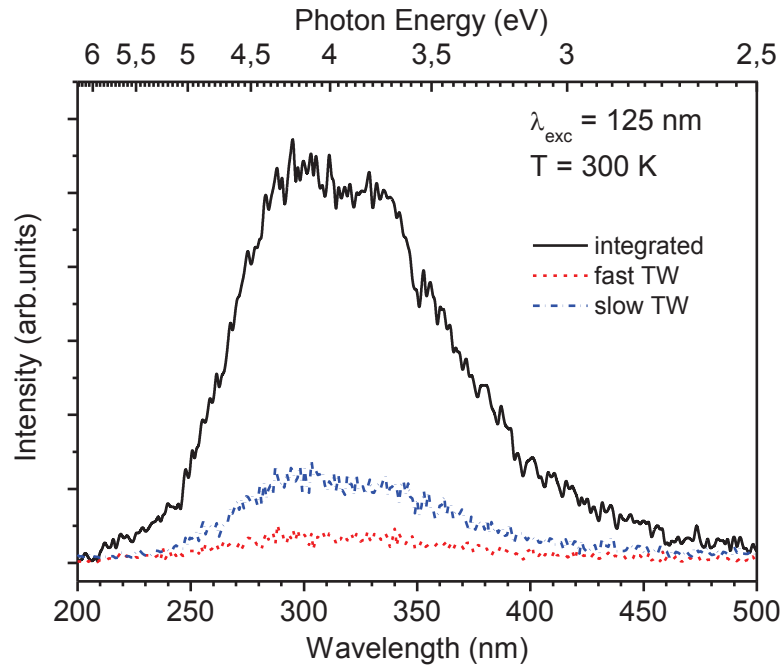
Fig. 4.32 RT time-resolved and time-integrated emission spectra of BMF:Nd^{3+} upon excitation at 125 nm.

Nevertheless, it is clear that energy transfer from the host electronic excitations to Nd^{3+} 5d states is not observed in BMF:Nd^{3+} crystal. This can be due to the fact that energy of relaxed (self-trapped) exciton in BMF is too low to excite 4f-5d transitions in Nd^{3+} that requires energy higher than 7.1 eV. The efficiency of recombination energy transfer depends on the absolute location of ground state of the dopant ion [98]. Unfortunately, to the best of our knowledge information on absolute location of rare earth energy levels in BMF is not available in literature. It is known, however, that Nd^{3+} ground state is located at about 3 eV in CaF_2 [99] 2.5 eV in BaF_2 [100], 3.5 eV in K_3YF_6 [101] , 2.7 eV in $NaLaF_4$ [102] that allows supposition that the Nd^{3+} ground state in BMF is likely located at quite high energy too. The latter prevents more-or-less effective capture of (self-trapped) holes from the valence band and makes the recombination energy transfer mechanism

hardly possible. Thus, we deal with a system where intrinsic electronic excitations predominantly relax via exciton or defects without transferring energy to Nd^{3+} ions.

The time profile of the Nd^{3+} 5d-4f emission at RT, monitored at 257 nm and excited at 164 nm, demonstrates a single exponential behaviour with an approximate lifetime of 14 ns (see the inset in Fig. 4.29), that agrees well with Nd^{3+} 5d-4f emission lifetime observed in other single crystal fluorides (14 ns in BaY_2F_8 , [103] 15.3 ns in SrF_2, 12.3 ns in BaF_2 and 17.7 ns in CaF_2 [104]). We note that the time profile in Fig. 4.29 is shown just within 200 ns (not in a whole time scale of 480 ns) for better representation. The lifetime remains nearly the same when the sample is cooled down to 8 K (see the inset in Fig. 4.30), suggesting no thermal quenching for the Nd^{3+} 5d-4f emission within the temperature range of 8-300 K. In addition, it is worth noting that the Nd^{3+} 5d-4f emission decay curves do not reveal any significant rise time within the time resolution capabilities of the synchrotron setup (better than 1 ns), indicating that excited Nd^{3+} $4f^2 5d^1$ states do not experience any thermally assisted population of the emitting level.

Finally, it should be pointed out that no significant influence of codoping with Na^+ (added as a charge compensator to eliminate defect-distorted Nd_{Ba} sites) in $BMF:Nd^{3+}$ was observed neither in the emission spectra nor in the decay curves. A small difference was observed in a time-integrated excitation spectrum of the Na^+ co-doped crystal. The difference, however, is just in a relative intensity of the spectral features not in their spectral positions (Fig. 4.31). The different relative intensity of the spectral features probably originates from a saturation effect that depends on thickness, orientation and surface quality of the crystal.

4.6.4 Conclusions

In this study we have shown that $BaMgF_4$ is an excellent host for fast and efficient 5d-4f luminescence of Nd^{3+} ions. The Nd^{3+} 5d-4f emission has been shown to decay with a lifetime of 14 ns while experiencing no thermal quenching of the luminescence within the temperature range 8-300 K. The host-to-impurity energy transfer has been found to be inefficient. Nevertheless, the overall spectroscopic and dynamic characteristics recorded for $BMF:Nd^{3+}$ single crystal in combination with its nonlinear optical properties suggest that this system can be a good candidate for the development of optical devices active in the VUV-UV regions, including tunable VUV-UV solid state lasers.

References

1. Rodnyi, P.A., *Progress in fast scintillators.* Radiation Measurements, 2001. **33**(5): p. 605-614.

2. Korzhik, M., et al., *Development of scintillation materials for PET scanners.* Nuclear Instruments and Methods in Physics Research Section A: Accelerators, Spectrometers, Detectors and Associated Equipment, 2007. **571**(1–2): p. 122-125.

3. Van Eijk, C.W.E., P. Dorenbos, and R. Visser, Nd^{3+} *and* Pr^{3+} *doped inorganic scintillators.* Nuclear Science, IEEE Transactions on, 1994. **41**(4): p. 738-741.

4. Nikl, M., et al., *Development of novel scintillator crystals.* Journal of Crystal Growth, 2006. **292**(2): p. 416-421.

5. Dorenbos, P., *The 5d level positions of the trivalent lanthanides in inorganic compounds.* Journal of Luminescence, 2000. **91**(3–4): p. 155-176.

6. Lecointre, A., et al., *Thermally stimulated luminescence of* $Ca_3(PO_4)_2$ *and* $Ca_9Ln(PO_4)_7$ *(Ln = Pr, Eu, Tb, Dy, Ho, Er, Lu).* Radiation Measurements, 2010. **45**(3–6): p. 273-276.

7. Du, F., et al., *Luminescence properties and site occupations of* Eu^{3+} *ions doped in double phosphates* $Ca_9R(PO_4)_7$ *(R = Al, Lu).* Journal of Materials Chemistry, 2011. **21**(12): p. 4669-4678.

8. Shannon, R., *Revised effective ionic radii and systematic studies of interatomic distances in halides and chalcogenides.* Acta Crystallographica Section A, 1976. **32**(5): p. 751-767.

9. Bessière, A., et al., *Site occupancy and mechanisms of thermally stimulated luminescence in* $Ca_9Ln(PO_4)_7$ *(Ln=lanthanide).* Acta Materialia, 2012. **60**(19): p. 6641-6649.

10. Tanner, P.A., et al., *Vacuum ultraviolet excitation spectra of lanthanide-doped hexafluoroelpasolites.* Journal of Physics: Condensed Matter, 2009. **21**(39): p. 395504.

11. Schwarz, L., et al., *Investigations on the electronic structure of double phosphates of the type* $M_3RE(PO_4)_2$ *(RE = rare earths, lanthanides).* Journal of Luminescence, 1997. **72–74**(0): p. 257-259.

12. Huang, C.-H., T.-M. Chen, and B.-M. Cheng, *Luminescence Investigation on Ultraviolet-Emitting Rare-Earth-Doped Phosphors Using Synchrotron Radiation.* Inorganic Chemistry, 2011. **50**(14): p. 6552-6556.

13. Liang, H., et al., *Photoluminescence of* Ce^{3+}, Pr^{3+} *and* Tb^{3+} *activated* $Sr_3Ln(PO_4)_3$ *under VUV-UV excitation.* Journal of Solid State Chemistry, 2004. **177**(3): p. 901-908.

14. Ivanovskikh, K., et al., *Fast UV luminescence in* Pr^{3+}-*doped eulytite double phosphates.* Optical Materials, 2011. **34**(2): p. 419-423.

15.   Zhao, C., et al., *Photoluminescence properties of Ca₉Lu(PO₄)₇:Ce³⁺, Mn²⁺ prepared by conventional solid-state reaction.* Journal of Luminescence, 2012. **132**(3): p. 617-621.

16.   Guo, N., et al., *Ca₉Lu(PO₄)₇:Eu²⁺,Mn²⁺: A Potential Single-Phased White-Light-Emitting Phosphor Suitable for White-Light-Emitting Diodes.* Inorganic Chemistry, 2010. **49**(23): p. 10907-10913.

17.   Mürk, V., B. Namozov, and N. Yaroshevich, *Complex oxides: Electron excitations and their relaxation.* Radiation Measurements, 1995. **24**(4): p. 371-374.

18.   Kirm, M., et al., *Mechanisms of intrinsic and impurity luminescence excitation by synchrotron radiation in wide-gap oxides.* Journal of Electron Spectroscopy and Related Phenomena, 1996. **79**(0): p. 91-94.

19.   Srivastava, A.M., et al., *The influence of the Pr^{3+} $4f^1 5d^1$ configuration on the $^1S_0$ emission efficiency and lifetime in $LaPO_4$.* Optical Materials, 2011. **33**(3): p. 292-298.

20.   Srivastava, A.M., et al., *Luminescence from the Pr^{3+} $4f^1 5d^1$ and $^1S_0$ states in $LiLaP_4O_{12}$.* Journal of Luminescence, 2009. **129**(2): p. 126-129.

21.   Wegh, R.T., W. van Klinken, and A. Meijerink, *High-energy 2G(2)9/2 emission and $4f^2$ $5d{\rightarrow}4f^3$ multiphonon relaxation for Nd^{3+} in orthoborates and orthophosphates.* Physical Review B, 2001. **64**(4): p. 045115.

22.   Laroche, M., et al., *Experimental and theoretical investigation of the $4fn{\rightarrow}4f^{n-1}5d$ transitions in YPO_4:Pr^{3+} and $YPO4$:Pr^{3+}, Ce^{3+}.* Journal of Physics: Condensed Matter, 2001. **13**(4): p. 765.

23.   Henderson, B. and G.F. Imbusch, *Optical Spectroscopy of Inorganic Solids*. 2006: Clarendon Press.

24.   Srivastava, A.M., M. Jennings, and J. Collins, *The interconfigurational $4f^1 5d^1{\rightarrow}4f^2$ luminescence of Pr^{3+} in $LuPO_4$, $K_3Lu(PO_4)_2$ and $LiLuSiO_4$.* Optical Materials, 2012. **34**(8): p. 1347-1352.

25.   Wisniewski, D., et al., *Scintillation and luminescence properties of Ce-activated K3Lu(PO4)2.* Journal of Alloys and Compounds, 2004. **380**(1–2): p. 191-195.

26.   Wisniewski, D. and L.A. Boatner, *Scintillation Properties and Time-Resolved Spectroscopy of a Novel Scintillator Material: Ce^{3+}-Activated $Li_3Lu(PO)_2$ Crystals.* Nuclear Science, IEEE Transactions on, 2009. **56**(6): p. 3806-3818.

27.   Wisniewski, D., et al., *$Rb_3Lu(PO_4)_2$:Ce and $Cs_3Lu(PO_4)_2$:Ce – new promising scintillator materials.* Crystal Research and Technology, 2003. **38**(3-5): p. 275-282.

28.   Yuan, J.L., et al., *VUV spectroscopic properties of Ce^{3+} and Pr^{3+}-doped $AREP_2O_7$-type alkali rare earth diphosphates (A=Na, K, Rb, Cs; RE=Y, Lu).* Journal of Luminescence, 2007. **126**(1): p. 130-134.

29.   Makhov, V.N., et al., *Luminescence properties of YPO₄:Nd³⁺: a promising VUV scintillator material.* Nuclear Instruments and Methods in Physics Research Section A: Accelerators, Spectrometers, Detectors and Associated Equipment, 2002. **486**(1–2): p. 437-442.

30.   Shalapska, T., et al., *Crystal structure and luminescence properties of LiYP₄O₁₂ :Ce ³ ⁺ phosphor.* Journal of Physics: Condensed Matter, 2010. **22**(48): p. 485503.

31.   Murakami, S., et al., *Photoluminescence and decay profiles of undoped and Fe³⁺, Eu³⁺-doped PLZT ceramics at low temperatures down to 10 K.* Inorganica Chimica Acta, 2000. **300–302**(0): p. 1014-1021.

32.   Zych, A., et al., *Analysis of the radiative lifetime of Pr³⁺d-f emission.* Journal of Applied Physics, 2012. **112**(1): p. -.

33.   Kloss, M., et al., *Optical investigation on Na₃RE(PO₄)₂ (RE = La, Gd, Eu).* Journal of Luminescence, 1997. **72–74**(0): p. 684-686.

34.   Yuan, J.-L., et al., *Synthesis, structure and X-ray excited luminescence of Ce³⁺-doped AREP₂O₇-type alkali rare earth diphosphates (A=Na, K, Rb, Cs; RE=Y, Lu).* Journal of Solid State Chemistry, 2007. **180**(12): p. 3381-3387.

35.   Melcher, C.L. and J.S. Schweitzer, *A promising new scintillator: cerium-doped lutetium oxyorthosilicate.* Nuclear Instruments and Methods in Physics Research Section A: Accelerators, Spectrometers, Detectors and Associated Equipment, 1992. **314**(1): p. 212-214.

36.   Mansuy, C., et al., *Characterization and scintillation properties of sol–gel derived Lu₂SiO₅:Ln³⁺ (Ln=Ce, Eu and Tb) powders.* Optical Materials, 2009. **31**(9): p. 1334-1336.

37.   Nikl, M., et al., *Fast 5d→4f luminescence of Pr³⁺ in Lu₂SiO₅ single crystal host.* Chemical Physics Letters, 2005. **410**(4–6): p. 218-221.

38.   Pejchal, J., et al., *Temperature dependence of the Pr³⁺ luminescence in LSO and YSO hosts.* Journal of Luminescence, 2009. **129**(12): p. 1857-1861.

39.   Nikl, M., et al., *Luminescence and scintillation kinetics of the Pr³⁺ doped Lu₂Si₂O₇ single crystal.* Chemical Physics Letters, 2010. **493**(1–3): p. 72-75.

40.   Klassen, N.V., et al., *Nanoscintillators for Microscopic Diagnostics of Biological and Medical Objects and Medical Therapy.* NanoBioscience, IEEE Transactions on, 2009. **8**(1): p. 20-32.

41.   Jacobsohn, L.G., et al., *Synthesis, luminescence and scintillation of rare earth doped lanthanum fluoride nanoparticles.* Optical Materials, 2010. **33**(2): p. 136-140.

42.   McKigney, E.A., et al., *Nanocomposite scintillators for radiation detection and nuclear spectroscopy.* Nuclear Instruments and Methods in Physics Research Section A: Accelerators, Spectrometers, Detectors and Associated Equipment, 2007. **579**(1): p. 15-18.

43.   Nedelec, J.M., *Sol-gel processing of nanostructured inorganic scintillating materials.* J. Nanomaterials, 2007. **2007**(1): p. 1-8.

44.   Jalabadze, N.V., et al., *Development of New Technologies for the Manufacturing of Nanocrystalline Scintillation Materials.* Nuclear Science, IEEE Transactions on, 2008. **55**(3): p. 1514-1522.

45.   Gustafsson, T., et al., *Lu₂SiO₅ by single-crystal X-ray and neutron diffraction.* Acta Crystallographica Section C, 2001. **57**(6): p. 668-669.

46.   Lutterotti, L. and S. Gialanella, *X-ray diffraction characterization of heavily deformed metallic specimens.* Acta Materialia, 1998. **46**(1): p. 101-110.

47.   Ivanov, V.Y., et al., *Electronic excitations and energy transfer in A₂SiO₅–Ce (A=Y, Lu, Gd) and Sc₂SiO₅ single crystals.* Nuclear Instruments and Methods in Physics Research Section A: Accelerators, Spectrometers, Detectors and Associated Equipment, 2001. **470**(1–2): p. 358-362.

48.   Ning, L., et al., *Electronic properties and 4f →5d transitions in Ce-doped Lu₂SiO₅: a theoretical investigation.* Journal of Materials Chemistry, 2012. **22**(27): p. 13723-13731.

49.   Ivanov, V.Y., et al., *Intrinsic luminescence of rare-earth oxyorthosilicates.* Physics of the Solid State, 2008. **50**(9): p. 1692-1698.

50.   Mikhailin, V.V., *Excitation of secondary processes in the vacuum ultraviolet range.* Nuclear Instruments and Methods in Physics Research Section A: Accelerators, Spectrometers, Detectors and Associated Equipment, 1987. **261**(1–2): p. 107-114.

51.   Kamenskikh, I.A., et al., *High-energy excitation of luminescence of crystals with oxyanions.* Nuclear Instruments and Methods in Physics Research Section A: Accelerators, Spectrometers, Detectors and Associated Equipment, 1989. **282**(2–3): p. 599-606.

52.   Mikhailin, V.V., et al., *Study of optical and luminescent properties of some inorganic scintillators in the fundamental absorption region.* Nuclear Instruments and Methods in Physics Research Section A: Accelerators, Spectrometers, Detectors and Associated Equipment, 2002. **486**(1–2): p. 367-373.

53.   Il'mas, E.R., C.B. Lushchik, and T.I. Savikhina, *Light transformers with photon multiplication.* Journal of Applied Spectroscopy, 1969. **10**(1): p. 92-97.

54.   Amans, D., et al., *Time-Resolved VUV Excited Luminescence of Y₂O₃-Yb Nanoparticles.* Nuclear Science, IEEE Transactions on, 2010. **57**(3): p. 1355-1360.

55.   van der Kolk, E., et al., *5d electron delocalization of Ce^{3+} and Pr^{3+} in Y$_2$SiO$_5$ and Lu$_2$SiO$_5$.* Physical Review B, 2005. **71**(16): p. 165120.

56.   Malyukin, Y.V., *Fundamental aspects of activated nanocrystal luminescence and possible applications.* Radiation Measurements, 2010. **45**(3–6): p. 589-593.

57.   Masalov, A., et al., *Strong quenching of praseodymium f–f luminescence induced by a surface of Y$_2$SiO$_5$:Pr^{3+} nanocrystal.* Journal of Luminescence, 2009. **129**(12): p. 1695-1697.

58.   Barta, J., et al., *Radiation-induced preparation of pure and Ce-doped lutetium aluminium garnet and its luminescent properties.* Journal of Materials Chemistry, 2012. **22**(32): p. 16590-16597.

59.   Shionoya, S., W.M. Yen, and H. Yamamoto, *Phosphor Handbook.* 2012: Taylor & Francis.

60.   Suyver, J.F., J.J. Kelly, and A. Meijerink, *Temperature-induced line broadening, line narrowing and line shift in the luminescence of nanocrystalline ZnS:Mn^{2+}.* Journal of Luminescence, 2003. **104**(3): p. 187-196.

61.   Bang, J., H. Yang, and P.H. Holloway, *Enhanced and stable green emission of ZnO nanoparticles by surface segregation of Mg.* Nanotechnology, 2006. **17**(4): p. 973.

62.   Shih, S.-J., Y.-Y. Wu, and K. Borisenko, *Control of morphology and dopant distribution in yttrium-doped ceria nanoparticles.* Journal of Nanoparticle Research, 2011. **13**(12): p. 7021-7028.

63.   Weng, X., et al., *Synthesis and characterization of doped nano-sized ceria–zirconia solid solutions.* Applied Catalysis B: Environmental, 2009. **90**(3–4): p. 405-415.

64.   Wang, J., et al., *Preparation and X-ray characterization of low-temperature phases of R$_2$SiO$_5$ (R = rare earth elements).* Materials Research Bulletin, 2001. **36**(10): p. 1855-1861.

65.   Shoudu, Z., et al., *Czochralski growth of rare-earth orthosilicates–Y$_2$SiO$_5$ single crystals.* Journal of Crystal Growth, 1999. **197**(4): p. 901-904.

66.   Rotman, S.R., *Wide-Gap Luminescent Materials: Theory and Applications: Theory and Applications*. 1997: Springer US.

67.   Coetsee, E., et al., *Luminescent mechanism of Y$_2$SiO$_5$:Ce phosphor powder.* Physica B: Condensed Matter, 2009. **404**(22): p. 4426-4430.

68.   Yukihara, E.G., et al., *Luminescence properties of Ce-doped oxyorthosilicate nanophosphors and single crystals.* Journal of Luminescence, 2010. **130**(12): p. 2309-2316.

69.   Aitasalo, T., et al., *Delayed luminescence of Ce^{3+} doped X1 form of Y$_2$SiO$_5$.* Optical Materials, 2005. **27**(9): p. 1511-1515.

70.   Chiriu, D., et al., *Structural characterization of Lu₁.₈Y₀.₂SiO₅ crystals.* Physical Review B, 2007. **76**(5): p. 054112.

71.   Znamenskiy, N.V., et al., *Concentration quenching anomalies of activated Y₂SiO₅:Pr³⁺ nanocrystal luminescence.* Laser Physics, 2007. **17**(4): p. 491-495.

72.   Wojtowicz, A.J., et al., *Scintillation properties of selected oxide monocrystals activated with Ce and Pr.* Optical Materials, 2006. **28**(1–2): p. 85-93.

73.   Zorenko, Y., et al., *Intrinsic luminescence of Lu₂SiO₅ (LSO) and Y₂SiO₅ (YSO) orthosilicates.* Journal of Luminescence, 2013. **137**(0): p. 204-207.

74.   Novoselov, A., et al., *Crystal growth, optical and luminescence properties of Pr-doped Y₂SiO₅ single crystals.* Optical Materials, 2007. **29**(11): p. 1381-1384.

75.   Dorenbos, P., et al., *Afterglow and thermoluminescence properties of Lu₂SiO₅:Ce scintillation crystals.* Journal of Physics: Condensed Matter, 1994. **6**(22): p. 4167.

76.   Shimamura, K., et al., *Advantageous growth characteristics and properties of compared with for UV/VUV nonlinear optical applications.* Journal of Crystal Growth, 2005. **275**(1–2): p. 128-134.

77.   Víllora, E.G., et al., *Birefringent- and quasi phase-matching with BaMgF₄ for vacuum-UV/UV and mid-IR all solid-state lasers.* Optics Express, 2009. **17**(15): p. 12362-12378.

78.   Janssens, S., G.V.M. Williams, and D. Clarke, *Synthesis and characterization of rare earth and transition metal doped BaMgF₄ nanoparticles.* Journal of Luminescence, 2013. **134**(0): p. 277-283.

79.   Kück, S., et al., *Emission and excitation characteristics and internal quantum efficiencies of vacuum-ultraviolet excited Pr³⁺ -doped fluoride compounds.* Physical Review B, 2005. **71**(16): p. 165112.

80.   Ivanovskikh, K.V., et al., *Optical spectroscopy of Ca₃Sc₂Si₃O₁₂, Ca₃Y₂Si₃O₁₂ and Ca₃Lu₂Si₃O₁₂ doped with Pr³⁺.* Journal of Luminescence, 2010. **130**(5): p. 893-901.

81.   Omelkov, S.I., et al., *A luminescence spectroscopy and theoretical study of 4f–5d transitions of Ce ³ ⁺ ions in SrAlF ₅ crystals.* Journal of Physics: Condensed Matter, 2011. **23**(10): p. 105501.

82.   Petrosyan, A.G., et al., *Potential of existing growth methods of LuAP and related scintillators.* Nuclear Instruments and Methods in Physics Research Section A: Accelerators, Spectrometers, Detectors and Associated Equipment, 2002. **486**(1–2): p. 74-78.

83.   Muñoz-Santiuste, J.E., et al., *Local environment of optically active Nd³⁺ ions in the ultratransparent BaMgF₄ ferroelectric crystal.* Physical Review B, 2012. **85**(18): p. 184110.

84.   Waynant, R.W. and P.H. Klein, *Vacuum ultraviolet laser emission from Nd³⁺:LaF₃.* Applied Physics Letters, 1985. **46**(1): p. 14-16.

85.   Dubinskii, M.A., et al., *Efficient LaF₃: Nd³⁺-based vacuum-ultraviolet laser at 172 nm.* Journal of the Optical Society of America B, 1992. **9**(7): p. 1148-1150.

86.   Gingl, F., *BaMgF4 and Ba2Mg3F10: New examples for structural relationships between hydrides and fluorides.* Zeitschrift für anorganische und allgemeine Chemie, 1997. **623**(1-6): p. 705-709.

87.   Víllora, E.G., et al., *Neodymium doping in UV-IR transparent ferroelectric BaMgF₄.* Journal of Applied Physics, 2010. **107**(3): p. -.

88.   van Pieterson, L., et al., *4fⁿ→4fⁿ⁻¹5d transitions of the light lanthanides: Experiment and theory.* Physical Review B, 2002. **65**(4): p. 045113.

89.   van Pieterson, L., et al., *Emission spectra and trends for 4fⁿ⁻¹5d↔4fⁿ transitions of lanthanide ions: Experiment and theory.* The Journal of Chemical Physics, 2001. **115**(20): p. 9382-9392.

90.   Khaidukov, N.M., et al., *VUV spectroscopy of KYF₄ crystals doped with Nd³⁺, Er³⁺ and Tm³⁺.* Optics Communications, 2000. **184**(1–4): p. 183-193.

91.   Yamaga, M., T. Imai, and N. Kodama, *Optical properties of two Ce³⁺-site centers in BaMgF₄:Ce³⁺ crystals.* Journal of Luminescence, 2000. **87–89**(0): p. 992-994.

92.   Hayashi, E., et al., *Vacuum ultraviolet and ultraviolet spectroscopy of BaMgF₄ codoped with Ce³⁺ and Na⁺.* Journal of Luminescence, 2006. **119–120**(0): p. 69-74.

93.   Watanabe, S., et al., *First-principles relativistic calculation for 4f–5d transition energy of Ce³⁺ in various fluoride hosts.* Journal of Solid State Chemistry, 2006. **179**(8): p. 2438-2442.

94.   Kodama, N., et al., *Optical and structural studies on BaMgF₄:Ce³⁺ crystals.* Journal of Crystal Growth, 2001. **229**(1–4): p. 492-496.

95.   Rubloff, G.W., *Far-Ultraviolet Reflectance Spectra and the Electronic Structure of Ionic Crystals.* Physical Review B, 1972. **5**(2): p. 662-684.

96.   Jouanin, C., J.P. Albert, and C. Gout, *Band structure and optical properties of magnesium fluoride.* J. Phys. France, 1976. **37**(5): p. 595-602.

97.   Song, A.K.S.W.R.T., *Self-trapped excitons.* 1996, Berlin; New York: Springer.

98.   Belsky, A.N. and J.C. Krupa, *Luminescence excitation mechanisms of rare earth doped phosphors in the VUV range.* Displays, 1999. **19**(4): p. 185-196.

99.   Dorenbos, P., *Locating lanthanide impurity levels in the forbidden band of host crystals.* Journal of Luminescence, 2004. **108**(1–4): p. 301-305.

100.   Rodnyĭ, P.A., I.V. Khodyuk, and G.B. Stryganyuk, *Location of the energy levels of the rare-earth ions in BaF$_2$ and CdF$_2$.* Physics of the Solid State, 2008. **50**(9): p. 1639-1643.

101.   Ma, C.-G., et al., *Spectroscopy and Calculations for 4f^N → 4f^{N-1}5d Transitions of Lanthanide Ions in K$_3$YF$_6$.* The Journal of Physical Chemistry A, 2012. **116**(36): p. 9158-9180.

102.   Krumpel, A.H., et al., *Lanthanide 4f-level location in lanthanide doped and cerium-lanthanide codoped NaLaF$_4$ by photo- and thermoluminescence.* Journal of Applied Physics, 2008. **104**(7): p. -.

103.   Pejchal, J., et al., *Luminescence and Scintillation Properties of VUV Scintillation Crystals Based on Lu-Admixed BaY$_2$F$_8$.* Nuclear Science, IEEE Transactions on, 2012. **59**(5): p. 2177-2182.

104.   Radzhabov, E., et al., *5d-4f Emission of Nd^{3+}, Sm^{3+}, Ho^{3+}, Er^{3+}, Tm^{3+} Ions in Alkaline Earth Fluorides.* Nuclear Science, IEEE Transactions on, 2012. **59**(5): p. 2074-2078.

Chapter 5

Conclusions

The purpose of this thesis work was the development and improvement of new fast inorganic scintillator materials for applications in modern medical diagnostic techniques such as positron emission tomography. This work has included the synthesis and the research on the processes responsible for a fast feeding and radiative relaxation of 5d states of lanthanide ions, crystal structure defects and intrinsic electronic excitations (electrons, holes, e-h pairs, excitons) in wide-gap crystal materials characterized by different dimensions, electronic structure and electron-phonon coupling.

Several materials have been investigated including the double phosphates $Ca_9Lu(PO_4)_7:Ce^{3+}/Pr^{3+}$, $K_3Lu(PO_4)_7:Pr^{3+}$ and $KLuP_2O_7:Pr^{3+}$ as bulk powders, the oxyorthosilicates $X1-Y_2SiO_5:Pr^{3+}$, $X2-Y_2SiO_5:Pr^{3+}$ and $X2-Lu_2SiO_5:Pr^{3+}$ as nanopowders and the fluoride $BaMgF_4:Nd^{3+}$ as single crystal.

The fast 5d-4f emission of Pr^{3+} and Ce^{3+} in $Ca_9Lu(PO_4)_7$ stable within temperature range 8-300 K has been observed from both Ce^{3+} and Pr^{3+} doped samples upon direct intra-centre VUV excitation but only in the case of $Ca_9Lu(PO_4)_7:Ce^{3+}$ sample efficient host-to-impurity energy transfer has been revealed. The analysis of time-resolved emission and excitation spectra has suggested the existence of multiple structure of the excited states of the defects, which experience significant Stokes shift and at the same time capture a significant fraction of host electronic excitations. The low excitation energy of Ce^{3+} 5d states allows efficient non-radiative energy transfer from the excited states of defects. This is not the case for $Ca_9Lu(PO_4)_7:Pr^{3+}$ where absorption of the defects competes with Pr^{3+} 4f-5d transitions. The results obtained in this work clearly showed that defects present in $Ca_9Lu(PO_4)_7$, which are at least partly attributed to the disordered nature of the host, substantially govern the dynamics and efficiency of the energy transfer processes.

$K_3Lu(PO_4)_2$ and $KLuP_2O_7$ revealed fast and efficient host-to-Pr^{3+} energy transfer suggesting good potentialities for application of these materials as fast scintillators. In the case of $K_3Lu(PO_4)_2$:Pr^{3+} luminescence spectra as well as decay curves showed significant changes with the temperature within the range 8-300 K reflecting the two crystal phase transitions of this compound.

The experimental results on nanopowders of sol-gel derived X1-Y_2SiO_5:Pr^{3+}, X2-Y_2SiO_5:Pr^{3+} and Lu_2SiO_5:Pr^{3+} revealed efficient and fast transfer of host electronic excitations to emitting Pr^{3+} ions, short Pr^{3+} 5d-4f emission decay time and absence of luminescence build-up. In the case of X2-Lu_2SiO_5:Pr^{3+} some evidences of thermally induced quenching processes have been observed and mainly addressed to surface related defects.

The Nd^{3+} 5d-4f emission in $BaMgF_4$ single crystal has been shown to decay with a lifetime of 14 ns while experiencing no thermal quenching of the luminescence within the temperature range 8-300 K. The host-to-impurity energy transfer has been found to be inefficient. Nevertheless, the overall spectroscopic and dynamic characteristics recorded for this material in combination with its nonlinear optical properties suggest that this system can be a good candidate for the development of optical devices active in the VUV-UV regions, including tunable VUV-UV solid state lasers.

List of publications

➢ M. Trevisani, K.V. Ivanovskikh, F. Piccinelli, A. Speghini, M. Bettinelli, *Fast UV luminescence of Pr^{3+} doped Calcium Lutetium Whitlockite*, ECS Transaction **41 (37)**, 11 (2012).

➢ T. Passuello, F. Piccinelli, M. Trevisani, M. Giarola, G. Mariotto, L. Marciniak, D. Hreniak, M. Guzik, M. Fasoli, A. Vedda, V. Jarý, M. Nikl, V. Causin, M. Bettinelli and A. Speghini, *Structural and optic properties of Vernier phase lutetium oxyfluorides doped with lanthanide ions: interesting candidates as scintillators and X-Ray phosphors,* Journal of Material Chemistry **22**, 10639 (2012).

➢ P. Haro-González, L. Martinez Maestro, M. Trevisani, S. Polizzi, D. Jaque, J. García Sole, and M. Bettinelli, *Evaluation of rare earth doped silica microspheres as optically controlled temperature sensors*, Journal of Applied Physics **112 (5)**, 054702 (2012).

➢ M. Trevisani, K.V. Ivanovskikh, F. Piccinelli, A. Speghini, M. Bettinelli, *Interconfigurational 5d→4f luminescence of Ce^{3+} and Pr^{3+} in Ca$_9$Lu(PO$_4$)$_7$,* Journal of Physics: Condensed Matter **24 (38)**, 385502 (2012).

➢ M. Trevisani, K.V. Ivanovskikh, N. Grillet, F. Piccinelli, M. Bettinelli, *Structural characterisation and time-resolved luminescence spectroscopy of nanocrystalline X2-Lu$_2$SiO$_5$:Pr^{3+} powders*, Chemical Physics Letter **565**, 80 (2013).

➢ C.-G. Ma, M. Trevisani, F. Piccinelli, K.V. Ivanovskikh, M. Bettinelli, M.G. Brik, *Analysis of vacuum ultraviolet electronic spectra of Ce^{3+} and Pr^{3+} ions in Ca$_9$Lu(PO$_4$)$_7$: Crystal-field calculations and simulation of optical spectra*, Journal of Physics: Cond. Matter **25 (16)**,165503 (2013).

➢ M. Trevisani, K. Ivanovskikh, F. Piccinelli, M. Bettinelli, *Synchrotron Radiation Study of Interconfigurational 5d-4f Luminescence of Pr^{3+} in KLuP$_2$O$_7$*, Z. Naturforschung, **69b**, 205, (2014).

➢ A.M. Srivastava, S.J. Camardello, H.A. Comanzo, M. Trevisani, M. Bettinelli, *Optical Spectroscopy of Pr^{3+} in the weberite, NaGdSb$_2$O$_7$: High covalence of Pr^{3+}-O^{2-} bonding*, Journal of Luminescence **148** (2014) 262.

➢ M. Trevisani, K. Ivanovskikh, F. Piccinelli, M. Bettinelli, *Fast 5d-4f luminescence in Pr^{3+}-doped K$_3$Lu(PO$_4$)$_2$*, Journal of Luminescence, in press.

➢ M. Trevisani, K.V. Ivanovskikh, M. O. Ramírez, P. Molina, E. G. Víllora, K. Shimamura, L. E. Bausá, M. Bettinelli, *VUV-UV 5d-4f interconfigurational transitions of Nd^{3+} in BaMgF$_4$ ferroelectric crystals*, Journal of Luminescence, in press.

Acknowledgements